Projet de Recherche INTERREG-V océan Indien 2014-2020
A1/OT1/OS-01a - Action II-2 TN

ReNovRisk-Cyclones et Précipitations

L8 : Rapport de synthèse ou article scientifique sur les techniques de descente d'échelle climatique

Olivier BOUSQUET

Laboratoire de l'Atmosphère et des Cyclones
(UMR 8105 CNRS/Météo-France/Université de La Réunion)

Livrable 8

Rapport de synthèse ou article scientifique sur les techniques de descente d'échelle climatique

Les techniques de descente d'échelle climatique permettent d'évaluer l'impact du changement climatique à l'échelle locale ou à l'échelle régionale à partir de simulations climatiques globales de basse résolution (telles que celles réalisées dans le cadre du GIEC). Ces approches permettent d'améliorer les simulations globales à basse résolution, pour évaluer plus précisément l'impact du changement climatique dans une région spécifique.

Dans le cadre du projet RNR-CP, nous nous sommes reposés sur la méthode de descente d'échelle dite "dynamique". Cette dernière est basée sur la réalisation de simulations climatiques à haute résolution spatiale, elles mêmes démarrées à partir des simulations climatiques à basse résolution à améliorer. Cette approche, considérée comme la plus fiable (mais aussi la plus coûteuse), s'applique aussi bien à l'étude des précipitations, qu'à celle de l'activité cyclonique dans son ensemble et nous a donc, pour cette raison, semblé plus pertinente.

L'autre approche, communément appelée "approche statistique", repose sur l'utilisation de données in-situ obtenues à l'échelle locale pour établir des fonctions de transfert qui, une fois appliquées aux données issues de modèles de climat à basse résolution, permettent d'évaluer les changements dans le futur. Cette approche statistique, moins couteuse mais également moins précise, n'a cependant pu être mise en œuvre du fait du manque de séries d'observations suffisamment longues disponibles dans la région.

Ces travaux réalisés et résultats obtenus sont fournis ci-après sous la forme de deux articles scientifiques.

Le premier article a été publié en 2020, par Julien CATTIAUX et collaborateurs, dans la revue Journal of Climate. Il revient, dans sa première partie, sur la réalisation et les caractéristiques des simulations climatiques utilisées dans le cadre du projet pour mettre en œuvre une descente d'échelle dynamique au moyen du modèle ARPEGE-Climat de Météo-France.

Le second article a été publié en 2021 dans la revue Atmosphere par Alberto MAVUME et collaborateurs. Il décrit, dans sa première partie, l'approche utilisée par les chercheurs mozambicains de l'INAM et de l'UEM pour mettre en oeuvre une descente d'échelle dynamique à partir des données disponibles librement dans le cadre du projet COordinated Regional Downscaling EXperiment (CORDEX-Africa).

Projected Changes in the Southern Indian Ocean Cyclone Activity Assessed from High-Resolution Experiments and CMIP5 Models

JULIEN CATTIAUX AND FABRICE CHAUVIN

Centre National de Recherches Météorologiques, Université de Toulouse, CNRS, Météo-France, Toulouse, France

OLIVIER BOUSQUET, SYLVIE MALARDEL, AND CHIA-LUN TSAI

Laboratoire de l'Atmosphère et des Cyclones, Université de la Réunion, CNRS, Météo-France, Saint-Denis, France

(Manuscript received 2 August 2019, in final form 7 March 2020)

ABSTRACT

The evolution of tropical cyclone activity under climate change remains a crucial scientific issue. Physical theory of cyclogenesis is limited, observational datasets suffer from heterogeneities in space and time, and state-of-the-art climate models used for future projections are still too coarse (~100 km of resolution) to simulate realistic systems. Two approaches can nevertheless be considered: 1) perform dedicated high-resolution (typically <50 km) experiments in which tropical cyclones can be tracked and 2) assess cyclone activity from existing low-resolution multimodel climate projections using large-scale indices as proxies. Here we explore these two approaches with a particular focus on the southern Indian Ocean. We first compute high-resolution experiments using the rotated-stretched configuration of our climate model (CNRM-CM6-1), which is able to simulate realistic tropical cyclones. In a 2-K warmer world, the model projects a 20% decrease in the frequency of tropical cyclones, together with an increase in their maximum lifetime intensity, a slight poleward shift of their trajectories, and a substantial delay (about 1 month) in the cyclone season onset. Large-scale indices applied to these high-resolution experiments fail to capture the overall decrease in cyclone frequency, but are able to partially represent projected changes in the spatiotemporal distribution of cyclone activity. Last, we apply large-scale indices to multimodel CMIP5 projections and find that the seasonal redistribution of cyclone activity is consistent across models.

1. Introduction

Understanding how climate change may influence tropical cyclone (TC) activity remains a challenging scientific issue (Knutson et al. 2010; Walsh et al. 2016). As TCs cause local devastating impacts and play a crucial role in maintaining regional water resources, this question also receives particular public attention.

Detecting potential trends in observational data is limited by the quality of historical records and the difficulty to disentangle the climate change signal from the noise of internal variability. A few studies have analyzed the International Best Track Archive for Climate Stewardship (IBTrACS) database, which compiles the best track datasets from diverse centers (Knapp et al. 2010). Various trends have been reported, such as an increase and a poleward shift in the TC lifetime maximum intensity (Kossin et al. 2013; Holland and Bruyère 2014) or a slowdown of the translation speed (Kossin 2018), but it remains unclear whether these trends result from data heterogeneities (e.g., introduction of new satellites), natural variability, or anthropogenic forcings. Therefore, so far, most assessments regarding the evolution of TCs in a warmer world have been made from theoretical and/or modeling studies.

There is a theoretical expectation that a warmer climate would undergo stronger TCs, in line with higher sea surface temperatures (SST) and increased potential intensity (Emanuel 1988). However, no such robust conclusion exists for changes in TC frequency due to the lack of a generally accepted theory for cyclogenesis, even if progress has been made on identifying the environmental conditions favoring cyclone activity (e.g., Held and Zhao 2011; Peng et al. 2012; Sugi et al. 2012).

Modeling studies addressing the evolution of TCs under climate change face an implacable issue: grid resolution must be high enough to simulate realistic

Corresponding author: Julien Cattiaux, julien.cattiaux@meteo.fr

DOI: 10.1175/JCLI-D-19-0591.1

TCs and experiments must be long enough—or enroll enough ensemble members—to isolate climate change from natural variability. The current generation of global models used for future climate projections—i.e., participants of the phase 5 of the Coupled Model Intercomparison Project (CMIP5)—have a horizontal grid spacing of about 100 km or greater (Taylor et al. 2011), which is too coarse to simulate realistic TCs (Camargo 2013); interestingly, the upcoming generation (CMIP6) will include a few models with higher resolutions (typically 50 km or higher). So far two approaches have thus been traditionally considered for studying TCs: (i) perform additional dedicated experiments at a higher resolution, or (ii) use the existing multimodel low-resolution climate projections to assess how large-scale environmental conditions favorable to cyclone activity may evolve in a warmer climate.

The first approach has been undertaken by a growing, but still limited, number of modeling centers that can afford the computer cost of high-resolution climate projections. Most of the performed experiments project a future reduction in the overall frequency of TCs, but an increase in the frequency of the strongest TCs (Walsh et al. 2016, and references therein). Also commonly reported are projected increases in associated phenomena, such as rainfall amounts and storm surges (Knutson et al. 2015; Woodruff et al. 2013).

The second approach consists of determining statistical relationships between cyclone activity and large-scale environmental factors, including dynamical (e.g., vertical and horizontal wind shear, low-tropospheric vorticity) and thermodynamical (e.g., midtropospheric humidity, sea surface temperature) variables. Combinations of these variables allow us to build cyclogenesis indices (CGIs), that have been shown to represent both the seasonal and geographical distribution of cyclone activity fairly well (Menkes et al. 2012). (Previous authors have used the abbreviation ''GPIs'' as the generic term for these indices, but since ''GPI'' is also an abbreviation used for one specific index used in this paper, here we use ''CGIs.'') Using CGIs to quantify potential changes in the cyclone activity is, however, questionable, as it assumes that statistical relationships established for present-day climatological features remain valid in a climate change context. In particular, it has been shown that CGIs fail to capture the decrease in TC frequency when applied to high-resolution climate projections (Camargo et al. 2014; Wehner et al. 2015; Chauvin et al. 2020), which may explain why attempts to apply CGIs to CMIP5 future projections have mostly remained inconclusive so far (Camargo 2013). However, the ability of CGIs to capture other potential changes in the cyclone activity (e.g., changes in the spatiotemporal distribution) has not been documented so far. In addition, since CGIs can be broken down into dynamical and thermal components, they can provide useful insights for the physical understanding of the projected changes in TC tracks.

Here we apply and compare both high-resolution and CGIs approaches to assess projected changes in cyclone activity and explore whether the two approaches can be reconciled on some aspects. We use the same methodology as in Chauvin et al. (2020) but we focus over the SIO basin, which has been seldom studied so far. Among the eight IBTrACS basins, it ranks third in terms of overall number of reported TCs (after the western and eastern Pacific basins). Even if less highly populated regions are exposed to TC hazards than in other basins, SIO TCs can still have dramatic impacts in Western Australia and southeastern Africa, including Madagascar and the Mascarene Islands (La Réunion, Mauritius, and Rodrigues), as recently illustrated by the devastating cyclone Idai.[1] In the western part of the SIO, the death toll associated with TCs averages to 20 fatalities per year over the last 19 years with 9 seasons above 100 fatalities according to the European Commission Joint Research Centre.[2] Long-term climate trend analysis in the SIO basin is particularly challenging due to the introduction of the *Meteosat-5* geostationary satellite into the region in 1998, which causes a temporal heterogeneity in observational and reanalysis products (Kuleshov et al. 2010; Kossin et al. 2013). Evidences for an observed increase in the number of severe TC days have nevertheless been reported in the western part of the SIO (Kuleshov et al. 2010; Malan et al. 2013). High-resolution climate projections suggest that SIO TCs follow the global behavior: a decrease in the overall frequency and an increase in the intensity (e.g., Murakami et al. 2012; Walsh et al. 2016).

The paper is structured as follows. Observations, reanalyses, high-resolution experiments, and CMIP5 models used in this study are presented in section 2. Methodologies including the tracking algorithm applied to high-resolution data and the cyclogenesis indices applied to lower-resolution data are detailed in section 3. Section 4 contains our main findings while discussion and conclusions are provided in sections 5 and 6.

[1] https://public.wmo.int/en/media/news/tropical-cyclone-idai-hits-mozambique.

[2] Emergency Reporting 23: http://www.gdacs.org/Public/download.aspx?type=DC&id=161.

TABLE 1. Observations, reanalyses, and CNRM-CM experiments used in this study. Time periods correspond to Southern Hemisphere convention for cyclone seasons (i.e., 1980 is July 1979–June 1980).

Abbreviation	Name	Details	Resolution (km)	Time period	TC tracks
IBTr	IBTrACS	TC track observations	—	1980–2016	×
ERAI	ERA-Interim	Reanalysis	80	1980–2016	
ERA5	ERA-5	Reanalysis	30	1980–2016	×
T127	CNRM-CM5	Historical simulation	155	1976–2005	
T359	CNRM-CM6-HR	AMIP simulation	55	1980–2010	×
SIO-P	CNRM-CM6-HR r.-s.	Experiment forced by historical SST	10–50	1971–2014	×
SIO-F	CNRM-CM6-HR r.-s.	Experiment forced by RCP8.5 SST	10–50	2051–94	×

2. Data

a. Observations and reanalyses

Observations and reanalyses used in this study are summarized in Table 1. Observational TC data are taken from the IBTrACS, version 4, dataset released in April 2019 that provides best track characteristics (e.g., position, sea level pressure, maximum sustained winds) on a 3-hourly basis (https://www.ncdc.noaa.gov/ibtracs/, Knapp et al. 2010). For consistency with model and reanalysis data used in this study, we restrict IBTrACS data to the period July 1979–June 2016 (i.e., cyclone seasons 1980–2016) and the hours 0000, 0600, 1200, and 1800 UTC. We only use information provided by the World Meteorological Organization (WMO) Regional Specialized Meteorological Centres (RSMCs): Météo-France La Réunion and the Australian Bureau of Meteorology (BoM) for the SIO basin. We only consider systems that are indicated as ''TS'' (tropical storms) in the metadata and that reach the official *moderate tropical storm* (category 1) stage according to Météo-France (BoM) classifications (i.e., 10-min sustained winds above $18\,m\,s^{-1}$) at least once in their lifetime. (Note that we use the terminology of the local RSMCs in this paper, not the Saffir–Simpson scale.)

ERA-5 data (30-km resolution, Hersbach et al. 2018) are used for both TC tracking and computing CGIs. ERA-Interim data (80-km resolution, Dee et al. 2011) are also used for computing CGIs, which allows for a fair comparison with CMIP5 models as they do no simulate realistic TCs (contrarily to ERA-5). Both datasets are downloaded from the European Centre for Medium-Range Weather Forecasts (https://www.ecmwf.int/en/forecasts/datasets/browse-reanalysis-datasets), on a regular 0.5° × 0.5° longitude–latitude grid and at a 6-hourly frequency over the period July 1979–June 2016 (i.e., cyclone seasons 1980–2016).

b. High-resolution experiments

We use the same experimental setup as in Chauvin et al. (2020), which consists in performing atmosphere-only present-day and future experiments with the Centre National de Recherches Météorologiques Coupled Global Climate Model (CNRM-CM) in its rotated-stretched configuration. The atmospheric component of CNRM-CM (ARPEGE) has indeed the particularity to enable a deformation of its horizontal grid: the pole can be placed over a location of interest (here, the SIO), and a stretching factor can be applied to progressively increase (decrease) the resolution around the pole (the antipode). The advantage of this configuration is that it provides high-resolution simulations over the area of interest, while preserving the consistency of the large-scale dynamics between global and regional scales. This technique has been extensively validated as it is routinely utilized by Météo-France for operational numerical weather prediction over Europe and has also been used in numerous studies of TCs over the North Atlantic basin (e.g., Chauvin et al. 2006; Daloz et al. 2012; Chauvin et al. 2020).

In the present study, the stretching is applied to a T359 grid (720 × 360 points), the pole is located at 12.5°S, 55°E, and the stretching factor is 3.5, resulting in a 14–50-km effective resolution within the SIO domain (defined as 0°–30°S, 30°–120°E; see Fig. 1a). The choice of the exact grid pole location was made in order to have the highest-resolution increase in the area under the responsibility of the Météo-France RSMC on La Réunion Island. The model is run with a 15-min time step. We use the same version of ARPEGE as in Chauvin et al. (2020) (i.e., a version close to the one participating to CMIP6 through CNRM-CM6-1 and CNRM-ESM2 models). A comprehensive description of this version, including details on convection, microphysics, and turbulence parameterizations, can be found in Voldoire et al. (2019), together with an evaluation of the CNRM-CM6-1 model.

Similarly to Chauvin et al. (2020), two experiments are conducted with the rotated-stretched configuration: a present-day simulation over the period 1971–2014 (named SIO-P), using historical SST and radiative forcings, and a future simulation over the period 2051–94

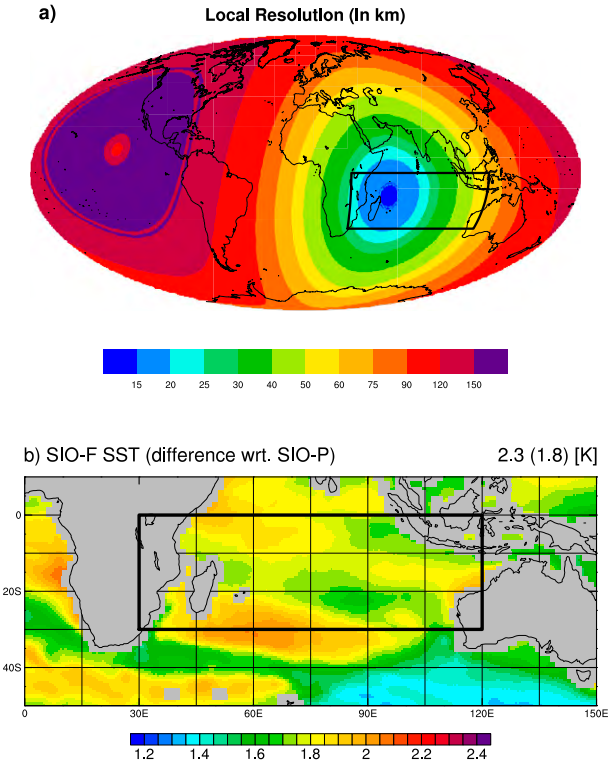

FIG. 1. (a) Effective grid resolution (km) of the rotated–stretched experiments. (b) Mean difference between prescribed SST (K) of SIO-F and SIO-P experiments.

(named SIO-F), using future SST and radiative forcings corresponding to the 8.5 W m^{-2} radiative concentration pathway (RCP8.5). Prescribed SST are taken from a member of CNRM-CM5 historical 1 RCP8.5 simulations (namely, the run r1i1p1; Voldoire et al. 2013), and are bias corrected over the present-day period with respect to the HadISST dataset (Rayner et al. 2003). Further methodological details, including the treatment of sea ice, are provided in Chauvin et al. (2020). The time-averaged SST difference between the two experiments is a generalized warming ranging from 1.6 to 2 K over the SIO domain with a field average of 1.8 K (Fig. 1b); CNRM-CM5 is close to the CMIP5 multimodel mean on this aspect (not shown). To assess the potential benefits of the rotated-stretched configuration in simulating cyclones, a third experiment with a uniform T359 grid (denoted T359) is conducted over 1980–2010 using prescribed SST from HadISST.

c. CMIP5 simulations

We use monthly outputs of atmospheric temperature (ta), wind (ua, va), specific humidity (hus), convective precipitation (prc), sea level pressure (psl), and sea surface temperature (ts) from the historical + RCP8.5 simulations of 14 CMIP5 models (Table 2). This ensemble includes the CNRM-CM5 simulation from which SST are taken to perform the high-resolution experiments, which will be denoted T127 in the following. All fields are interpolated from the native model grid onto a common 2.5° × 2.5° longitude–latitude grid prior to any diagnostic computation. This is also the case for ERA-5 and ERA-Interim data when they are compared with CMIP5 data.

3. Methods

a. Tracking algorithm

As in Daloz et al. (2012) and Chauvin et al. (2020), we use the algorithm introduced and detailed in Chauvin et al. (2006) to track TCs in ERA-5 and SIO-P, SIO-F, and T359 experiments. The tracker is applied to 6-hourly outputs, and in this paper all the data are first interpolated onto a common 0.5° × 0.5° longitude–latitude

TABLE 2. CMIP5 models used in this study.

Abbreviation	Name	Country	Lon × lat	Resolution (km)
BCC	BCC-CSM1.1	China	2.8° × 2.8°	310
CCCMA	CanESM2	Canada	2.8° × 2.8°	310
CNRM	CNRM-CM5	France	1.4° × 1.4°	155
CSIRO	CSIRO-Mk3.6.0	Australia	1.9° × 1.9°	210
GFDL	GFDL-ESM2M	United States	2.0° × 2.5°	250
GISS	GISS-E2-R	United States	2.0° × 2.5°	250
INM	INM-CM4	Russia	1.5° × 2.0°	195
IPSL	IPSL-CM5A-LR	France	1.9° × 3.8°	300
MIROC	MIROC-ESM	Japan	2.8° × 2.8°	310
MOHC	HadGEM2-ES	United Kingdom	1.3° × 1.9°	180
MPIM	MPI-ESM-LR	Germany	1.9° × 1.9°	210
MRI	MRI-CGCM3	China	1.1° × 1.1°	120
NCAR	CCSM4	United States	0.9° × 1.3°	120
NCC	NorESM1	Norway	1.1° × 1.1°	120

grid (i.e., the effective grid of the T359 experiment and the resolution chosen for the download of ERA-5 data) in order to allow for a fair comparison. The tracking algorithm involves three steps:

1) At each time step, grid points potentially concerned by a TC are identified, based on the main criteria that depict TCs: sea level pressure is a local minimum (low pressure system), 850-hPa vorticity exceeds a threshold (strong vortex), 10-m wind speed exceeds a threshold (strong winds), mean 700–300-hPa temperature local anomaly exceeds a threshold (warm core), tangential wind speed is higher at 850 hPa than at 300 hPa (stronger winds at low levels due to the thermal wind relationship), temperature local anomaly is higher at 300 hPa than at 850 hPa (warmer core at high levels). (Thresholds are discussed below.) Note that there is no latitude criterion, so that the detection can potentially occur outside the tropics.
2) TC points identified in step 1 are connected across consecutive time steps to build TC tracks. The association procedure is described in detail in Chauvin et al. (2006).
3) Tracks are completed before and after the TC stage in order to include cyclogenesis and cyclolysis. This is done by relaxing all criteria except vorticity and rerunning the algorithm backward (forward) from the first (last) point of the previously identified TC track. This step also ensures that a system reaching the TC stage twice (or more) in its lifetime is counted as a unique system.

The algorithm is highly sensitive to the thresholds used in step 1 that primarily depend on the data resolution. Here, the thresholds have been calibrated by repeating the tracking procedure on ERA-5 over 2011–16 with various combinations of thresholds and comparing the resulting tracks to IBTrACS. The retained values are $20 \times 10^{-5}\,s^{-1}$ for vorticity, $13\,m\,s^{-1}$ for wind speed, and 1 K for local temperature anomaly. With these values, the algorithm detects most of IBTrACS trajectories in ERA-5, with a limited number of false or missed tracks (see example of cyclone season 2015 in Fig. 2 and further details in section 4). Note that a perfect correspondence between IBTrACS and ERA5 tracks was not expected due to (i) IBTrACS specificities, (ii) potential model errors, and (iii) potential impacts of data assimilation on TCs.

We distinguish three stages in the tracks resulting from the algorithm: the development stage [from the system initiation (or cyclogenesis) to its intensification into a TC], the TC stage (encompassing all TC points with possible temporary interruptions), and the cyclolysis stage (from the last TC point to the end of the track). For consistency, we also distinguish these three stages in IBTrACS, but on the basis of the $18\,m\,s^{-1}$ wind speed threshold: development stage from the track start to the first exceedance, then TC stage until the last exceedance, then cyclolysis stage.

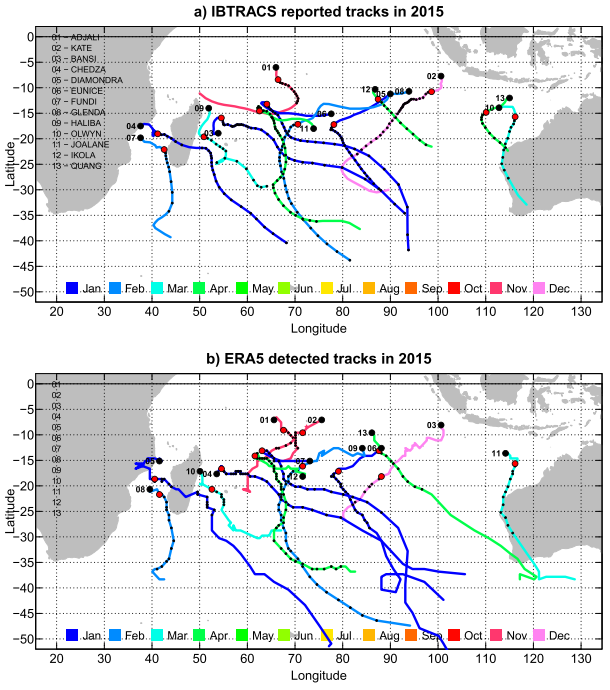

FIG. 2. (a) TC tracks reported in IBTrACS for the 2015 season. (b) TC tracks resulting from the tracking algorithm applied to ERA5 for the 2015 season. Dots along trajectories indicate TC points, with thick black dots for the first point of the system (genesis point) and thick red dots for the first point of the TC stage (intensification point). Track colors indicate the month of the track starting point (genesis).

b. *Cyclogenesis indices (CGIs)*

The link between cyclone activity and large-scale environmental conditions is assessed using CGIs from the existing literature. We use the three indices evaluated on seasonal and interannual time scales by Menkes et al. (2012), and used separately by Royer and Chauvin (2009), Camargo (2013), and Chauvin et al. (2020) in a climate change perspective:

- the CYGP index introduced by Royer et al. (1998), after Gray (1975);
- the GPI index introduced by Emanuel and Nolan (2004);
- the TCS index introduced by Tippett et al. (2011) (hereafter referred as TIPP in order to avoid confusion with the TCs acronym used for "tropical cyclones").

All indices are computed at the gridpoint scale and on a monthly basis (i.e., calculated with monthly mean climate data). They are constructed as multiplicative functions of dynamical and thermal variables that result

from empirical fits between observed cyclone activity and reanalyzed large-scale variables. Dynamical variables are the same for the three indices used in this paper (low-level vorticity and vertical wind shear) while thermal variables differ. More precisely, the indices are as follows:

$$\mathrm{CYGP} = \beta_{\mathrm{CYGP}} \times \underbrace{|f|\left(\zeta_r \frac{f}{|f|} + 5\right)(V_{\mathrm{shear}} + 3)^{-1}}_{\text{Dynamical}} \times \underbrace{\max(P_c^* - 3, 0)}_{\text{Thermal}}, \quad (1)$$

$$\mathrm{GPI} = \beta_{\mathrm{GPI}} \times \underbrace{|10^5\zeta|^{3/2}(1 + 0.1V_{\mathrm{shear}})^{-2}}_{\text{Dynamical}} \times \underbrace{\left(\frac{H}{50}\right)^3 \left(\frac{V_{\mathrm{pot}}}{70}\right)^3}_{\text{Thermal}}, \quad (2)$$

$$\mathrm{TIPP} = \beta_{\mathrm{TIPP}} \times \underbrace{\cos(\varphi)\exp(1.03\zeta - 0.15V_{\mathrm{shear}})}_{\text{Dynamical}} \times \underbrace{\exp(0.05H + 0.56\mathrm{SST}_{\mathrm{loc}})}_{\text{Thermal}}, \quad (3)$$

where f is the Coriolis parameter, φ is the latitude, ζ (ζ_r) is the absolute (relative) vorticity at 850 hPa, $V_{\mathrm{shear}} = \Delta V/\Delta p$ is the vertical wind shear between 850 and 200 hPa, $P_c^*$is the convective precipitation, H is the relative humidity at 600 hPa, $\mathrm{SST}_{\mathrm{loc}} = \mathrm{SST} - \overline{\mathrm{SST}}^{(20\mathrm{S}-20\mathrm{N})}$ is the local SST anomaly relative to the tropics (20°S–20°N), and V_{pot} is the TC potential intensity introduced by Emanuel (1988) that we calculate using the pcmin_2013.f routine distributed by K. Emanuel.[3] For the three indices, the β coefficient is a scaling factor that allows to interpret global maps of CGIs as densities of TCs; here we systematically tune these scaling factors so that the global sum of CGIs equals 84 (TCs per year over the globe) over the present-day period, and we keep the same β for computing indices over future periods. More details about the computation of these three indices can be found in the appendix of Menkes et al. (2012).

It is important to note that in this paper, we use the exact same equations for all reanalysis or model data on which we compute CGIs. In particular the numerical constants that are present in the above equations are the ones used by Menkes et al. (2012), and they correspond to the ones originally introduced by the respective authors. Camargo et al. (2014) suggest that CGIs perform better in capturing climate-related changes in cyclone activity when they are refitted for the model of interest (including the selection of predictors). Here we consider that such a model-dependent computation of CGIs is outside the scope of our study, and that using the exact same definition for CGIs allows for a fair comparison between models. Last, for the sake of simplicity, results are mainly shown for the average of the three indices (hereafter the aggregate CGI), and behaviors of individual indices are only mentioned in the text when they substantially differ from the mean. Considering the average of CGIs also tends to emphasize signals that are common—thus robust—across individual indices.

As CGIs are written as multiplicative functions, differences between time averages over two periods of time (typically present-day vs future) can be broken down into individual contributions of dynamical versus thermal components. Indeed, for each calendar month, if x_i (y_i) denotes the dynamical (thermal) component of the CGI for year i, and x_i' and y_i' denotes their anomalies relative to their time averages $\overline{x}$ and $\overline{y}$, the time-averaged CGI over either the present-day (P) or the future (F) period is

$$\overline{\mathrm{CGI}} = \overline{x_i y_i} = \overline{(\overline{x} + x_i')(\overline{y} + y_i')} = \overline{x}\,\overline{y} + \overline{x_i' y_i'}. \quad (4)$$

Thus, the $F - P$ difference (denoted Δ) in time-averaged CGI is

$$\Delta\overline{\mathrm{CGI}} = \overline{\mathrm{CGI}}^F - \overline{\mathrm{CGI}}^P = \overline{x}^F\overline{y}^F - \overline{x}^P\overline{y}^P + \underbrace{\overline{x_i' y_i'}^F - \overline{x_i' y_i'}^P}_{\varepsilon}, \quad (5)$$

with ε the residual term resulting from dependencies between monthly anomalies of x_i and y_i. Finally, since $\overline{x}^F = \overline{x}^P + \Delta\overline{x}$ and $\overline{y}^F = \overline{y}^P + \Delta\overline{y}$, one can write

$$\Delta\overline{\mathrm{CGI}} = \underbrace{\overline{y}^P\Delta\overline{x}}_{\text{Dynamical}} + \underbrace{\overline{x}^P\Delta\overline{y}}_{\text{Thermal}} + \underbrace{\Delta\overline{x}\Delta\overline{y} + \varepsilon}_{\text{Residual}}, \quad (6)$$

where $\overline{y}^P\Delta\overline{x}$ is the contribution of dynamical changes only, and $\overline{x}^P\Delta\overline{y}$ is the contribution of thermal changes only. In the following, the last two terms $\Delta\overline{x}\Delta\overline{y}$ and ε are grouped into a single residual term, which is systematically shown in the figures but not commented in the text. The decomposition is performed for each calendar month separately and then averaged over the season or the year.

4. Results

a. Analysis of high-resolution experiments

1) Realism of simulated TCs

To assess the realism of TCs simulated by the different model configurations, we first analyze the statistical

[3] ftp://texmex.mit.edu/pub/emanuel/TCMAX/.

distribution of the annual minimum of sea level pressure in the SIO basin (Fig. 3a). Observed values are taken from IBTrACS assuming that annual minima of sea level pressure systematically occur within TCs. Over 1980–2016 the median is found to be 915 hPa; this means that such a low pressure is reached by at least one system over the SIO basin every 2 years on average. ECMWF reanalyses are unable to simulate pressures lower than 950 hPa, although a notable improvement is seen in ERA-5 relative to ERA-Interim (likely due to the increase in resolution). Uniform CNRM-CM configurations (T127 and T359) also fail to simulate extremely low pressures, although one outlying system reaches 905 hPa in the T359 experiment. The CNRM-CM5 (CNRM-CM6-1) model nevertheless simulates lower pressures than ERA-Interim (ERA-5) while it has a slightly coarser resolution; one reason could be that in reanalyses, data assimilation tends to spatially smooth low pressure systems when centers of action are slightly shifted between assimilated observations and forecast background. The added value of the rotated-stretched configuration in the present-day climate (SIO-P) is evident from Fig. 3a: this experiment is able to simulate lower pressures than observed (e.g., below 900 hPa), even if the median of the annual minimum pressure distribution remains slightly higher than observed (~930 hPa).

Once the tracking is done, the realism of resulting TCs is evaluated from the statistical relationship between the minimum sea level pressure and the maximum wind speed along the track (Fig. 3b). Both variables are indeed strongly correlated, as evidenced in TC observations (IBTrACS) and shown by Atkinson and Holliday (1977). Such a relationship is well captured by present-day model experiments (T359, SIO-P), although the model exhibits stronger winds than IBTrACS for a given pressure especially in the rotated-stretched configuration. The uniform experiment (T359) nevertheless struggles to simulate strong TCs (only two systems with pressure below 930 hPa and wind speed above 50 m s^{-1}) while the rotated-stretched experiment (SIO-P) can generate stronger TCs than the most intense TC recorded in IBTrACS. This result was also found by Chauvin et al. (2020) over the North Atlantic basin. Despite its fine resolution, ERA-5 fails to reproduce the strength of observed TCs. Note that a fair comparison between winds of IBTrACS, ERA-5, and ARPEGE experiments is, however, difficult since one compares wind output at a given time step and grid point (model) with 10-min sustained winds at the local cyclone scale (IBTrACS).

Finally, a first evaluation of the projected changes in TC characteristics can be assessed from these diagnostics: here we find no clear difference in the pressure–wind relationship between the SIO-P and the SIO-F

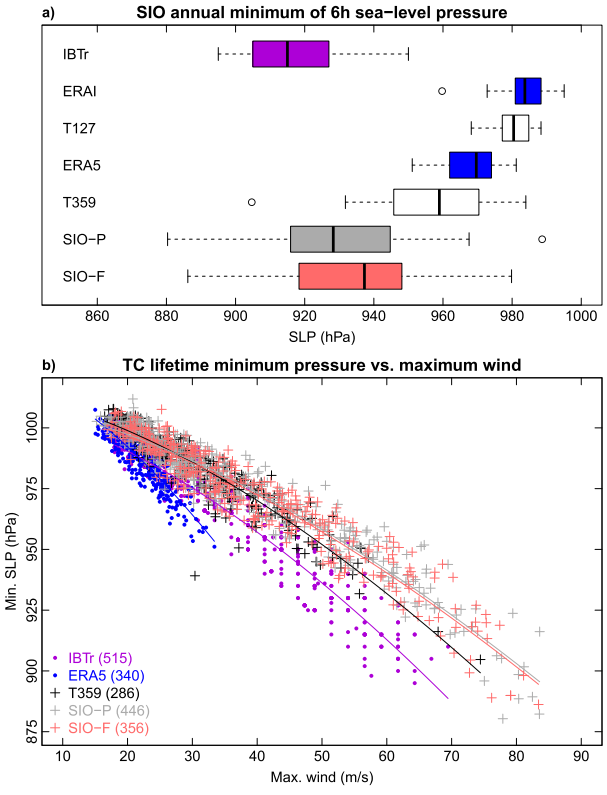

FIG. 3. (a) Distribution of the annual minimum of 6-h SLP (hPa) across the SIO domain (0–30°S, 30°–120°E) for IBTrACS (1980–2016, violet), ERAI and ERA5 (1980–2016, blue), T127 (1976–2005) and T359 (1981–2010) uniform experiments (white), and SIO-P (1971–2014, gray) and SIO-F (2051–94, red) rotated–stretched experiments. In all boxplots used in this paper, the box represents the first and third quartiles, the band inside is the median, the whiskers expand to the largest values still within the 1.5 interquartile range from the box, and the small circles indicate outliers. (b) Lifetime minimum SLP (p) as function of lifetime maximum wind (V) for all TCs reported in IBTrACS and detected in ERA5, T359, SIO-P, and SIO-F [periods and colors are as in (a)]. Fits are added following Atkinson and Holliday (1977) (i.e., assuming $p = a + bV^{1/0.644}$ with a and b the coefficients to be fitted).

experiments (Fig. 3b), and although the SIO-F distribution of the annual minimum of sea level pressure seems slightly shifted toward higher pressures than SIO-P (Fig. 3a), the difference between the two samples is not statistically significant (p value of about 0.5). Changes in TC characteristics are thus more carefully scrutinized in the following.

2) ANALYSIS OF TC FREQUENCY

On average, 13.9 TCs per year are reported in the SIO domain by IBTrACS (Fig. 4a). As the average number of TC days per system is found to be 5.2 days, it leads to an annual number of TC days of 73 days (Fig. 4b). The tracking algorithm has been calibrated on ERA-5 over 2011–16 (section 3); on average over these years, it

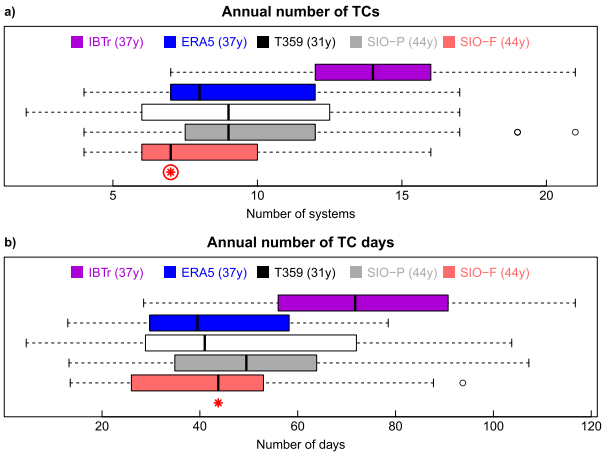

FIG. 4. (a) Distribution of the annual number of TCs in the SIO domain for IBTrACS (violet), ERA5 (blue), T359 (white), SIO-P (gray), and SIO-F (red). (b) As in (b), but for the annual number of TC days. Red (circled) asterisks indicate differences between SIO-P and SIO-F averages that are significant at the 90% (95%) level following a *t* test.

detects 11 TCs and 54 TC days per year (vs 12.5 TCs and 63 TC days per year in IBTrACS). Over the whole time period 1980–2016, the tracking algorithm applied to ERA-5 more substantially underestimates the observed number of both TCs (9 vs 13.9 yr^{-1}) and TC days (42 vs 73 TC days yr^{-1}). This inconsistency is the strongest at the beginning of the time period and progressively decreases with time (not shown), which questions the temporal homogeneity of IBTrACS and/or ERA-5 over the SIO. However, a more detailed evaluation is left for future studies.

T359 and SIO-P experiments simulate a similar amount of TCs (9.2 and 10.1 on average, distribution in Fig. 4a) and TC days (51 vs 52 on average, distribution in Fig. 4b). This suggests that the uniform 50-km resolution of the T359 experiment is potentially sufficient to generate a realistic number of TCs, albeit with weaker intensity than in the rotated-stretched configuration (see previous section and Fig. 3). The SIO-F experiment produces about 20% less TCs than the SIO-P experiment (8.1 yr^{-1} on average), which is qualitatively consistent with the broadly reported future decrease in TC frequency (e.g., Walsh et al. 2016) and quantitatively agrees with results of Murakami et al. (2012). This 20% decrease in the frequency is significant at the 95% level; as it is associated with a slight increase in TC duration (5.5 vs 5.1 TC days per system), the decrease in the annual number of TC days in less statistically significant (90% level, 44 vs 52 days). (This increase in TC duration is further detailed below with the TC intensity.)

In the SIO, TCs preferably develop close to the center of the basin (10°–15°S, 60°–80°E), the Mozambique channel, and close to the Australian shore (Fig. 5a). This spatial pattern is well captured by ERA-5, confirming that the tracking algorithm applied to the reanalysis is able to detect part of the TCs reported in IBTrACS (Fig. 5b, spatial correlation of 0.90 with Fig. 5a). T359 and SIO-P experiments tend to simulate too little (much) TC intensification in the center (south) of the basin (Figs. 5c,d, spatial correlations of 0.62 and 0.51 with Fig. 5a). This might reflect a systematic bias of the CNRM-CM6-1 model since a similar behavior was reported by Chauvin et al. (2020) over the North Atlantic basin; future studies will investigate the origins of this geographical bias. The rotated-stretched configuration (SIO-P) results in an enhanced number of TCs in the SIO relative to the uniform configuration; symmetrically, less systems are simulated in other basins. A few systems have their intensification point outside the tropics (even south of 30°S) in the model; these can be either systems that have developed in the tropics and reached the TC stage after an extratropical transition, or systems that have developed outside the tropics but still meet the criteria to be detected as TC by the tracking algorithm. We have decided not to filter these systems out; in particular the use of a fixed latitude criterion would have been questionable in a climate change context. A small number of such extratropical systems is also detected in ERA-5 by the tracking algorithm.

In agreement with Fig. 4, SIO-F simulates globally fewer TCs than SIO-P, especially northeast of the Mascarene Islands (Fig. 5e). Although the signal is noisy due to the limited number of systems (446 in SIO-P vs 356 in SIO-F), more TC intensification is observed south of the Mozambique and west of Australia. Similar conclusions arise from analyzing densities of full TC tracks that are smoother due to the greater number of points included (Figs. 5f–j). In particular, the SIO-F versus SIO-P difference reveals a general northwest–southeast dipole (with the exception of the Mozambique channel), consistent with a poleward shift of TC tracks superimposed with a general decrease in the number of TCs.

3) ANALYSIS OF TC INTENSITY

Consistent with Fig. 3b, TCs simulated by the uniform T359 experiment are weaker than reported in IBTrACS, as illustrated by both the lifetime minimum pressure (983 vs 962 hPa on average, Fig. 6a) and maximum wind speed (31 vs 36 m s^{-1} on average, Fig. 6b). This bias is partly corrected in the rotated-stretched configuration (SIO-P, 975 hPa and 37 m s^{-1} on average). TC intensity is significantly increased in the SIO-F experiment (971 hPa and 39 m s^{-1} on average), which is again in line with the existing literature (e.g., Walsh et al. 2016). Interestingly, most of this increase in intensity arises

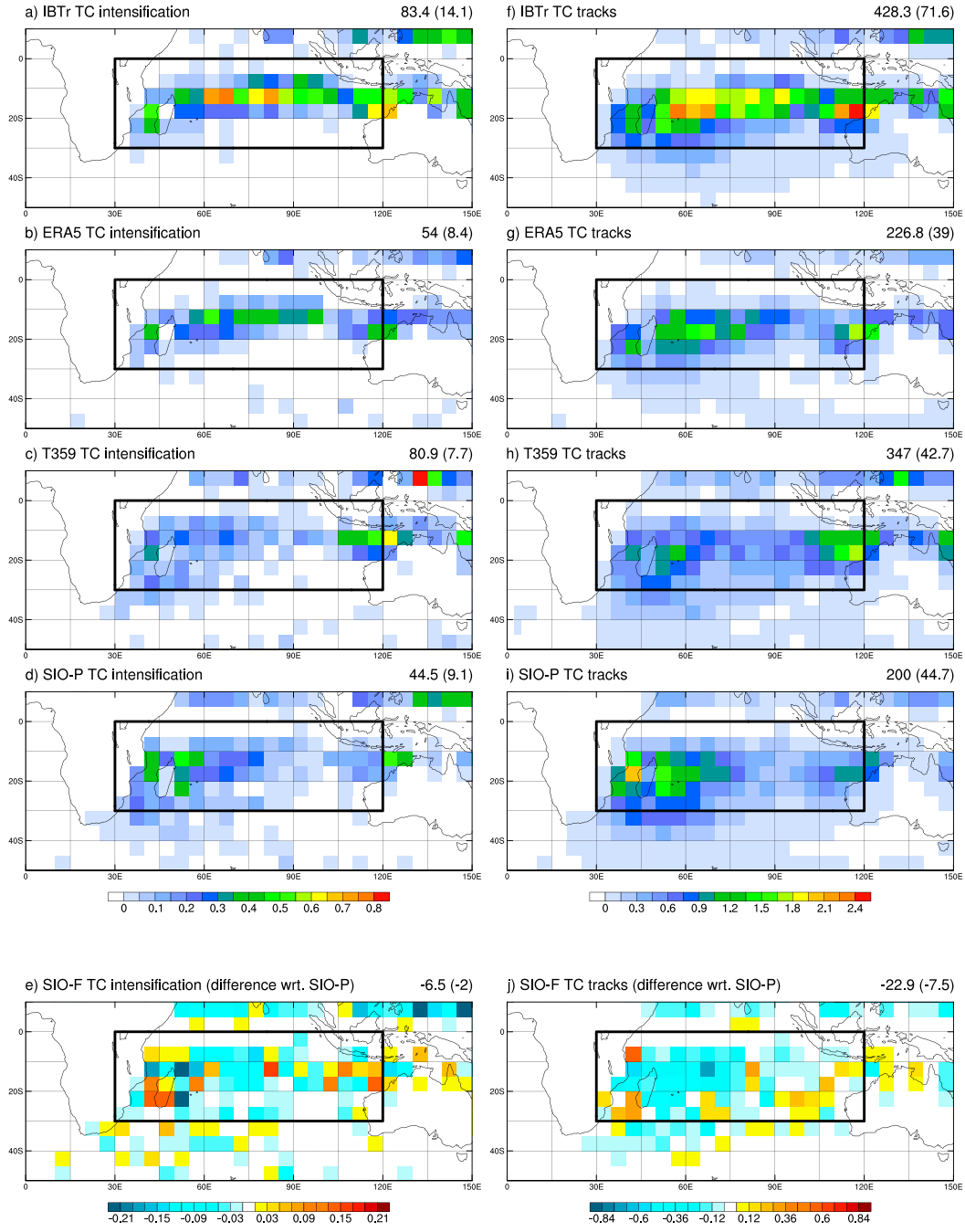

FIG. 5. (a)–(e) Frequency of TC intensification points (i.e., first TC point for each trajectory) (in number of points per year and per 5° × 5° grid box) for (a) IBTrACS, (b) ERA5, (c) T359, (d) SIO-P, and (e) SIO-F represented as a difference relative to (d). (f)–(j) As in (a)–(e), but for TC tracks (i.e., all TC points for each trajectory). Sums over the globe and for the SIO domain (in parentheses) are indicated in the top-right corner of each panel.

from the core of the distribution: TCs with an intensity below the median of the present-day distribution occur less frequently in the future experiment (40% of TCs in SIO-F vs 50% in SIO-P by definition), while TCs with an intensity between the 60th and 80th percentiles of the present-day distribution are more frequent (30% vs 20% by definition). (Values are similar for both minimum pressure and maximum wind.) Extremely intense TCs also contribute to the intensity increase: about 6%–7% of the future TCs exceeds the 95th percentile of the present-day intensity distribution (low pressure or high winds), so that even if the overall number of TCs

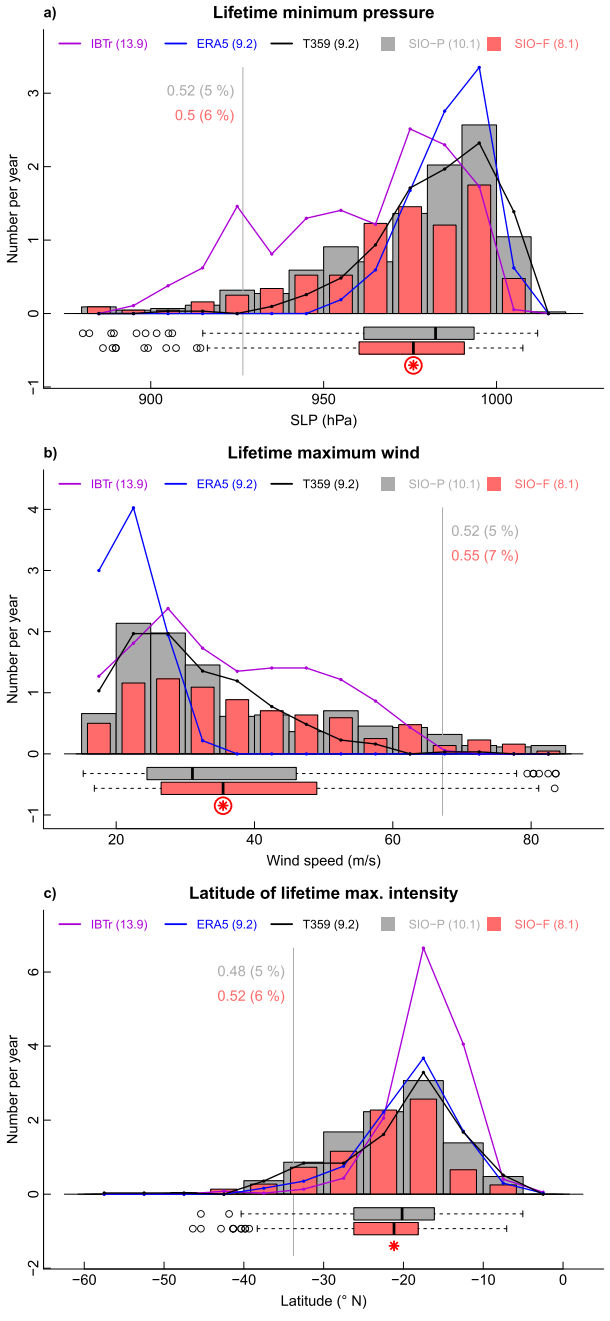

FIG. 6. (a) Frequency histogram (in number of systems per year) of the TC lifetime minimum pressure (hPa) for IBTrACS (violet line), ERA5 (blue line), T359 (black line), SIO-P (gray bars), and SIO-F (red bars). (b) As in (a), but for the lifetime maximum wind ($m\ s^{-1}$). (c) As in (a), but for the latitude of the lifetime minimum pressure (°N). For SIO-P and SIO-F, probability distributions are also represented (boxplots). Red (circled) asterisks indicate differences between SIO-P and SIO-F averages that are significant at the 90% (95%) level following a *t* test.

decreases by 20% (Fig. 4), the number of extremely intense TCs remains constant (about $0.5\ yr^{-1}$ with this definition). Similar results are obtained from the accumulated cyclone energy (not shown).

The increase in TC intensity in the rotated-stretched experiments is associated with a 90% level significant poleward shift of the lifetime maximum intensity (Fig. 6c). Although this is qualitatively consistent with the literature (e.g., Kossin et al. 2013), here we find a relatively weak shift of about 1°S in 80 years (22.3°S for SIO-F vs 21.3°S for SIO-P on average). This shift is related to a poleward extension of the tracks: while latitudes of genesis and intensification do not change significantly, the latitude of cyclolysis is shifted by 1.4°S on average (26.9° vs 25.5°S). Model biases in the spatial density of tracks (Fig. 5) are reflected in the distribution of the latitude of maximum lifetime intensity: too many (few) tracks at high (low) latitudes. Part of the discrepancy between model experiments and IBTrACS could arise from the tracking algorithm, since the ERA-5 distribution shows a similar poleward displacement.

Last, the increase in TC intensity is also related to a slightly longer TC stage (5.7 vs 5.4 days on average) that incorporates more TC days (5.5 vs 5.1 on average). Over the whole system lifetime, this increase is compensated by decreases in the duration of both development (1.9 vs 2.1 days) and cyclolysis (2.4 vs 2.5 days) stages; however, only the shorter development stage is statistically significant at the 95% level (not shown). (The terminology of the different stages is defined in section 3a.)

4) ANALYSIS OF SEASONAL CYCLE

An interesting feature revealed by the rotated-stretched experiments is that the cyclone season is found to be shorter under future climate conditions (Fig. 7). In the SIO-P experiment, the first (last) TC of the season—July to June—starts on average on 12 November (28 April), so that the cyclone season—defined here as the difference between these two dates—lasts on average 172 days. These values are very close to the uniform T359 experiment (12 November to 21 April, 165 days) and to the IBTrACS observations (7 November to 28 April, 177 days). In the SIO-F experiment, the season begins on average 32 days later (14 December), ends 9 days earlier (19 April), and thus lasts 41 days less than in SIO-P. The later onset and the shorter duration of the season are significant at the 95% level. These changes result from a strong decrease in the number of TCs occurring in the austral winter: in SIO-P, 17 TCs (3.8% on the total number) are detected during the months of June–September and 16 (3.6%) in October, versus 2 (0.6%) and 3 (0.8%), respectively, in SIO-F. Note that such wintertime systems are realistic: 9 systems are recorded over 1980–2016 in IBTrACS in

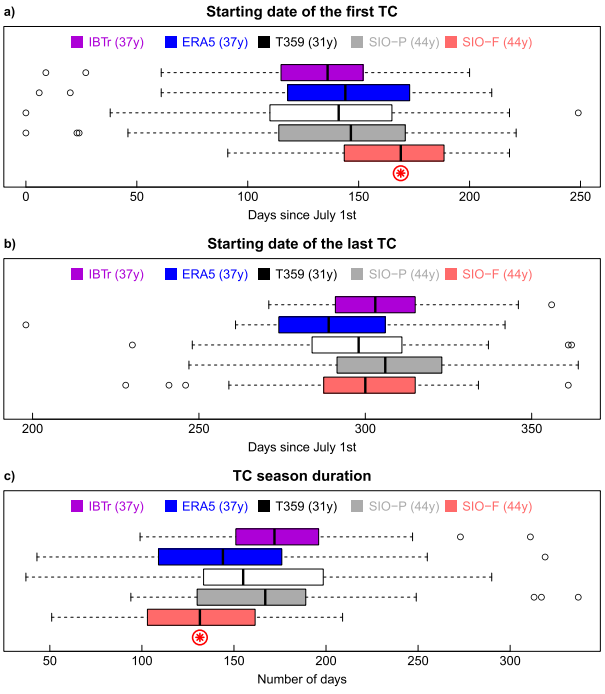

FIG. 7. As in Fig. 4, but for (a) the date of the first TC intensification within the season, (b) the date of the last TC intensification within the season, and (c) the TC season duration measured as the difference between (b) and (a).

June–September and 11 in October (i.e., 1.7% and 2.1% of the total number), with 6 systems reaching at least the *severe tropical storm* (category 2) stage (winds above 25 m s^{-1}), including one *tropical cyclone* (category 3) system (33 m s^{-1}; Oscar in October 1983) and two *intense tropical cyclone* (category 4) systems (47 m s^{-1}; Bellamine in October 1996 and Anais in October 2012) according to Météo-France (BoM) classifications (again, we use the terminology of the local RSMCs in this paper, not the Saffir–Simpson scale.). As a consequence of the winter decrease, the relative fraction of TCs occurring during the austral summer increases, especially during the months of February, March, and April (57% of TCs in SIO-F vs 51% in SIO-P). Further elements about this seasonal redistribution of TCs are discussed later.

b. Analysis of cyclogenesis indices

1) CGIs IN HIGH-RESOLUTION EXPERIMENTS

Previous studies have shown that CGIs can capture the geographical distribution of cyclone activity fairly well (e.g., Menkes et al. 2012). This is verified here over the SIO basin by comparing the aggregate index (average of CGIs, see section 3) computed on the ERA-5 data (Fig. 8a) with observed TC track densities (Figs. 5a,f). CGIs are indeed able to represent both the fraction of global cyclone activity that occurs within the SIO basin (12.5 out of 84 TCs yr^{-1} on average, similar to IBTrACS values) and its spatial distribution within the basin with a local maximum around 10°S, 75°E (spatial correlation of 0.73 between Figs. 5a and 8a when remapped onto the same 5° × 5° grid). The agreement between indices and actual track densities is less clear for the SIO-P experiment: CGIs suggest that cyclone activity should preferably occur within a latitudinally narrow area expanding from Madagascar to Indonesia similarly to ERA-5 (Fig. 8b) whereas TC tracks were detected more uniformly in the western part of the basin (Figs. 5d,i, spatial correlation of 0.54 between Figs. 5b and 8d). Possible reasons for this discrepancy can be that (i) the native resolution in SIO-P is nonuniform across the basin, (ii) CGIs were fitted on observations and reanalysis, so that coefficients used in their computation do not reflect the model characteristics, and (iii) the model (and the tracking algorithm) seem to have difficulties to simulate (detect) TCs at low latitudes, as reported in section 4a and Fig. 5.

CGIs fail to capture the 20% decrease in TC frequency between SIO-P and SIO-F that is observed in Figs. 5e,j (Fig. 8c). They instead indicate an unchanged cyclone activity on average over the SIO basin (difference of + 0.4 TCs yr^{-1}). This result is consistent with results of Chauvin et al. (2020) over the North Atlantic basin and also agrees with Camargo et al. (2014), who compared CGIs and actual TC tracks in high-resolution experiments from another model. Within the basin, the spatial pattern of changes in CGIs mostly consists in a poleward shift of the cyclone activity area, which is qualitatively consistent with changes in densities of tracks (Figs. 5e,j, spatial correlation of 0.25 between Figs. 5e and 8c) and with the poleward displacement of the location of lifetime maximum intensity (Fig. 6c). CGIs also support an increased cyclone activity north of Madagascar and in the Mozambique channel, as seen in the TC tracks. In other words, CGIs miss the overall decrease in TC frequency but seem to capture part of the changes in the regional distribution of TC tracks.

Further, breaking down changes in CGIs into dynamical and thermal components indicates that both contribute almost equally to the poleward shift of the cyclone activity area (Figs. 8d–f). They differ the most in the western part of the basin, especially north of the Mascarene Islands, where dynamical variables support a decrease in cyclone activity—consistent with the decrease in the number of TC tracks (Fig. 5j)—which is almost entirely compensated by the thermal contribution. One could interpret such a decrease in the dynamical component as less favorable conditions for cyclogenesis (i.e., decreased TC frequency), while the

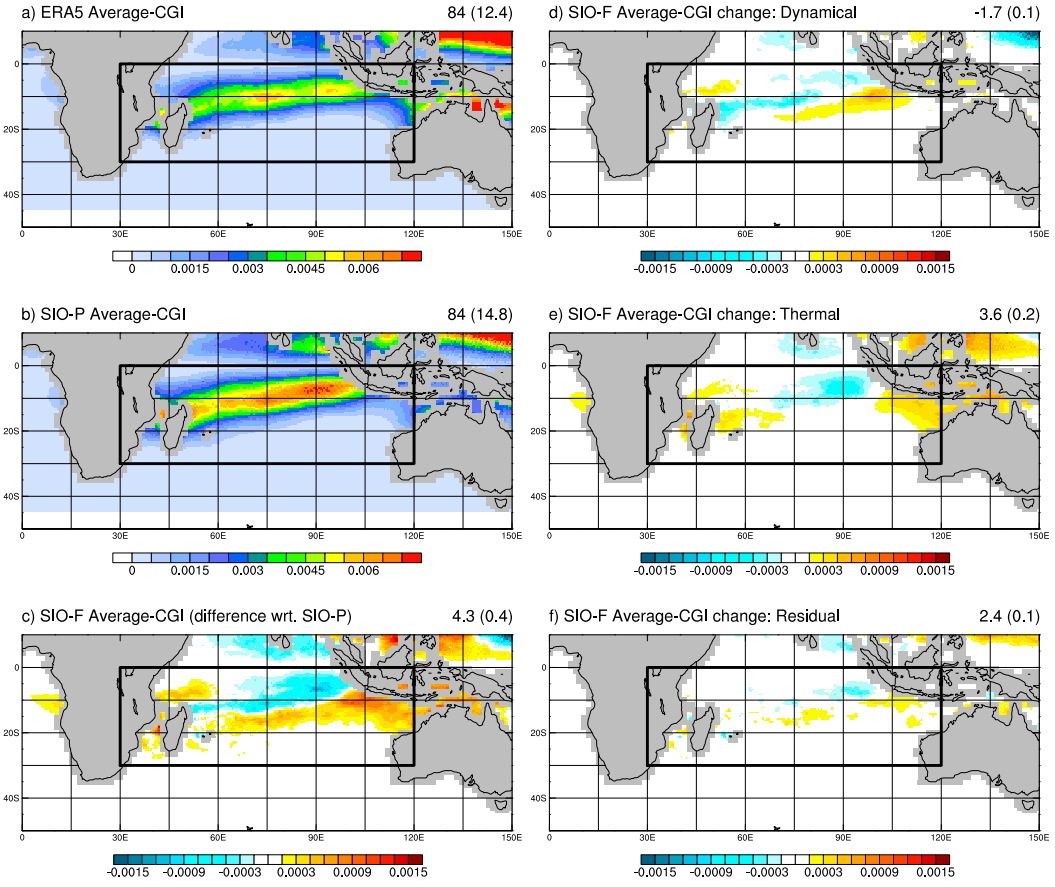

FIG. 8. (left) Annual mean of averaged CGIs (in number of TCs yr^{-1} and per $0.5° \times 0.5°$ grid box) for (a) ERA5, (b) SIO-P, and (c) SIO-F represented as a difference relative to (b). (right) Contributions of (d) dynamical components, (e) thermal components, and (f) residuals to (c). Sums over the globe and for the SIO domain (in parentheses) are indicated in the top-right corner of each panel.

increase in the thermal component could be indicative of more favorable conditions for intensification (i.e., increased TC intensity). However, this simple interpretation should be moderated by the fact that dynamical predictors can also be important for intensification (e.g., the vertical wind shear modulates the TC intensity), while thermal predictors can also be important for cyclogenesis (e.g., the midlevel relative humidity is relevant to spinning up the midlevel vortex in the early development). The CGI increase in the Mozambique channel solely arises from the thermal contribution, in line with a greater SST increase in this area compared to the rest of the basin (Fig. 1). The residual contribution is generally small but can be substantial especially in the eastern part of the basin.

Last, while results discussed above are based on the aggregate CGI, similar conclusions can be drawn from each index taken separately (not shown). In particular the spatial pattern of the SIO-F versus SIO-P difference (Fig. 8c) is common to all indices, albeit the spatial average over the domain differs (+0.4, +1.3, and −0.6 TCs per year for CYGP, GPI, and TIPP, respectively). As all the three indices share the same dynamical variables, there is little interindex dispersion in the dynamical contribution presented in Fig. 8d. Discrepancies in the thermal contribution, that is strongly positive for the GPI and slightly negative for the TIPP, therefore explain most of the differences between indices, suggesting that some thermal variables are more relevant than others to capture climate-related changes in cyclone activity.

2) CGIs IN CMIP5 MODELS

Here we assess whether changes in CGIs obtained in high-resolution CNRM-CM6-1 experiments are representative of changes in CGIs obtained in low-resolution multimodel CMIP5 projections. In the following we indicate CMIP5 ensemble-mean values together with the 10th and 90th percentiles of CMIP5 distribution between parentheses—as the ensemble contains 14

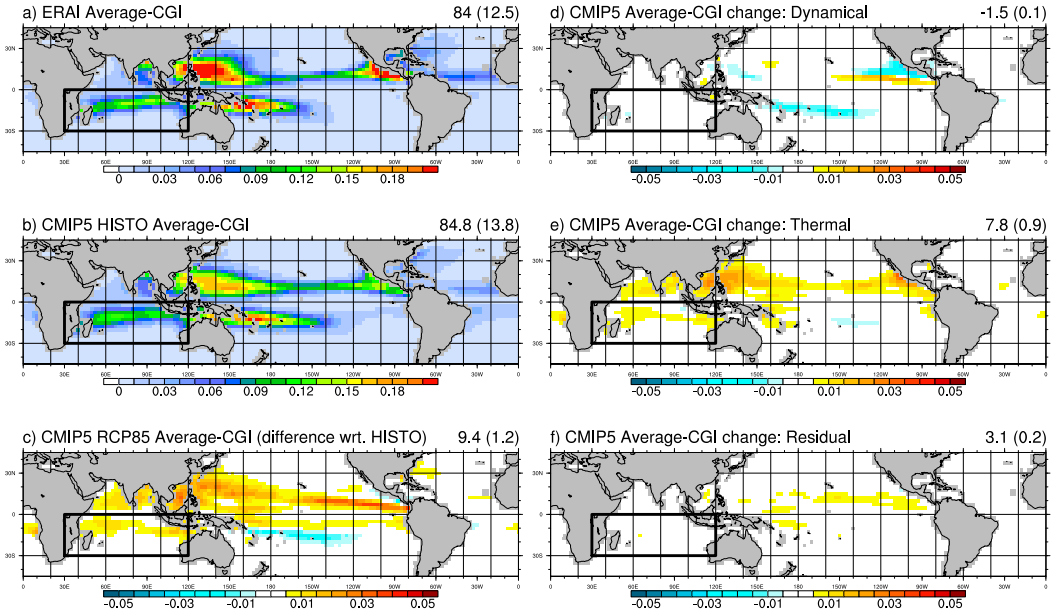

FIG. 9. (left) Annual mean of averaged CGIs (in number of TCs yr^{-1} and per 2.5° × 2.5° grid box) for (a) ERAI, (b) CMIP5 ensemble mean historical simulations over 1976–2005, and (c) CMIP5 ensemble-mean RCP8.5 simulations over 2070–99 represented as a difference relative to (b). (right) Contributions of (d) dynamical components, (e) thermal components, and (f) residuals to (c). Sums over the globe and for the SIO domain (in parentheses) are indicated in the top-right corner of each panel.

models, this range excludes the two lowest and two highest values.

First, comparing ERA-Interim (80-km resolution, interpolated onto a 2.5° grid, Fig. 9a) with ERA-5 (30-km resolution, interpolated onto a 0.5° grid, Fig. 8a) shows that the resolution has little effect on the computation of CGIs; this was expected since these indices are designed to account for large-scale conditions. Both reanalyses indeed result in a similar fraction of cyclone activity in the SIO (about 15% of the global activity) and a similar spatial pattern within the basin. CMIP5 models have been shown to represent the geographical climatology of several CGIs fairly well (Camargo 2013), which is here confirmed by our aggregate CGI (Fig. 9b), although the ensemble averaging tends to smooth hotspots of cyclone activity due to intermodel dispersion in the exact location of local maxima. On average, about 16% [14%–20%] of the global cyclone activity occurs in the SIO, which is consistent with reanalyses. [A more detailed analysis of individual CMIP5 model biases can be found in Camargo (2013) and is considered to be beyond the scope of this paper.] Importantly, we have verified that our SIO-P high-resolution experiment lies within the range of CMIP5 models in terms of representation of present-day climatology of CGIs (not shown).

In future RCP8.5 projections, CMIP5 models simulate an overall increase in CGIs, slightly less pronounced over the SIO (+9% [−8% to 20%]) than globally (+11% [−2% to 20%], Fig. 9c). Our results based on an aggregate CGI are consistent with the GPI analysis reported in Camargo (2013), although the GPI is the index that projects the strongest ensemble-mean increase: +16.3 (+2.8) TCs per year at global scale (in the SIO basin) versus +7.7 (+0.2) and +4.1 (+0.6) for the CYGP and the TIPP, respectively.

The global increase in CGIs projected by CMIP5 models (+11%, i.e., +9.4 TCs per year) arises from the thermal contribution (+7.8 TCs per year), while the dynamical component exhibits a small decrease (−1.5, Figs. 9d–f). The latter is robust across indices (−2, −1.2, and −1.3 for CYGP, GPI, and TIPP, respectively), while the former is the strongest for GPI (+14.7) and the lowest for TIPP (+3). This is consistent with CGIs applied to high-resolution experiments and supports the idea that changes in dynamical conditions could be related to changes in TC frequency (e.g., less favorable weather for cyclogenesis), while changes in thermal conditions could be related to changes in TC intensity (e.g., more available energy for intensification). This may be particularly the case for the GPI that includes the potential intensity introduced by Emanuel (1988) in its thermal component (Emanuel and Nolan 2004). Again, this interpretation should nevertheless be moderated because the relationship between dynamical versus thermal components and TC genesis versus intensification is not straightforward.

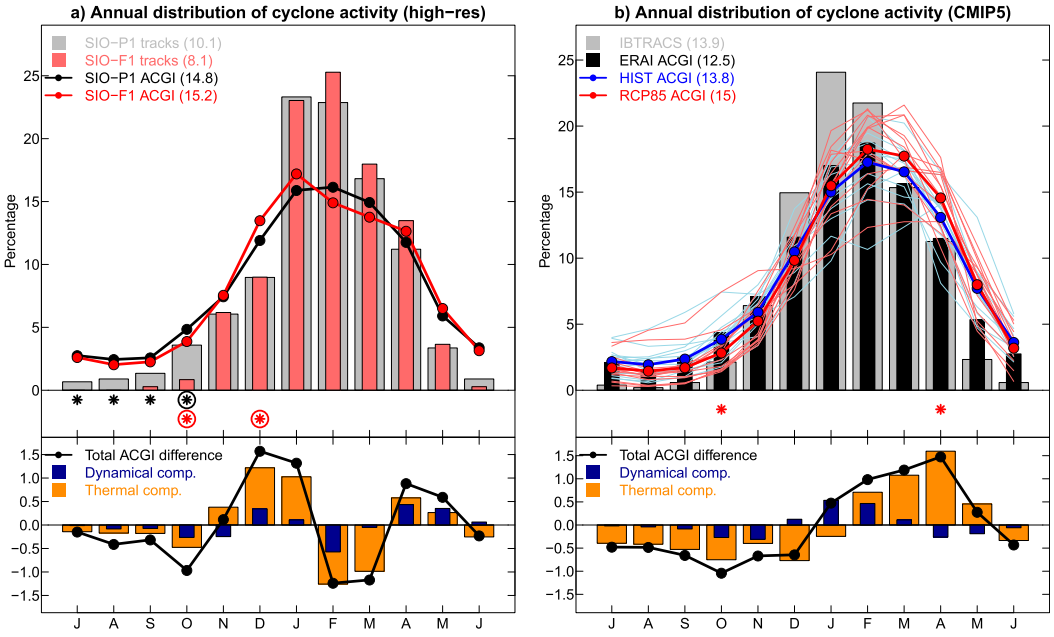

FIG. 10. (a) Annual distribution of SIO-P (gray bars) and SIO-F (red bars) TCs, and SIO-P (black line) and SIO-F (red line) aggregate CGI. Black (circled) asterisks indicate differences between bars that are significant at the 90% (95%) level; red (circled) asterisks indicate differences between lines that are significant at the 90% (95%) level. (b) Annual cycle of IBTrACS TCs (gray bars), and ERA-Interim (black bars), CMIP5 historical (blue lines), and RCP8.5 (red lines) averaged CGIs, with thick lines for ensemble means. Red (circled) asterisks indicate differences between ensemble means that are significant at the 90% (95%) level. All cycles are normalized and represented in percent per month. (bottom) Decomposition of the total aggregate CGI difference (black line) into dynamical (blue bars) and thermal (orange bars) components.

With a +0.4 TCs per year increase in the SIO (Fig. 8c), the SIO-F versus SIO-P difference is consistent with the range of CMIP5 projections. A fair comparison is, however, difficult since time periods used to evaluate changes differ. Interestingly, spatial patterns of CGI changes in the SIO are similar between high-resolution CNRM-CM6-1 experiments and the CNRM-CM5 experiment included in the CMIP5 ensemble (not shown). This is not completely surprising since SIO-P and SIO-F experiments use SST taken from this CNRM-CM5 simulation, but suggests that changes in large-scale environmental variables associated with cyclone activity are robust across the two versions of the atmospheric model and the two grid configurations. The poleward shift of cyclone activity suggested by CNRM-CM6-1 aggregate CGIs is, however, not representative of the CMIP5 ensemble that rather projects a reinforcement of cyclone activity close to the equator (Fig. 9c). This highlights that changes in the geographical distribution of cyclone activity captured by CGIs can be model dependent (e.g., Camargo 2013).

3) ANALYSIS OF CGIS' ANNUAL CYCLE

Globally, CGIs have been shown to represent the annual cycle of TC occurrence fairly well, although with a weaker seasonal amplitude (Menkes et al. 2012). This is confirmed here by our high-resolution exeriments: in the SIO-P experiment, 90% of the TC tracks occur from November to May while the aggregate CGI would indicate 78% (Fig. 10a). As discussed above (Fig. 7), we find a dramatic decrease in TC frequency during the austral winter in the SIO-F experiment, which translates into a significant decrease in the relative TC occurrence from June to October, counterbalanced by an increase—albeit not significant—from February to April. This redistribution is partly explained by CGIs, which also support a relative decrease of cyclone activity in winter (significant in October) and a relative increase in summer (significant in December). The fact that relative changes disagree between TC tracks and CGIs in February and March could be due to sampling uncertainty since they are not statistically significant.

Annual cycles of both TC occurrence and CGIs simulated by the SIO-P experiment are consistent with IBTrACS and ERA-Interim, respectively (Fig. 10b). In particular, 94% of IBTrACS TCs occur from November to May while the ERA-Interim aggregate CGI would indicate 82%. CMIP5 historical simulations are generally consistent with ERA-Interim in that aspect,

although they tend to underestimate (overestimate) the proportion of cyclone activity in early (late) summer: 49% (41%) from November to February (March to June) on average over the ensemble versus 54% (35%) in ERA-Interim. Projected changes in the RCP8.5 simulations are indicative of relative decrease of cyclone activity from June to December (significant in October) counterbalanced by a relative increase from January to May (significant in April). Such a seasonal redistribution of cyclone activity is fully consistent with results from our high-resolution experiments, suggesting that this feature of TC changes could be robust across models. Last, both dynamical and thermal components contribute to reshaping the annual cycle of CGIs, although monthly contributions differ: for instance, in CMIP5, the CGI relative increase in summer is mostly explained by the dynamical component in January, by the thermal component in March and April, and by both in February.

5. Discussion

In this paper we have tried to assess projected changes in the SIO cyclone activity from two complementary approaches: (i) high-resolution experiments with our in-home model (CNRM-CM6-1) that simulates realistic TCs and allows for a statistical analysis of TC characteristics and (ii) low-resolution multimodel climate projections in which cyclone activity can only be estimated from empirical indices built on large-scale environmental variables. Although we have shown that robust results emerge, both approaches used in this study suffer from clear limitations.

First, our high-resolution experiments are performed in an atmosphere-only framework (i.e., with prescribed SST), whereas the atmosphere strongly interacts with the near-surface ocean during TCs. Daloz et al. (2012) have shown that the ocean–atmosphere coupling can modify the simulation of TCs by the rotated-stretched configuration of the CNRM-CM model, the impact being sensitive to the coupling frequency. However, in their review paper, Walsh et al. (2016) assess that atmosphere–ocean coupling only has a limited effect on climate change experiments. In addition, using an atmosphere-only framework allows us to correct for potential biases in SST (as done in our experimental design).

Second, results obtained with the rotated-stretched configuration might be sensitive to the arbitrary choice of the grid pole location (Daloz et al. 2012). In the present study, the focus has been intentionally made on the western part of the SIO, in order to better assess potential changes in TCs over the area enclosing Mozambique, Madagascar, and the Mascarene Islands [i.e., the region under the responsibility of Météo-France (local RSMC)]. In exchange, the resolution was not dramatically increased at the other side of the SIO (Australian shore) compared to the uniform T359 grid. We are nevertheless confident (from our expertise with the rotated-stretched configuration) that a small displacement of the grid pole would not have altered the results significantly. The fact that the uniform T359 experiment (50 km) simulates reasonable TCs gives us additional confidence that results of rotated-stretched experiments are robust across the whole SIO basin. Last, our results share some similarities with Chauvin et al. (2020), which suggests that the main conclusions could be robust among oceanic basins, although a more systematic analysis would be needed.

A third limitation of our experimental protocol is that it only includes one member per experiment, which could raise questions about our ability to disentangle climate change signal from the noise of internal variability. More ensemble members would probably have smoothed the changes in track densities presented in Fig. 5; we were nevertheless able to detect a few statistically significant changes at the basinwide scale, such as the decrease in the overall number of TCs or the reduction in the duration of the cyclone season. In their analysis of the North Atlantic basin, Chauvin et al. (2020) performed five members per experiment and concluded that although this provides robustness in results obtained at regional scale, one member of 50 years is sufficient for the large-scale signal to emerge.

A follow-up question is the sensitivity of our results to the unique model used to perform high-resolution experiments (CNRM-CM6-1). Here we have shown that (i) our results are quantitatively similar to other high-resolution modeling studies (e.g., Murakami et al. 2012) and that (ii) large-scale environmental changes simulated by CNRM-CM6-1 lie in the range of CMIP5 uncertainties. However, the issue of model dependency will not be properly tackled until multimodel ensembles of high-resolution climate projections exist, and the upcoming HighResMIP exercise (Haarsma et al. 2016) can be considered as a promising first step to that regard.

Last, statistical tools used to analyze both high-resolution experiments (TC tracking algorithm) and multiple low-resolution model datasets (computation of CGIs) can be questioned. The TC tracking algorithm uses several arbitrary thresholds (winds, vorticity, temperature) that clearly affect the number of systems detected; however, we have verified that our main findings remain unchanged when using slightly different thresholds (not shown). The computation of CGIs is also problematic as the choice of the predictors (environmental variables) and the fit of their coefficients are likely to be model

sensitive; using 3 indices and 14 models was a way to take this source of uncertainty into account, and building more sophisticated and possibly model-dependent CGIs is left for future work.

6. Conclusions

The aim of this study was to assess projected changes in the SIO tropical cyclone (TC) activity from both high-resolution CNRM-CM6-1 dedicated experiments and CMIP5 multimodel climate projections. Our main findings can be summarized as follows:

- the uniform T359 (50 km) configuration of the CNRM-CM6-1 model is able to simulate realistic TCs in terms of frequency and pressure–wind relationship, although with a weaker intensity than observed. The rotated-stretched configuration improves the realism of simulated TCs (especially in terms of intensity) over the area of interest.
- Rotated-stretched high-resolution experiments project a 20% decrease in the SIO TC frequency between 1965–2014 and 2045–94 in the RCP8.5 scenario. In the meantime, they indicate an increase in the maximum lifetime intensity, and a slight poleward extension of the TC tracks. As a consequence, the frequency of the strongest TCs is projected to remain nearly constant.
- Rotated-stretched high-resolution experiments project a substantial reduction of the cyclone season duration; in particular the first TC of the season is projected to occur 1 month later on average (mid-December vs mid-November). Although the raw number of TCs is projected to decrease for all individual months, cyclone activity is redistributed within the season, with a smaller (greater) relative proportion of cyclones occurring in early (late) summer. This result may be important for Regional Specialized Meteorological Centres and local administrations in charge of TC monitoring and alertness.
- Cyclogenesis indices (CGIs) applied to high-resolution experiments fail to capture the projected decrease in overall TC frequency. However, they are able to partially represent changes in the spatiotemporal distribution of cyclone activity, such as the poleward shift and the seasonal redistribution. This may not be surprising as CGIs are designed to represent not the total number of TCs but their spatiotemporal distribution.
- Changes in CGIs obtained from CNRM-CM6-1 lie in the range of CMIP5 projections. In particular the seasonal redistribution of cyclone activity is consistent across models.

Future work will involve further understanding of the decreasing TC frequency in CNRM-CM6–1 experiments: whether this results from less frequent initiations of small-scale vortices or from less favorable conditions to intensification into TCs will be particularly scrutinized in the light of the work of Duvel (2015). Besides, the computation of CGIs in high-resolution experiments can be viewed as a first step into the physical understanding of changes in cyclone activity, and future analyses will further explore how they relate to changes in large-scale environmental features such as the Indian monsoon, the Madden–Julian oscillation, and/or the Hadley–Walker circulation. Impact studies may also be conducted to assess consequences of the projected changes in cyclone activity on associated phenomena such as rainfall or storm surges. Expanding the analysis to the new generation of climate models (CMIP6)—especially those with sufficiently high resolutions to simulate realistic TCs—will also be naturally considered for future work.

Finally, a promising prospective of this study is to pursue the efforts to reconcile results on TCs derived from high-resolution experiments with CGIs computed on low-resolution climate projections. In this paper we have shown that although CGIs miss the overall decrease in the number of TCs, they partially capture changes in their spatiotemporal distribution. Further, we have shown that the future increase in CGIs is mostly driven by their thermal component, while their dynamical component slightly decreases. The fact that these indices are empirically fitted on present-day cyclone activity features might give too much weight to the thermal component in a climate change context. Future research may therefore focus on the development of cyclogenesis indices that remain relevant for assessing climate change, taking advantage of high-resolution climate projections distributed within CMIP6 and possibly using more comprehensive statistical learning techniques.

Acknowledgments. This work has been partly supported by the ReNovRisk-C3 project within the Indian Ocean INTERREG-V Programme 2014–20. J.C. thanks all people at LACy and Météo-France La Réunion for their welcome and fruitful discussions, and Rémy Lee-Ah-Siem for technical support.

REFERENCES

Atkinson, G., and C. Holliday, 1977: Tropical cyclone minimum sea level pressure/maximum sustained wind relationship for the western North Pacific. *Mon. Wea. Rev.*, **105**, 421–427, https://doi.org/10.1175/1520-0493(1977)105<0421:TCMSLP>2.0.CO;2.

Camargo, S., 2013: Global and regional aspects of tropical cyclone activity in the CMIP5 models. *J. Climate*, **26**, 9880–9902, https://doi.org/10.1175/JCLI-D-12-00549.1.

——, M. Tippett, A. Sobel, G. Vecchi, and M. Zhao, 2014: Testing the performance of tropical cyclone genesis indices in future climates using the HiRAM model. *J. Climate*, **27**, 9171–9196, https://doi.org/10.1175/JCLI-D-13-00505.1.

Chauvin, F., J.-F. Royer, and M. Déqué, 2006: Response of hurricane-type vortices to global warming as simulated by ARPEGE-Climat at high resolution. *Climate Dyn.*, **27**, 377–399, https://doi.org/10.1007/s00382-006-0135-7.

——, R. Pilon, P. Palany, and A. BelMadani, 2020: Future changes in Atlantic hurricanes with the rotated-stretched ARPEGE-Climat at very high resolution. *Climate Dyn.*, **54**, 947–972, https://doi.org/10.1007/s00382-019-05040-4.

Daloz, A. S., F. Chauvin, and F. Roux, 2012: Impact of the configuration of stretching and ocean–atmosphere coupling on tropical cyclone activity in the variable-resolution GCM ARPEGE. *Climate Dyn.*, **39**, 2343–2359, https://doi.org/10.1007/s00382-012-1561-3.

Dee, D., and Coauthors, 2011: The ERA-Interim reanalysis: Configuration and performance of the data assimilation system. *Quart. J. Roy. Meteor. Soc.*, **137**, 553–597, https://doi.org/10.1002/qj.828.

Duvel, J.-P., 2015: Initiation and intensification of tropical depressions over the southern Indian Ocean: Influence of the MJO. *Mon. Wea. Rev.*, **143**, 2170–2191, https://doi.org/10.1175/MWR-D-14-00318.1.

Emanuel, K., 1988: The maximum intensity of hurricanes. *J. Atmos. Sci.*, **45**, 1143–1155, https://doi.org/10.1175/1520-0469(1988)045<1143:TMIOH>2.0.CO;2.

——, and D. Nolan, 2004: Tropical cyclone activity and the global climate system. Preprints, *26th Conf. on Hurricanes and Tropical Meteorology*, Miami, FL, Amer. Meteor. Soc., 240–241.

Gray, W. M., 1975: Tropical cyclone genesis. Atmospheric Science Paper 234, Colorado State University, 121 pp.

Haarsma, R., and Coauthors, 2016: High Resolution Model Intercomparison Project (HighResMIP v1.0) for CMIP6. *Geosci. Model Dev.*, **9**, 4185–4208, https://doi.org/10.5194/gmd-9-4185-2016.

Held, I., and M. Zhao, 2011: The response of tropical cyclone statistics to an increase in CO_2 with fixed sea surface temperatures. *J. Climate*, **24**, 5353–5364, https://doi.org/10.1175/JCLI-D-11-00050.1.

Hersbach, H., and Coauthors, 2018: Operational global reanalysis: Progress, future directions and synergies with NWP. ERA Rep. Series 27, 65 pp, https://doi.org/10.21957/tkic6g3wm.

Holland, G., and C. Bruyère, 2014: Recent intense hurricane response to global climate change. *Climate Dyn.*, **42**, 617–627, https://doi.org/10.1007/s00382-013-1713-0.

Knapp, K., M. Kruk, D. Levinson, H. Diamond, and C. Neumann, 2010: The International Best Track Archive for Climate Stewardship (IBTrACS). *Bull. Amer. Meteor. Soc.*, **91**, 363–376, https://doi.org/10.1175/2009BAMS2755.1.

Knutson, T., and Coauthors, 2010: Tropical cyclones and climate change. *Nat. Geosci.*, **3**, 157–163, https://doi.org/10.1038/ngeo779.

——, J. Sirutis, M. Zhao, R. Tuleya, M. Bender, G. Vecchi, G. Villarini, and D. Chavas, 2015: Global projections of intense tropical cyclone activity for the late twenty-first century from dynamical downscaling of CMIP5/RCP4.5 scenarios. *J. Climate*, **28**, 7203–7224, https://doi.org/10.1175/JCLI-D-15-0129.1.

Kossin, J., 2018: A global slowdown of tropical-cyclone translation speed. *Nature*, **558**, 104–107, https://doi.org/10.1038/s41586-018-0158-3.

——, T. Olander, and K. Knapp, 2013: Trend analysis with a new global record of tropical cyclone intensity. *J. Climate*, **26**, 9960–9976, https://doi.org/10.1175/JCLI-D-13-00262.1.

Kuleshov, Y., R. Fawcett, L. Qi, B. Trewin, D. Jones, J. McBride, and H. Ramsay, 2010: Trends in tropical cyclones in the South Indian Ocean and the South Pacific Ocean. *J. Geophys. Res.*, **115**, D01101, https://doi.org/10.1029/2009JD012372.

Malan, N., C. Reason, and B. Loveday, 2013: Variability in tropical cyclone heat potential over the Southwest Indian Ocean. *J. Geophys. Res. Oceans*, **118**, 6734–6746, https://doi.org/10.1002/2013JC008958.

Menkes, C., M. Lengaigne, P. Marchesiello, N. Jourdain, E. Vincent, J. Lefèvre, F. Chauvin, and J.-F. Royer, 2012: Comparison of tropical cyclogenesis indices on seasonal to interannual timescales. *Climate Dyn.*, **38**, 301–321, https://doi.org/10.1007/s00382-011-1126-x.

Murakami, H., and Coauthors, 2012: Future changes in tropical cyclone activity projected by the new high-resolution MRI-AGCM. *J. Climate*, **25**, 3237–3260, https://doi.org/10.1175/JCLI-D-11-00415.1.

Peng, M., B. Fu, T. Li, and D. Stevens, 2012: Developing versus nondeveloping disturbances for tropical cyclone formation. Part I: North Atlantic. *Mon. Wea. Rev.*, **140**, 1047–1066, https://doi.org/10.1175/2011MWR3617.1.

Rayner, N. A., D. Parker, E. Horton, C. Folland, L. Alexander, D. Rowell, E. Kent, and A. Kaplan, 2003: Global analyses of sea surface temperature, sea ice, and night marine air temperature since the late nineteenth century. *J. Geophys. Res.*, **108**, 4407, https://doi.org/10.1029/2002JD002670.

Royer, J.-F., and F. Chauvin, 2009: Response of tropical cyclogenesis to global warming in an IPCC AR4 scenario. *Hurricanes and Climate Change*, J. Elsner and T. Jagger, Eds., Springer, 213–234, https://doi.org/10.1007/978-0-387-09410-6_12.

——, ——, B. Timbal, P. Araspin, and D. Grimal, 1998: A GCM study of the impact of greenhouse gas increase on the frequency of occurrence of tropical cyclones. *Climatic Change*, **38**, 307–343, https://doi.org/10.1023/A:1005386312622.

Sugi, M., H. Murakami, and J. Yoshimura, 2012: On the mechanism of tropical cyclone frequency changes due to global warming. *J. Meteor. Soc. Japan*, **90A**, 397–408, https://doi.org/10.2151/JMSJ.2012-A24.

Taylor, K., R. Stouffer, and G. Meehl, 2011: An overview of CMIP5 and the experiment design. *Bull. Amer. Meteor. Soc.*, **93**, 485–498, https://doi.org/10.1175/BAMS-D-11-00094.1.

Tippett, M., S. Camargo, and A. Sobel, 2011: A Poisson regression index for tropical cyclone genesis and the role of large-scale vorticity in genesis. *J. Climate*, **24**, 2335–2357, https://doi.org/10.1175/2010JCLI3811.1.

Voldoire, A., and Coauthors, 2013: The CNRM-CM5. 1 global climate model: Description and basic evaluation. *Climate Dyn.*, **40**, 2091–2121, https://doi.org/10.1007/s00382-011-1259-y.

——, and Coauthors, 2019: Evaluation of CMIP6 DECK experiments with CNRM-CM6-1. *J. Adv. Model. Earth Syst.*, **11**, 2177–2213, https://doi.org/10.1029/2019MS001683.

Walsh, K., and Coauthors, 2016: Tropical cyclones and climate change. *Wiley Interdiscip. Rev.: Climate Change*, **7**, 65–89, https://doi.org/10.1002/WCC.371.

Wehner, M., Prabhat, K. A. Reed, D. Stone, W. D. Collins, and J. Bacmeister, 2015: Resolution dependence of future tropical cyclone projections of CAM5.1 in the U.S. CLIVAR Hurricane working group idealized configurations. *J. Climate*, **28**, 3905–3925, https://doi.org/10.1175/JCLI-D-14-00311.1.

Woodruff, J., J. Irish, and S. Camargo, 2013: Coastal flooding by tropical cyclones and sea-level rise. *Nature*, **504**, 44–52, https://doi.org/10.1038/nature12855.

atmosphere

IMPACT FACTOR 3.110

CITESCORE 3.7

Article

Analysis of Climate Change Projections for Mozambique under the Representative Concentration Pathways

Alberto F. Mavume, Bionídio E. Banze, Odete A. Macie and António J. Queface

Special Issue
Tropical Cyclones in the Indian Ocean

Edited by
Prof. Dr. Olivier Bousquet

MDPI

https://doi.org/10.3390/atmos12050588

atmosphere

MDPI

Article

Analysis of Climate Change Projections for Mozambique under the Representative Concentration Pathways

Alberto F. Mavume [1,*], Bionídio E. Banze [1], Odete A. Macie [1] and António J. Queface [1,2]

[1] Departamento de Física, Faculdade de Ciências, Universidade Eduardo Mondlane, Avenida Julius Nyerere, 3453, Campus Universitário Principal, 257 Maputo, Mozambique; bionidio.banze@uem.mz (B.E.B.); odete.macie@uem.mz (O.A.M.); queface@uem.mz (A.J.Q.)

[2] Instituto Nacional de Gestão e Redução do Risco de Desastres, Programa de Gestão do Risco de Desastres e Resiliência, Rua Gare de Mercadorias, 690 Maputo, Mozambique

* Correspondence: amavume@uem.mz; Tel.: +258-21-493-377

Abstract: Despite having contributed the least to global warming and having the lowest emissions, the African region is the most vulnerable continent to climate change impacts. To reduce the levels of risk arising from climate change, it is mandatory to combine both mitigation and adaptation. While mitigation can reduce global warming, not all impacts can be avoided. Therefore, adaptation is essential to advance strategic interventions and reduce the impacts. As part of the international effort to cope with changing climate, a set of Coordinated Regional Downscaling Experiment (CORDEX) domains have been established worldwide. The CORDEX-Africa initiative has been developed to analyze downscaled regional climate data over the African domain for climate data analysis techniques and engage users of climate information in both sector-specific and region/space-based applications. This study takes outputs of high-resolution climate multi-models from the CORDEX-Africa initiative constructed at a spatial resolution of 50 km to assess climate change projections over Mozambique. Projected spatial and temporal changes (three 30-year time periods, the present (2011–2040), mid (2041–2070), and the end (2071–2100)) in temperature and precipitation under the Representative Concentration Pathways RCP2.6, RCP4.5, and RCP8.5 are analyzed and compared relative to the baseline period (1961–1990). Results show that there is a tendency toward an increase in annual temperature as we move toward the middle and end of the century, mainly for RCP4.5 and RCP8.5 scenarios. This is evident for the Gaza Province, north of the Tete Province, and parts of Niassa Province, where variations will be Tmax (0.92 to 4.73 °C), Tmin (1.12 to 4.85 °C), and Tmean (0.99 to 4.7 °C). In contrast, the coastal region will experience less variation (values < 0.5 °C to 3 °C). At the seasonal scale, the pattern of temperature change does not differ from that of the annual scale. The JJA and SON seasons present the largest variations in temperature compared with DJF and MAM seasons. The increase in temperature may reach 4.47 °C in DJF, 4.59 °C in MAM, 5.04 °C in JJA, and 5.25 °C in SON. Precipitation shows substantial spatial and temporal variations, both in annual and seasonal scales. The northern coastal zone region shows a reduction in precipitation, while the entire southern region, with the exception of the coastal part, shows an increase up to 40% and up to 50% in some parts of the central and northern regions, in future climates for all periods under the three reference scenarios. At the seasonal scale (DJF and MAM), the precipitation in much of Mozambique shows above average precipitation with an increase up to more than 40% under the three scenarios. In contrast, during the JJA season, the three scenarios show a decrease in precipitation. Notably, the interior part will have the largest decrease, reaching a variation of −60% over most of the Gaza, Tete, and Niassa Provinces.

Keywords: climate change; CORDEX-Africa; RCP; temperature; precipitation; Mozambique

Citation: Mavume, A.F.; Banze, B.E.; Macie, O.A.; Queface, A.J. Analysis of Climate Change Projections for Mozambique under the Representative Concentration Pathways. *Atmosphere* **2021**, *12*, 588. https://doi.org/10.3390/atmos12050588

Academic Editor: Mohammad Valipour

Received: 10 March 2021
Accepted: 24 April 2021
Published: 1 May 2021

1. Introduction

According to the International Panel on Climate Change (IPCC) Fifth Assessment Report (AR5), climate change warming is unequivocal, while it is extremely likely that

this is a result of anthropogenic activities. For instance, recent climate changes have had widespread impacts on human and natural systems worldwide [1].

Despite having contributed the least to global warming and having the lowest emissions, Africa faces exponential collateral damage, posing systemic risks to its economies, infrastructure investments, water and food systems, public health, agriculture, and livelihoods, threatening to undo its modest development gains and slip into higher levels of extreme poverty. This situation is aggravated by the interaction of 'multiple stresses', occurring at various levels and low adaptive capacity [2].

Mozambique is one of the African countries most exposed to climate-related risks, which is and will be exacerbated by climate change. Extreme dangerous and destructive events are remarkable and have been associated with the occurrence of disasters of major socio-economic impacts [3]. Its population was 13 million in 1990, it reached 27.9 million in 2017 and 29.5 million in 2018 with a growth rate of 2.9% per annum [4,5]. The Southern African sub-region (South Africa and Mozambique) is, after Northern Africa, the continent's most urbanized and is projected to reach a region-wide urban majority around the end of the current decade. South Africa reached an urban majority of 62% in 2011 with Mozambique projected to reach an urban majority by 2050 [6]. The urban population is low (33.4%) and the rural population is high (66.6%), but the wealth distribution is also uneven [7]. About 43% of the population resides within the coastal region of the country. Mozambique has been one of Africa's fastest growing economies throughout the past years, driven by investments related to the exploration of multiple natural resources. The Mozambique economy generally demonstrated growth in the 2010–2018 period; however the country's Gross Domestic Product (GDP) per capita has declined over the past decade, from 458 USD in 2007 to 443 USD in 2017, reflecting the country's population growth [7]. While the population growth numbers and investments are increasing, the vulnerability of the country is also increasing as coastal zones are exposed to a range of coastal hazards such as sea level rise, storm surges, and tropical cyclones. The 2018–2019 southwest Indian Ocean tropical cyclone season was remarkable, being the deadliest and costliest season ever recorded (≈1380 deaths and ≈USD 2.3 billion damage). Although the number of cyclones was exceptional across the region, most of the deaths and damage occurred as a result of Intense Tropical Cyclone IDAI. The situation become exacerbated on 25 April, with the appearance of Intense Tropical cyclone Kenneth, which was classified as the strongest cyclone to ever make landfall in Mozambique. This TC struck the Mozambique coast further north, resulting in considerable damage and socio-economic impacts (≈45 deaths and ≈USD 100 million damage) [8]. Weather associated with both cyclones affected the central and northern regions of Mozambique, including the neighboring countries of Zimbabwe and Malawi. These destructive cyclones resulted in severe humanitarian impacts, including hundreds of casualties and hundreds of thousands of displaced persons [8–10]. Therefore, vulnerability may increase, as the climate affects human lives, agriculture, water, health, infrastructure, and other aspects of daily life. Extreme weather events such those aforementioned among others including extreme precipitation and floods [11,12] and severe droughts [13], and high extreme temperatures and heat waves [14–16] are predicted to continue and pose significant social and economic pressures within several parts of Africa and elsewhere, while there is mounting evidence suggesting that the frequency and intensity of some events will change in the future due to climate change [17,18].

Post-2015, the Nationally Determined Contributions (NDCs) to the Paris Agreement (PA) have become the main instrument for guiding policy responses to climate change [10]. Three main actions emerged from PA 2015 showing the willingness of national governments to strengthen the global response to the threat of climate change: (i) to keep global temperature rise well below 2 °C above pre-industrial levels, and to pursue determined efforts to limit the temperature increase even further to 1.5 °C; (ii) to strengthen the ability of countries to adapt to climate change and develop low-carbon emission technology; and (iii) to make finance flows consistent with a pathway toward low-carbon emissions and climate-resilient development [19,20]. These two thresholds provided a strong signal for

the governments to take urgent decisions and actions to mitigate the ongoing and future climate change and for the scientific community to assess the various implications that could arise if warming overcomes 1.5–2 °C. A recent study [21] shows considerable global economic gains from complying with the Paris Climate Accord. With the implementation of the NDCs (formerly defined as Intended Nationally Determined Contributions, INDCs), aggregate global emission levels would be lower than in pre-INDC trajectories [21]. These efforts are greatly recognized; however, the translation of these commitments into plausible binding targets of greenhouse gas reductions at the national level is still slow. According to the UN Environment's 2019 Emissions Gap Report, the emissions will continue to increase, even if all national commitments under the Paris Agreement are implemented through the NDC and other regulatory mechanisms. The fact is the world is still on the course for around 3 °C of warming above pre-industrial levels [22,23]. Mozambique's NDC states clearly its adaptation mission to "reduce climate change vulnerability and improve the wellbeing of Mozambicans through the implementation of concrete measures for adaptation and climate risk reduction, promoting mitigation and low-carbon development, aiming at sustainable development, with the active participation of all stakeholders in the social, environmental and economic sectors". Mozambique has committed to reduce about 76.5 metric tons of carbon dioxide equivalent (76.5 MtCO2eq) from 2020 to 2030, which is conditional on the provision of support from the international community [24].

The two PA thresholds goals are essentially viewed as means to quantify if there is a significant reduction in regional and local climate risks and demonstrating benefits in limiting warming below 1.5 °C [25]. It is likely that negative effects of 0.5 °C increment can be seen in extreme events. For instance, estimates indicate that the chances of an extreme event at 0.5 °C warming is almost two times than that at 1.5 °C [26]. GDP loss estimates per year under global warming scenarios (2, 3, and 4 °C) are expected to be higher, and the relative damages from not complying with the 2 °C target for Southern Africa are particularly severe [21].

Temperature and precipitation are two key indicators that characterize the state of the climate and which have continuously affected living conditions in many geographical locations in Africa [10]. Thus, by changing the temperature and precipitation patterns, climate change becomes a major concern to the survival of the human being as it poses significant risks and impacts on the natural resources, environment, and surrounding assets.

Over Southern Africa, there is a positive sign of change for temperature, with temperature rising faster at 2 °C (1.5–2.5 °C) as compared to 1.5 °C (0.5–1.5 °C) of global warming. On the other hand, the region is projected to face robust precipitation decreases of about 10–20% and increases in the number of consecutive dry days and decrease in the number of consecutive wet days [20]. However, it is likely that some hotspots will face robust precipitation increases in some places. For instance, a projected increase in temperature is expected to influence the multiplication of pests, weeds, and several diseases that would lead to increased costs of crop production and failure in crop yields as well as reduction in food and water resources availability [20,27,28]. Some areas may become drier as a result temperature increases with increasing drought frequency and number of heatwaves [29–31]. Warming will also increase evaporation and transpiration rates that would result reductions in stream flow for hydroelectric power [32,33]. In addition, warming is also likely to increase outbreaks of waterborne diseases and diseases transmitted by rodents [34–38]. The projected increases in rainfall are likely to influence nutrient loss, removal of the top fertile layer of soil and saturation of soil, pests disease outbreaks, and infrastructure damage that would result in low crop yields and disruption of the food supply chain [1,20,36,39,40]. Changes in precipitation patterns are projected to cause severe flooding during the rainy season and severe drought during the dry season [41]. This scenario is likely to affect several business and economic sectors.

Within Southern Africa, Mozambique is one of the hotspots, as it is particularly vulnerable to climate change compounded by high levels of poverty and strong reliance on the rain-fed agriculture sector to drive its economy, employment opportunities, and

food security. The agriculture sector in Mozambique, being largely driven by smallholder farmers, is the primary livelihood basis for 80% of the population and contributes to the overall national economy with approximately 31.5% of the Gross Domestic Product (GDP) [42]. The majority of sectors, particularly agriculture, food security, and water resources, are strongly impacted by variations in temperature and precipitation. The impacts described above are currently happening and causing socio-economic impacts in Mozambique and are likely to be an additional challenge for the country to achieve various sustainable development goals and other national targets.

In this regard, monitoring and understanding the spatial and temporal characteristics of these two indicators (temperature and precipitation) under future climate, along with underlying impacts, at regional and local levels is crucial for strengthening science–policy dialogue and support decision making in the development of effective and science-based adaptation strategies at all levels of governance and sectors.

To perform this exercise, Global Circulation Models also or referred to as Global Climate Models (GCMs) have been used to assess the causes of past changes and for projecting temperature and precipitation changes in the future [43].

GCMs are complex computer models, as well as fundamental tools, designed to provide several important outputs, at a global scale, typically at a spatial scale of 200–330 km, for instance, which is not relevant for studies or applications at regional and local scales [41]. Climate change projections of high quality are performed by downscaling techniques and are often required in climate change impact assessments studies at regional and local scales [25,44,45]. They are also important for informing policy makers and the society on how science-based evidence can contribute to foster actionable mitigation and adaptation measures [46]. Therefore, downscaling of outputs from GCM is a required and important approach to overcome common limitations in the GCM such as coarse spatial resolution and bias [44,47]. The main approaches to downscale outputs from GCMs are (i) statistical downscaling [47,48] and (ii) dynamic downscaling [49]. These approaches result mainly not only from the spatial resolution but also from the more realistic or complete physics representation in Regional Climate Models (RCMs), which allow for obtaining detailed climate information about dynamic processes taking place in specific regions [50]. Dynamic downscaling, which relies on the boundary conditions from GCMs, is seen as the most appropriate approach for the better representation of these processes on climate variables [49]. However, these capabilities are not always are available for all, because they demand high computational requirements, particularly if they are of dynamic type [48]. For a comprehensive review about the types and main features of downscaling techniques, see [44]. On the other hand, in regions with low station coverage, weak data infrastructure, and limited modeling capabilities, people are often facing big challenges for conducting their assessments. Currently, there is a significant number of collaborative projects producing climate simulation from dynamic downscaling for model inter-comparisons and impact assessment. Today, thanks to the various collaborative projects around the world, climate simulations derived from dynamic downscaling for model inter-comparisons and impact assessments can be accessed [44]. Some of these projects involve the COordinated Regional Downscaling EXperiment (CORDEX) initiative, which produces dynamically downscaled climate simulations for all continents, including Africa. The CORDEX initiative is the most comprehensive effort ever made in coordinating regional climate projections throughout the world [46] and, for instance, an opening window for the scientific community to access these facilities to get the climate information and skills needed to conduct their own assessments. The CORDEX initiative was pioneered by the World Climate Research Programme (WCRP) to produce high-resolution climate datasets over different parts of the world, of which Africa was the first target region selected for the experiments [51].

Scientific research focusing on GCMs and downscaling techniques to produce climate change projections is receiving more attention in recent years, particularly from research groups of CORDEX community and affiliates. For instance, more than 60 research articles have been published under the CORDEX Africa initiative since 2012 and are publicly

available at the Climate Systems Analysis Group (CSAG), University of Cape Town, South Africa (http://www.csag.uct.ac.za/cordex-africa/cordex-africa-publications/, accessed on 12 March 2020). The majority of these studies are either focusing on the CORDEX Africa domain [25,52] or its subregions, namely, East Africa [47,53], West Africa [54,55], Southern Africa [31,56,57], Greater Horn of Africa [58], and the Congo Basin [59]. Some country-level studies have been conducted for Botswana [16], Tanzania [44,60], and Zimbabwe [61], among few others. In general, these publications address various applications providing a comprehensive range of a plausible future within the CORDEX Africa domain or under its subregions or countries. Regional analysis with RCMs in these studies highlighted the indisputable value of the downscaling approach compared to GCMs, as in most cases, it showed good performance in reproducing finer details among other features in both temperature and precipitation projections [25,52].

While some countries might have substantial progress in conducting studies and publishing such results, others have very limited published work, adding to the fact that either GCMs or RCMs downscaling techniques have not been or are poorly implemented and issues such as data infrastructure including the working environment need to be improved and expanded. These limited capabilities elements are common in several countries in Africa, particularly in Mozambique, which is the subject of the current research.

The research entitled "Impact of climate change on disaster risk in Mozambique", conducted by the National Institute for Disaster Risk Management and Reduction (INGD), former the National Institute for Disaster Management (INGC) was widely cited and became the first to apply climate change models on a regional scale to produce future climate change in Mozambique [62]. The study provided the country with an important view on the possible impacts of climate change on national investment and poverty reduction plans as well as the large sections of the coast characterized by human settlements and investments. The study [3] revealed that climate change and disaster risk go hand in hand because most of the impacts of climate change will be felt in the form of increased risk, spread, intensity, and frequency of natural disasters. Ref. [41] used the statistical downscaling of seven GCMs downscaled to each of the selected 39 station locations. All GCMs were used in the IPCC 4th Assessment Report and forced with SRES A2 emissions scenario (IPCC, 2000-which assumes that society will continue to use fossil fuels at a moderate growth rate, there will be less economic integration, and populations will continue to expand) for the 1960–2005, 2046–2065, and 2080–2100 periods. Ref. [41] found that both maximum and minimum temperatures are projected to increase by 1.5–3 °C in all seasons by all seven GCMs by the middle of the century (2046–2065). Exceptionally, the September-October-November (SON) season will experience the most increase-an increase of 2.5–3 °C. These increases in temperature are expected to be higher more toward inland and less at the coast, partially due to the moderate influence of the ocean. By the end of the century (2081–2100), temperature in the central region will increase by as much as 5–6 °C. Previous studies [29] found the same results, with most of the Southern African region projected to increase between 4 and 6 °C by the 2100s under the A2 SRES emissions scenario. The downscaled projections from seven GCMs [41] suggest an increase in precipitation in the December-May period by the middle of the century and end of this century, particularly in coastal areas considering significant spread between the models, which is indeed a challenge. However, increases in precipitation are likely to be greatest toward the end of the summer season, particularly in the north and coastal regions.

The objective of this work is to use the available CORDEX-Africa archives of regional climate modeled data and make a subset for the Mozambique domain in order to provide a comprehensive range of projected future changes. The study focuses on annual and seasonal temperature and precipitation changes and takes outputs of high-resolution climate ensemble from the CORDEX-Africa Initiative constructed at a spatial resolution of 50 km. It is notably part of the ReNovRisk-Cyclone research program, which aims to assess the impact of climate change on tropical cyclone activity and water resources in the southwest Indian Ocean basin, particularly in the Mozambique Channel region [63]. The

main focus of the analysis is to use the Representative Concentration Pathways scenarios (RCPs, [64,65]) to obtain climate change projections and explore future changes, risks, and impacts. The study assess the performance of model outputs in relation to historical data and the robustness of the projected changes of climate variables through the available simulations and ensembles. Furthermore, the study discusses the implications and usefulness of the projected changes for the various key country targets.

The results are presented and discussed in both regional and local context. Our findings could contribute to the climate adaptation and mitigation actions and NDC efforts in the country. In addition, while this study presents a different methodology, it is also an update of the previous scenario (SRES) applied in previous studies [3,29,41]. The development of RCP emerged from an IPCC request to the scientific community, as the existing scenarios (the so-called Special Emissions Scenarios-SRES) [66] needed to be updated and expanded in scope [64,65].

2. Data and Methods

2.1. Study Area and Climate

Mozambique, the focus domain of this study, is located in the southeastern part of the African Continent, between latitudes 10°27′ S and 26°57′ S and longitudes 30°12′ E and 40°51′ E (Figure 1), which favors the intertropical and subtropical climate conditions. The country has a total surface area of 799,380 km^2 (of which 98% is land and 2% form inland waters). The country holds a long coastline in the Indian Ocean, covering a total distance of about 2700 km and a continental shelf area of 104,300 km^2.

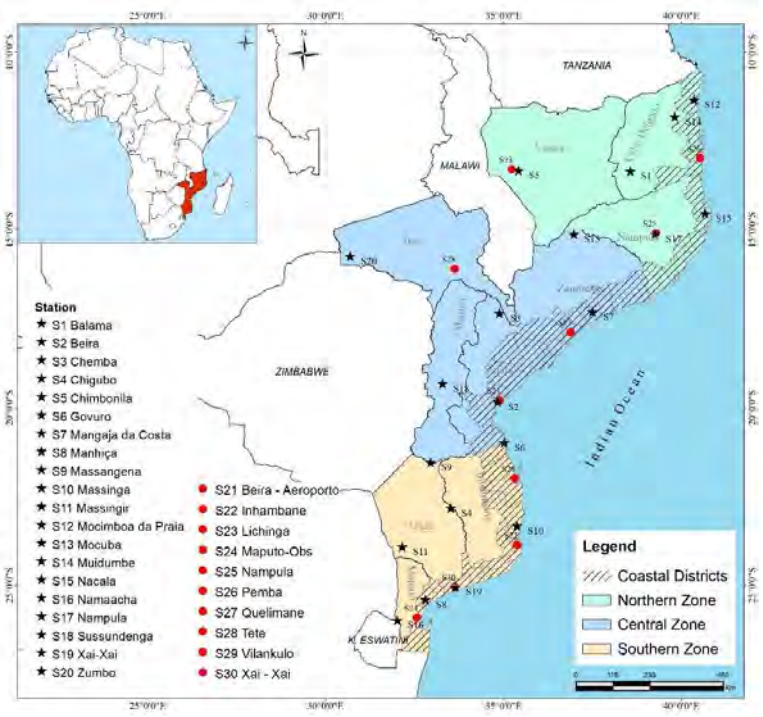

Figure 1. Map of the study area showing the administrative division of Mozambique, the different ground based meteorological stations, and the four sub-regions used in this study as highlighted from the map of the African continent.

Mozambique has a different climatic regime compared to most Southern African countries, given its coastal location, facing the warm Indian Ocean, the varying altitude, and its long latitudinal extension (between approximately 10° and 26° S). Thus, the northern part is dominated by a tropical rainy climate, while the central part is dominated by moderately humid climate modified by altitude. The central part is more prone to floods, tropical weather systems (e.g., tropical cyclones), and epidemics, followed by the north

and south. The southern part is more influenced by mid-latitude systems or by interactions with both. A tropical dry savannah climate is also a common feature in the southern part, which makes it more prone to drought than the center or north. For example, the central and northern regions in Mozambique receive between 400 and 600 mm more annual mean precipitation than the southern part [67]. Other areas in the center of the country and the entire coastal area receive amounts of precipitation ranging from 800 to 1000 mm. Furthermore, a significant number of dry spells is observed in the southern part, while in the northern part, rains are more regular [68].

Mozambique has two seasons: summer, which runs from October to March, and winter, which runs from April to September. The highest average maximum temperatures are found in the country's coastal zone, in the south of Tete province and in the western part of Gaza province [3]. Temperatures in Mozambique are highest during the summer and lowest during the winter. Average temperatures in Mozambique range from 25 to 30 °C (average maximum temperatures) in summer and between 15 and 21 °C (average minimum temperatures) in winter [3]. As for the average minimum temperatures, these have a decreasing pattern from the coast to the interior. The highest average minimum temperatures are found along the north coast, while the lowest are found in the province of Gaza. Extreme temperatures are common both in summer (above 40 °C) and winter (around 15 °C) in some areas.

In general, the precipitation producing systems in Mozambique comprise the Intertropical Convergence Zone (ZCIT), the El Niño-South Oscillation (ENSO), the Tropical Temperate Troughs (TTTs), the tropical cyclones formed in the southwestern Indian Ocean, the Indian Monsoon, the low-pressure systems on the continent, the frontal systems, the Indian Anticyclones, and Atlantic anticyclones. The country precipitation is heavily influenced by ENSO, a global oceanic temperature anomaly [69] that drives local interannual climate variability. The ENSO phenomenon is associated with severe dry conditions over central and southern Mozambique [70]. Conversely, the La Niña phase is associated with periods of heavy, extended precipitation, and it can result in floods. During the rainy season (November to March), precipitation variability in Mozambique is dominated by the ITCZ, a narrow transition belt, where the global northeast and southeast trades converge, inducing upward motion and precipitation [71]. Its influence is predominately felt in the north and center, whereas TTTs, oriented in a northwest–southeast direction, deliver substantial rain over large areas in the southern and central Mozambique and neighboring countries [12]. For instance, these authors hypothesize that a band of rain observed during a convective activity in mid-January 2013 could suggest a strong TTT feature with intense activity over southern Mozambique. TTTs are viewed and accepted as the main summer synoptic rain, producing a system over southern Africa [72] consisting of a combination between a lower-layer tropical perturbation and a mid-latitude trough in the upper atmosphere. Precipitation is the primary factor governing the development and persistence of drought [73]. Low levels of precipitation can have severe impact over Mozambique, which in many areas has a low resilience and limited capacity to mitigate drought effects. Tropical cyclones that generate within the Mozambique Channel (MC) or form and travel into the MC from the wider open waters east of Madagascar Island are occasionally able to make landfall into the African mainland, which is accompanied with heavy precipitation and other associated hazards [74–76]. There are other precipitation episodes of varying duration and intensity that are poorly documented, which are still a challenge for weather forecasters to predict given the short duration and surprising factor when they occur. For example, the interaction between sea breezes and urban heat islands seems to develop mesoscale convective systems that result in short-term heavy rains in some areas of the country. Synoptic-scale winds (e.g., sea breeze) are known to influence the heat island circulation, and their interaction has been studied and confirmed in other parts of the world [77]. Given the limited predicting skills when they occur, the earlier warning systems could not provide the necessary information in a timely and efficiently manner to the residents in order to avoid the consequences.

2.2. Data

2.2.1. Climate Data from Model Simulations Outputs

This study uses three different ensembles of regional climate change simulations outputs from the COordinated Regional Downscaling EXperiment (CORDEX-Africa): one ensemble of 4 simulations (out of which, 5 were not available) based on the representative concentration pathway (RCP) 2.6, one ensemble of 9 simulations based on RCP4.5, and one ensemble of 9 simulations based on RCP8.5. All data for the three ensembles, RCP2.6, RCP4.5 and RCP8.5, included in the analysis were available from the ESGF (Earth System Grid Federation) Swedish datanode (https://esg-dn1.nsc.liu.se/projects/esgf-liu/, accessed on 12 March 2020). The Regional Climate Model (RCA4) and the driving GCMs are presented in Table 1.

Table 1. List of driving Global Climate Model—GCMs (nine available for RCP4.5 and RCP8.5, and 4 available for RCP2.6 scenario) along with the RCA4 regional model.

	Project/Initiative	Driving GCMs (Historical)	Driving GCMs (Projections)	RCM	Period
1	CORDEX-Africa	CanESM2	CanESM2	RCA4	1951–2100
2	CORDEX-Africa	CNRM-CM5	CNRM-CM5	RCA4	1951–2100
3	CORDEX-Africa	CSIRO-MK3	CSIRO-MK3	RCA4	1951–2100
4	CORDEX-Africa	GFDL-ESM2M	GFDL-ESM2M	RCA4	1951–2100
5	CORDEX-Africa	HadGEM2-ES	HadGEM2-ES ([1])	RCA4	1951–2099
6	CORDEX-Africa	IPSL-CM5A-MR	IPSL-CM5A-MR	RCA4	1951–2100
7	CORDEX-Africa	MIROC5	MIROC5 ([1])	RCA4	1951–2100
8	CORDEX-Africa	MPI-ESM-LR	MPI-ESM-LR ([1])	RCA4	1951–2100
9	CORDEX-Africa	Nor-ESM1-M	Nor-ESM1-M ([1])	RCA4	1951–2100

Driving GCMs Institutes/Centers-1. Canadian Centre for Climate Modelling and Analysis; 2. Centre National de Recherches Météorologiques; 3. Commonwealth Scientific and Industrial Research Organization; 4. Geophysical Fluid Dynamic Laboratory; 5. Met Office Hadley Centre; 6. Institut Pierre Simon Laplace; 7. Tokyo Center for Climate System Research; 8. Max Planck Institute for Meteorology; 9. Bjerknes Centre for Climate Research. RCM Model Center: Swedish Meteorological and Hydrological Institute (SHMI). [1] Avaliable simulations for RCP2.6.

The data correspond to the 1951–2100 period and cover two of the most important meteorological variables in terms of direct impacts, the temperature and precipitation. The selected variables belong to the Phase I CORDEX simulations and have a spatial resolution of 0.44° (≈50 km). The data are retrieved following specific guiding instructions and steps (http://www.csag.uct.ac.za/cordex-africa/how-to-download-cordex-data-from-the-esgf/, accessed on 12 March 2020), which are provided at the ESGF-LiU data node. The regional climate model from which the data were derived is the latest fourth generation Rossby Centre Atmosphere regional climate model (RCA4) at the Swedish Meteorological and Hydrological Institute (SHMI) [78,79].

In practice, SHMI uses RCA4 to dynamically downscale all the GCMs over the Africa CORDEX domain [79]. The RCA4 model has been applied in previous studies in Africa [25] and other parts of the world [80]. Ref. [81] recognize that RCA4 has a number of improved modifications for specific physical parameterizations, which make it ideal and transferrable for applications in African regions. Some common concerns for almost the majority of RCMs in Africa include different convection schemes [82], including the phase of diurnal cycle of precipitation, among others. According to [81], this is an indication that higher resolution does not necessarily lead to a better performance of the RCMs. RCMs model outputs may still produce considerable systematic biases, and their direct use as input for impact assessment models may not be appropriate, since they might lead to inaccurate conclusions [83]. Biases are usually defined as long-term average deviations between simulations and observations [84]. Several bias correction methods have been developed to adjust meteorological variables from the RCMs ranging from simple scaling approaches to sophisticated distribution mapping [85–87]. The GCMs projections are forced by the Representative Concentration Pathways, which are hereafter referred to as RCPs [88]. The RCPs are prescribed greenhouse gas concentration pathways throughout the 21st

century, corresponding to different radiative forcing stabilization levels [64,65]. Three RCP were available for this study: (i) RCP2.6, the *lowest-level scenario* (most ambitious scenario with radical climate mitigation policies) which would slow global warming to 1.5 °C (the peak of the radiative forcing in the middle of the century of ≈3 W/m^2) followed by a decline; (ii) RCP4.5, *the mid-level scenario* with strong climate policy (e.g., the Paris Agreement) which would slow global warming to around 2 °C (or ≈4.5 W/m^2) by 2100 (RCP4.5), and (iii) RCP8.5, the *highest-level scenario* (business as usual scenario, without either countervailing action or climate policy), which could increase global warming up to 4 °C or 8.5 Wm^2 radiative forcing on the climate system by 2100.

2.2.2. Observed Data

The observed monthly precipitation, maximum temperature, and minimum temperature data from 27 stations were collected from the National Institute of Meteorology (INAM, https://www.inam.gov.mz/index.php/pt/, accessed on 12 March 2020) of Mozambique starting from 1961 to 2015. The historical observations were used for performance evaluation against the GCMs historical model outputs in each region of Mozambique.

Due to the inconsistencies in the observed station data, the evaluation was made only for the 1971–2000 period covering 10 stations (Table 2). After the evaluation was made, it was possible to read for each station the associated number of gaps for each variable (precipitation: Prec.; minimum temperature: Tmin.; and maximum temperature: Tmax.). Since the evaluated data showed fewer gaps compared to the initial station data, they are considered more reliable and suitable for the performance evaluation of quantile mapping against the GCMs historical model outputs.

Table 2. Observed stations (10) from the National Institute of Meteorology (INAM) used for the evaluation of model outputs and the related gaps to each data (%).

Station	Prec. Gaps (%)	Tmin Gaps (%)	Tmax Gaps (%)
Xai—Xai	4.11	5.83	7.5
Beira-Aeroporto	1.12	3.06	3.06
Pemba	1.41	5.62	5.62
Lichinga	6.51	1.67	1.67
Nampula	0.56	0.56	1.11
Quelimane	2.56	0.0	0.56
Tete	4.06	3.61	3.89
Maputo-Observatório	0.0	0.0	0.0
Inhambane	2.29	1.67	1.67
Vilanculos	6.21	4.72	5.0

2.3. Methods

2.3.1. Definition of Climate Periods, Seasons, and Subregions

Climate projections for temperature and precipitation are presented for different climate future periods and time scales. Following [53], the years 1961–1990 are defined as the baseline (reference) period or recent past, while the three 30-year period (time-slices), 2011–2040, 2041–2070, and 2071–2100, are representative for the *present*, *mid*, and *end* of the twenty-first century. The climate change projections for Mozambique are presented at annual scale in these periods.

The study also examined temperature and precipitation projections at a seasonal scale considering that large seasonal variations characterize most of Africa and Mozambique in particular [89]. In this context, climate analyses were performed including four seasons, summer (December-January-February (DJF)), late summer (May-June-July (MAM)), winter (June-July-August (JJA); and early summer (September-October-November (SON)) to explore changes in a seasonal context. Important circulation changes such as El Niño-Southern Oscillation (ENSO), Intertropical Convergence Zone (ITCZ), Mozambique Chanel Trough (MCT), monsoons, and Mascarene High, which alter the climate conditions in

Mozambique, seem to be the most dominant factors that control the seasonal changes. For example, in Southern Africa, the rainy season reaches its peak between December and February (DJF), when 80% of annual rainfall is recorded in the region, with some areas reaching 90% [90]. The influence of El-Niño is felt most in the southeastern part of Southern Africa, reaching a peak at the end of the summer i.e., between January and March (JFM) [91].

For spatial average analysis, the study area is divided in four sub-regions, namely: the coastal, northern, central, and southern regions (see [3]) based on the climatological features and vulnerability in the area (Figure 1 and Table 3).

Table 3. Sample of districts chosen according to vulnerability.

Region	District	Latitude	Longitude	Altitude (m)	Associated Vulnerability Event
Coastal	Govuro	−20.990	35.021	130	Drought/Floods/Cyclones
	Massinga	−23.329	35.382	116	Drought/Cyclones
	Mocimboa da Praia	−11.346	40.357	29	Drought/Cyclones
	Nacala	−14.541	40.672	133	Drought/Floods/Cyclones
	Mangaja da Costa	−17.309	37.508	103	Floods/Cyclones
	Beira	−19.846	34.841	5	Floods/Cyclones
	Xai-Xai	−25.053	33.644	45	Drought/Floods/Cyclones
	Manhiça	−25.401	32.810	37	Drought/Floods/Cyclones
Northern	Muidumbe	−11.823	39.821	504	Drought/Floods/Cyclones
	Balama	−13.348	38.572	591	Drought/Cyclones
	Nampula	−15.120	39.264	414	Floods
	Chimbonila	−13.331	35.423	550	Cyclones
Central	Zumbo	−11.823	30.447	504	Drought/Floods
	Chemba	−13.348	34.894	591	Drought/Floods/Cyclones
	Mocuba	−15.120	36.980	414	Floods
	Sussundenga	−13.331	33.293	550	Floods/Cyclones
Southern	Massangena	−21.545	32.952	120	Drought/Floods
	Chigubo	−22.830	33.523	210	Drought/Floods/Cyclones
	Massingir	−23.920	32.158	191	Drought/Floods
	Namaacha	−25.983	32.018	490	Drought/Floods

2.3.2. Evaluation of Historical CORDEX Model Simulations

The evaluation of historical simulations was made using Taylor diagrams. Taylor diagrams are defined as mathematical diagrams designed to graphically represent which of several approximate representations (or models) of a system, process, or phenomenon is most realistic, and how closely a pattern or a set of patterns matches observations [92,93]. These mathematical diagrams are constructed to assess the performance of model outputs in relation to historical data. Taylor diagrams in this context provide a graphical framework that allows variables from the set of models represented in Table 1 to be compared to our precipitation and temperature historical reference data provided by the INAM.

2.3.3. Calculation of Temporal and Spatial Variations in Climate Projections

The annual time series and spatial variations of temperature and precipitation have been calculated over the entire country as well as in four sub-regions. The multi-model average of simulations (or ensemble approach) is applied to reduce uncertainty associated with individual climate models based on the available Representative Concentration Pathways (RCP2.6, RCP4.5, and RCP8.5). For the temperature, the analysis will focus on the maximum of the change, since we are interested in knowing how much it will heat up until the end of the century. For precipitation, the analysis will focus on the 5th, 50th, and 95th percentiles. The 5th and 95th percentiles are used to indicate the range over which normal values are expected. The 50th percentile indicates the central value, giving the idea of the sign of most of the values.

2.3.4. Robustness of Projected CORDEX Model Simulations

The robustness of the climate projections is based on the combination of two tests, the test of agreement and the significance test, as described by [94]. The test of agreement assesses the robustness of the projections based on the comparison of the signal of each simulation in relation to the signal of the ensemble. The percentage of simulations whose sign of change agrees with the sign of the ensemble will define the level of robustness of the projections. In this study, it is considered that the projection is robust in terms of signal agreement, when over 66% of the simulations agree with the signal of the ensemble. For the significance test, the two-tailed Student t-test based on unequal variances between future and historical data, with a 95% confidence level was used. The significance test assesses the difference in distributions between two series, in this case, the 30 years of the simulated projections in relation to the historical 30 years. Similar to what was done in the test of agreement, the Student t-test was performed for each simulation in such a way that the change is considered statically significant if more than 66% of the simulations show a significant change. The analysis of the robustness of the climate projections is made for the 20 districts of the four regions shown in Table 3.

3. Results

3.1. Evaluation of Historical CORDEX Model Simulations

Taylor diagrams [92] were used to assess the performance of model outputs in relation to historical data in each region of Mozambique. The outputs of the nine models are represented by the letters M1, M2,..., M9, following the sequence shown in Table 1. Despite the evaluation of all model outputs, the analyses are focused on the average of the nine models, which is represented by "ALL".

Regarding temperature (Appendix A, Figure A1), it can be seen that all models show correlations above 0.7, in almost all stations, except in Pemba, where the correlations are above 0.5. The associated errors vary between 0.25 and 2 °C, with the standard deviation not exceeding 3 °C. The average of the models presents the best results in the evaluation, where their correlation reaches more than 0.9 in Beira, Inhambane, Lichinga, Quelimane, Vilanculos, and Xai-Xai.

In precipitation (Appendix A, Figure A2), different from temperature, the correlations are relatively lower. In some stations such as Beira, Inhambane, Maputo, Vilanculos, and Xai-Xai, the models show correlations below 0.5. Nampula and Lichinga present correlations that reach 0.75 and 0.77, respectively. The errors vary between 100 and 200 mm. Similar to what was observed in the temperature, the average of the models presents the best results also for precipitation. For the average of the models, only the stations of Inhambane, Maputo, Vilanculos, and Xai-Xai (all from the south) have correlations below 0.5. The rest of the stations show correlations above 0.6, with values reaching 0.79 in Nampula and 0.82 in Lichinga.

3.2. Calculation of Temporal Variations in Climate Projections

3.2.1. Temporal Variations in Mean Annual Temperature Projections

Figure 2a shows the time series of anomalies (in relation to the 1961-1990 reference period) of the historical and temperature projections for the three RCP scenarios (RCP2.6, RCP4.5, and RCP8.5), for the four regions (coastal, northern, central, and southern) chosen. It is evident that for the more optimistic scenario (RCP2.6), the temperature increase will start to stabilize around 2030, regardless of the region. In the RCP2.6 scenario, the temperature anomaly can reach up to 2 °C in all regions, except the coastal region. This suggests that the coastal region will experience less temperature variation. For the RCP4.5 scenario, the temperature starts to stabilize around 2050, and for this scenario, the temperature anomaly will not exceed 2 °C in the coastal region. In the remaining regions, anomalies associated with RCP4.5 reach 3 °C. The RCP8.5 scenario is the one with the most accentuated increase throughout the 21st century. Anomalies related to this scenario reach

values close to 6 °C in the southern region; on the other hand, in the coastal region, they do not reach 5 °C.

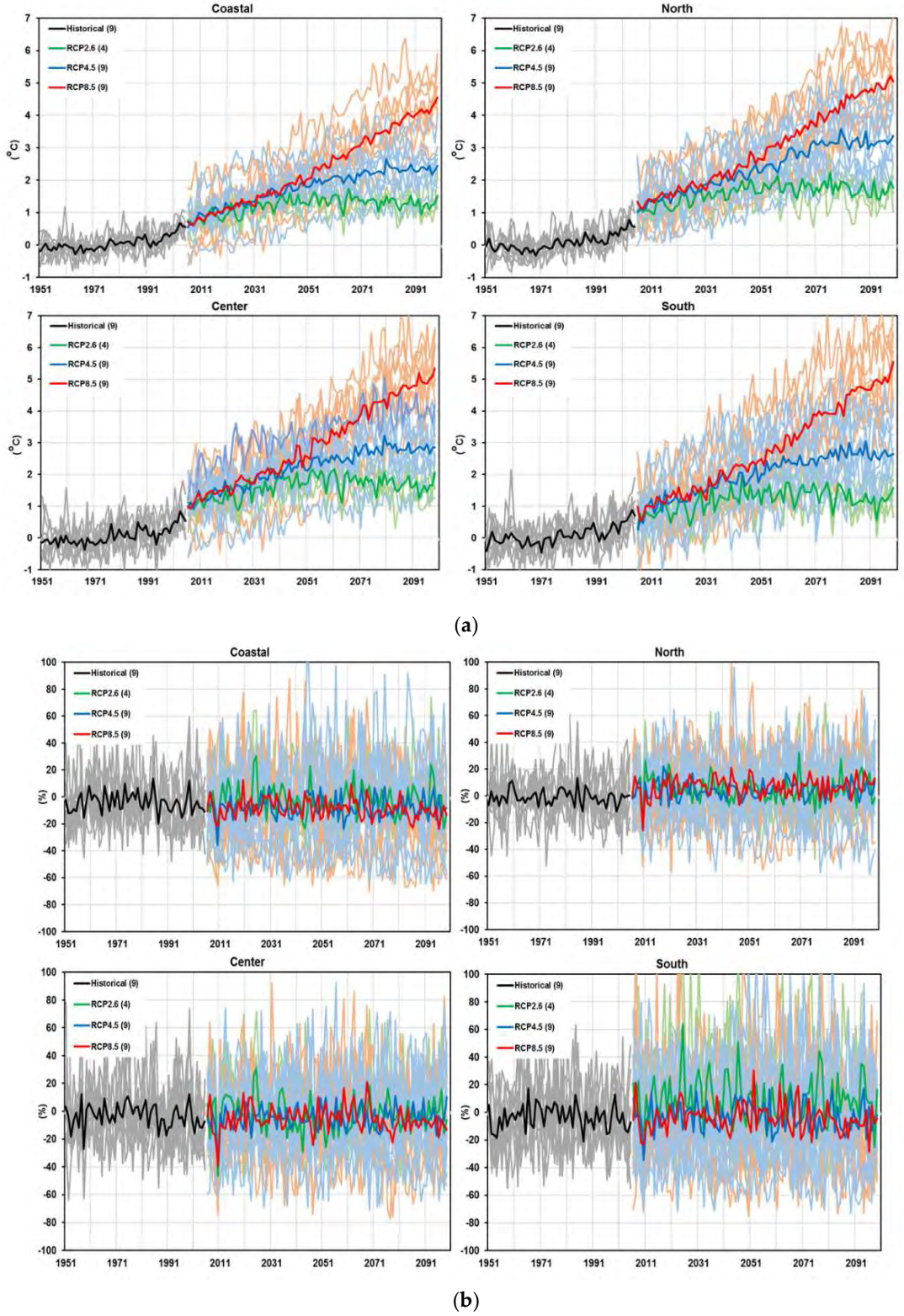

Figure 2. (**a**) Projected time-series of annual mean temperature anomalies with respect to the reference period 1961–1990, for the historical and three RCP simulations (RCP2.6, RCP4.5, and RCP8.5), for the four regions used in this study; (**b**) Projected time-series of annual precipitation anomalies with respect to the reference period 1961–1990, for the historical and three RCP simulations (RCP2.6, RCP4.5, and RCP8.5), for the four regions used in this study.

3.2.2. Temporal Variations of Annual Precipitation Projections

In the time series of precipitation anomalies (Figure 2b), it is clear that the southern region is the one with the greatest interannual variability. In general, all RCPs present a great annual variability, being that the northern region is the only one with an above average precipitation trend.

3.3. Changes in Mean Annual and Seasonal Temperature Projections over Mozambique

3.3.1. Projected Changes in Mean Annual Temperature

Projected changes for the three periods (2040s, 2070s, and 2100s) show that the average annual temperature (maximum, minimum, and average) will be higher than the average for the reference period (1961–1990), as it is presented in Figures 3–5. There is a tendency toward an increase in temperature as we move toward the middle and end of the century, mainly for the RCP4.5 and RCP8.5 scenarios, with the minimum temperature being the variable that will have the major variation. The coastal region of Mozambique will experience less variation, while the interior will experience greater changes in temperature. This result is consistent with that found by [3]. Some locations (hotspots) stand out for having the major variations regardless of the scenario and the period, such as the cases in the western part of the Gaza Province (near the border with Zimbabwe), the northern Tete Province, and the western part of the Niassa Province. The interior of the Gaza Province is one of the driest regions in Mozambique, while the Tete Province is predominantly the warmest.

Under the RCP2.6 scenario (Figures 3–5, left), during the 2040s, the extreme northeast of Mozambique (Cabo Delgado and Nampula Provinces) is the place that will present the smallest variations (values below 0.5 °C). According to Table 4, the change in maximum, minimum, and average temperatures may reach 0.92, 1.12, and 0.99 °C, respectively, being parts of Gaza and Inhambane (southern region), almost the entire province of Zambézia, and parts of the provinces of Tete, Sofala, and Manica (central region) and parts of the Niassa Province (northern region), the places where the major variation is observed. During the 2070s, the observed patterns do not portray significant differences, with the northernmost part of Mozambique showing variations below 0.5 °C. For this period, projected changes under the same scenario indicate that the maximum, minimum, and average temperature variation may reach 1.39, 1.56, and 1.45 °C, respectively (Table 4), with the provinces of the central region being those that will experience the major increase in the average annual maximum temperature. In the 2100s, in addition to the extreme northeast of Mozambique, the southwestern tip of Maputo Province also stands out as being the place where the change in the average annual maximum temperature does not exceed 0.5 °C. During this period, the temperature variation may reach 1.24 °C for the maximum, 1.4 °C for the minimum, and 1.23 °C for the average, with the central region being the place where the major change will occur.

Table 4. Maximum change in annual temperature for the 2040s (2011–2040), 2070s (2041–2070), and 2100s (2071–2100) with respect to the reference period (1961–1990) for the RCP2.6 scenario. The cells filled with the blue color have values below 2 °C (threshold defined by the Paris Agreement).

Period	Change in 2040s			Change in 2070s			Change in 2100s		
	Tmax	Tmin	Tmean	Tmax	Tmin	Tmean	Tmax	Tmin	Tmean
Annual	0.92	1.12	0.99	1.39	1.56	1.45	1.24	1.40	1.23
DJF	0.87	1.14	0.94	1.46	1.57	1.44	1.46	1.47	1.33
MAM	0.81	1.11	0.83	1.21	1.55	1.31	1.01	1.29	1.08
JJA	1.36	1.53	1.45	1.56	1.69	1.63	1.53	1.69	1.62
SON	1.41	1.33	1.40	1.83	1.78	1.84	1.72	1.67	1.71

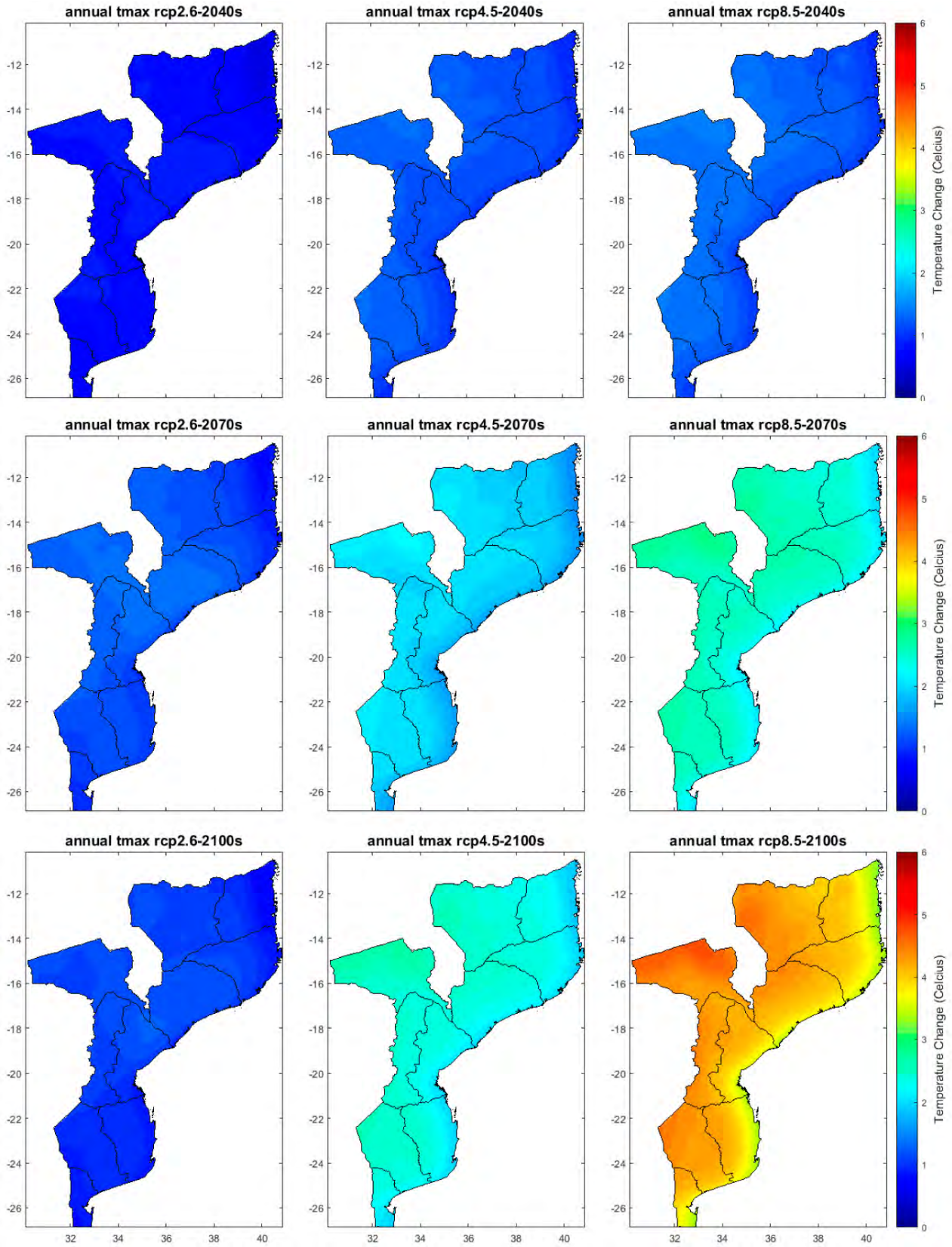

Figure 3. Projected changes of annual maximum temperature for the 2040s (2011–2040), 2070s (2041–2070), and 2100s (2071–2100) with respect to the reference period (1961–1990) for the three RCPs scenarios (RCP2.6, RCP4.5, and RCP8.5).

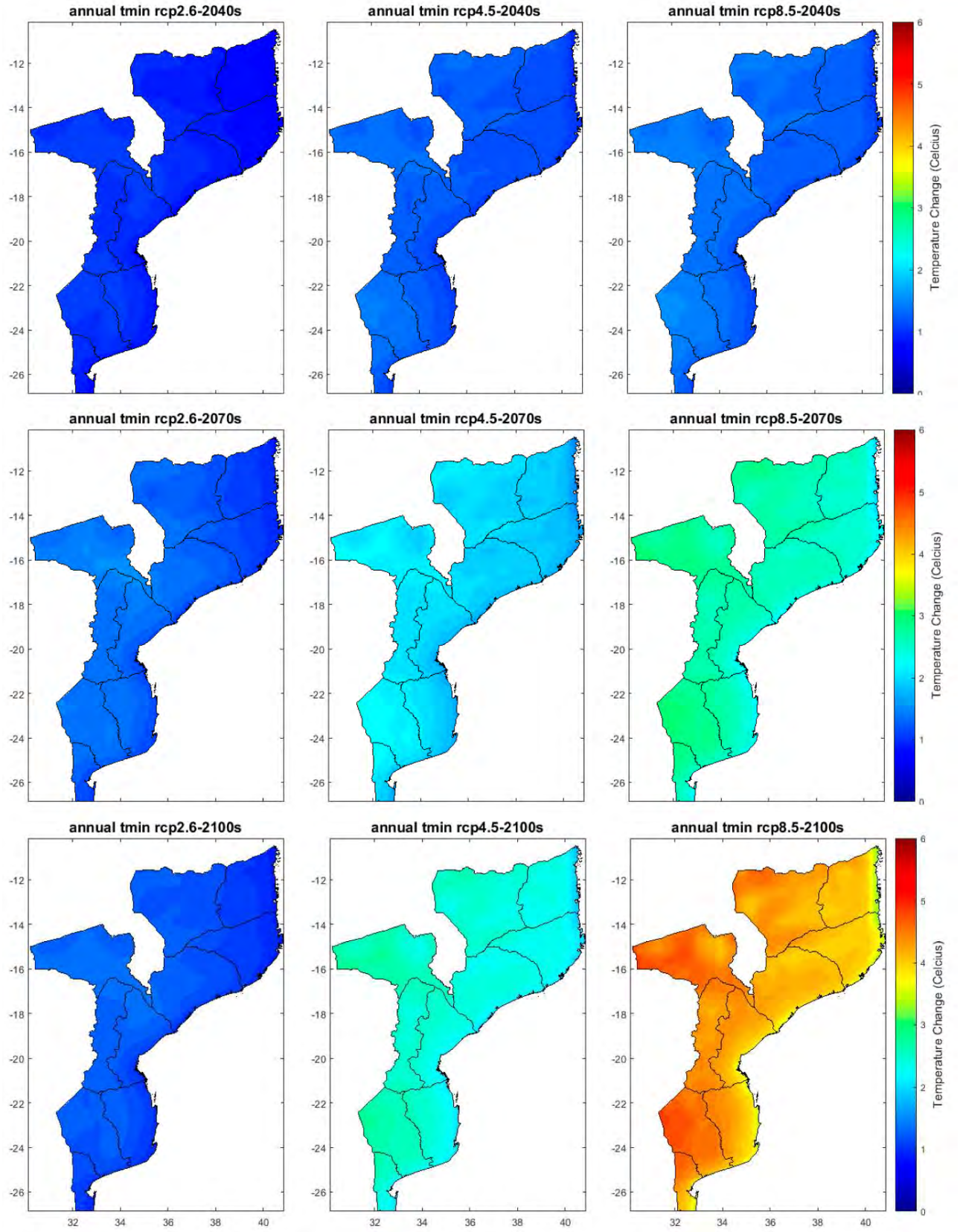

Figure 4. Projected changes of annual minimum temperature for the 2040s (2011–2040), 2070s (2041–2070), and 2100s (2071–2100) with respect to the reference period (1961–1990) for the three RCPs scenarios (RCP2.6, RCP4.5, and RCP8.5).

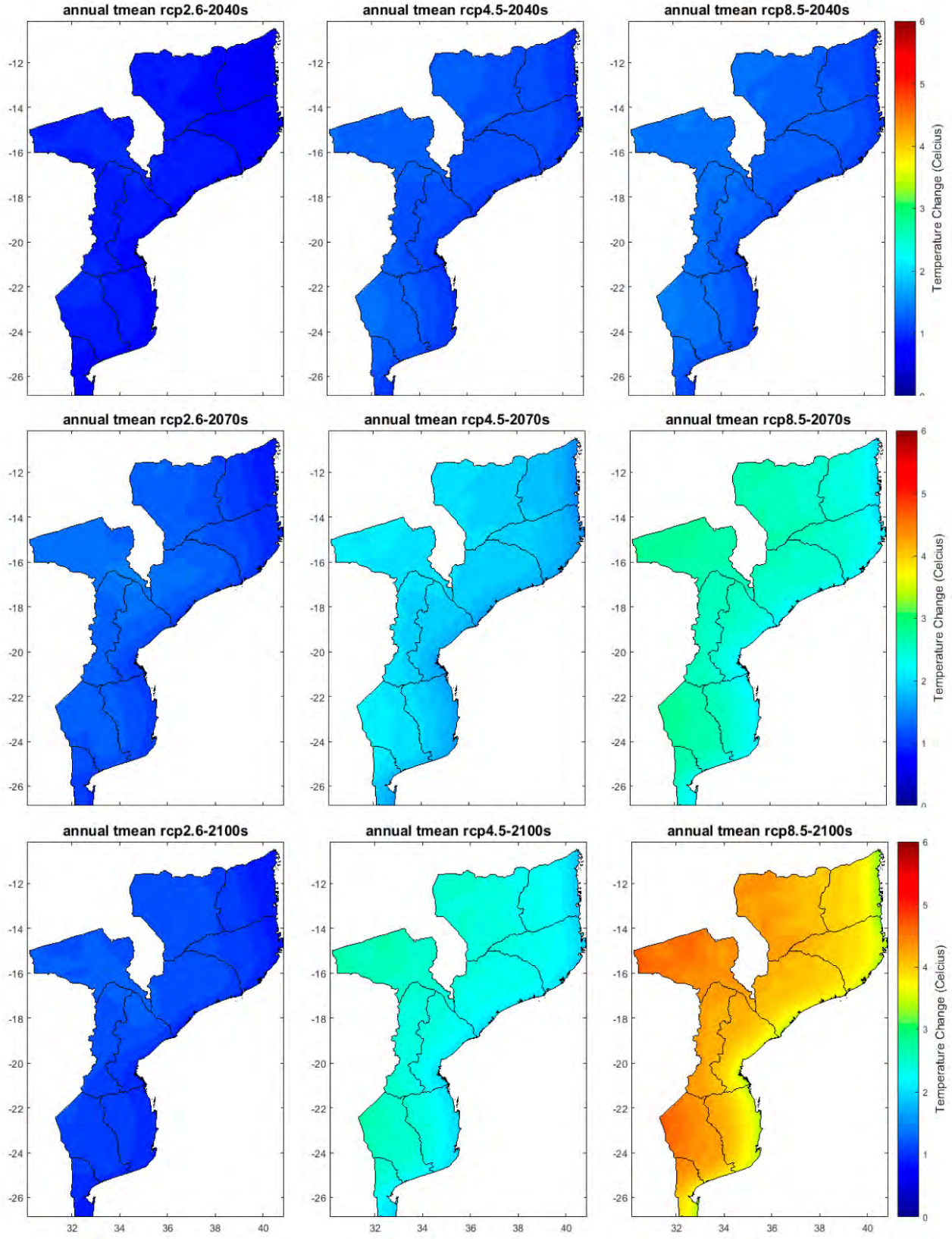

Figure 5. Projected changes of annual mean temperature for the 2040s (2011–2040), 2070s (2041–2070), and 2100s (2071–2100) with respect to the reference period (1961–1990) for the three RCPs scenarios (RCP2.6, RCP4.5, and RCP8.5).

The RCP4.5 scenario presents relatively higher temperature change values compared to RCP2.6 (Figures 3–5, middle). During the 2040s, the entire coastal region showed varia-

tions of less than 0.5 °C. The change in maximum, minimum, and average temperatures can reach 1.35, 1.46, and 1.39 °C (Table 5) with the interior of the Gaza Province, north of the Tete Province, and parts of the Niassa and Zambézia Provinces being the places that experience the major variations. In the 2070s, the temperature variation showed values that exceed 2 °C. The temperature change varies from just over 1 °C in the coastal region to around 2.28 °C in the interior areas. The northern part of the Tete Province is the place where the major variation is observed. During the 2100s, it is evident that for the RCP4.5 scenario, the temperature change is no more than 2 °C in the coastal region. In the interior of Mozambique, the temperature variation exceeds 2 °C, reaching 2.74 °C for the maximum temperature, 2.8 °C for the minimum temperature, and 2.71 °C for the average temperature.

Table 5. Maximum change in annual temperature for the 2040s (2011–2040), 2070s (2041–2070), and 2100s (2071–2100) with respect to the reference period (1961–1990) for the RCP4.5 scenario. The cells filled with the blue color have values below 2 °C (threshold defined by the Paris Agreement), and the cells with orange indicate temperature values between 2 and 4 °C.

Period	Change in 2040s			Change in 2070s			Change in 2100s		
	Tmax	Tmin	Tmean	Tmax	Tmin	Tmean	Tmax	Tmin	Tmean
Annual	1.35	1.46	1.39	2.20	2.28	2.19	2.74	2.80	2.71
DJF	1.47	1.38	1.40	2.19	2.15	2.12	2.57	2.53	2.51
MAM	1.20	1.39	1.27	2.05	2.18	2.01	2.74	2.89	2.69
JJA	1.49	1.55	1.47	2.34	2.39	2.23	2.89	2.91	2.74
SON	1.53	1.53	1.52	2.63	2.51	2.60	3.05	3.03	3.06

The projections under the RCP8.5 scenario (Figures 3–5, right) present a pattern consistent with that observed in both the RCP 2.6 and 4.5 scenarios. For the 2040s, the change is no more than 1 °C in the coastal region. The variation in maximum, minimum, and average temperatures can reach 1.49, 1.56, and 1.48 °C (Table 6), respectively, in which the interior of the Gaza Province, the north of the Tete Province, and parts of the Niassa Province are the places where the major changes are observed. In the 2070s, the coastal parts of the northern and southern regions will experience changes in temperature with values below 2 °C. In the interior areas, the change can reach 3 °C, with the interior of the Gaza Province, north of the Tete Province and parts of the Niassa Province being the most outstanding places. In the last 30 years of the century, projections under the RCP8.5 scenario show that the change in temperature may exceed 4 °C. In the coastal region, the temperature rise has values that reach 3 °C. The change in maximum, minimum, and average temperatures can reach 4.73, 4.85, and 4.7 °C, respectively, with the northern part of the Tete Province and west of the Niassa Province being the places that show the greatest change.

Table 6. Maximum change in annual temperature for the 2040s (2011–2040), 2070s (2041–2070), and 2100s (2071–2100) with respect to the reference period (1961–1990) for the RCP8.5 scenario. The cells filled with the blue color have values below 2 °C (threshold defined by the Paris Agreement), with orange indicating the cells with temperature values between 2 and 4 °C, and finally the red color representing the cells with values above 4 °C.

Period	Change in 2040s			Change in 2070s			Change in 2100s		
	Tmax	Tmin	Tmean	Tmax	Tmin	Tmean	Tmax	Tmin	Tmean
Annual	1.49	1.56	1.48	2.86	3.00	2.86	4.73	4.85	4.70
DJF	1.39	1.40	1.37	2.71	2.78	2.69	4.42	4.47	4.39
MAM	1.50	1.58	1.41	2.68	2.92	2.65	4.65	4.87	4.59
JJA	1.74	1.72	1.63	3.02	3.17	2.92	5.00	5.04	4.70
SON	1.66	1.64	1.64	3.28	3.32	3.28	5.25	5.20	5.20

3.3.2. Projected Changes in Mean Seasonal Temperature

At the seasonal time scale, the pattern of temperature change does not differ from the pattern found in the analysis of projections at the annual scale. The coastal zone has the smallest variations, and the interior has the largest variations. The JJA and SON seasons are the ones that present the largest variations in temperature, with the interior of the Gaza Province and parts of the Tete and Niassa Provinces being the places where the major changes are observed, mainly for the RCP 4.5 and 8.5 scenarios. At this point, due to the high number of variables to be analyzed, the focus will be on the average temperature.

The projections under the RCP2.6 scenario (Table 4) show that the temperature variations will not reach 2 °C, regardless of the period and the season. The spatial distribution of projected changes in temperature, under the RCP2.6 scenario during the DJF season (Figures A3–A5, left), shows that in addition to the coastal region, much of the southern region, including the interior of the Gaza Province, are the places where there will be the lowest variations (values below 0.5 °C). In this season, the variation in the average temperature may reach 0.94 °C in the 2040s, 1.44 °C in the 2070s, and 1.33 °C in the 2100s (Table 4). The northern Tete Province and parts of the Niassa and Zambézia Provinces are the places where the observed warming is largest. During the MAM season (Figures A6–A8, left), the pattern of temperature change is close to the pattern observed in DJF, with the exception of the minimum temperature, which is already beginning to show a significant increase in the interior of the Gaza Province, for the RCP 4.5 and 8.5 scenarios. The change in average temperature may reach 0.83 °C in the 2040s, 1.55 °C in the 2070s, and 1.08 °C in the 2100s (Table 4). The seasons of JJA (Figures A9–A11, left) and SON (Figures A12–A14, left) are the ones that will experience the major changes, with the minimum temperature being the variable that will present the major variation. This suggests that there is a tendency toward a decrease in thermal amplitude, with less cold winters. It is notable that during the 2040s, regardless of the time scale (annual or seasonal), the three temperature variables analyzed show an increase of no more than 1.5 °C except for the minimum temperature, which shows an increase that will reach 1.53 °C during the JJA season (Table 4). The major changes (values above 1 °C) are expected in the interior of the Gaza Province, south of the Manica Province, and north of the Tete Province (central and southern regions) and in parts of the Niassa Province (near the border with Malawi). During the 2070s, the temperature increased slightly compared to the 2040s. In this period (2070s), the change in the minimum temperature presents values above 1.5 °C, with the major change occurring in the SON season (1.78 °C). For the maximum and average temperature, only the JJA and SON seasons have changes above 1.5 °C. For these variables, the major change occurs during the SON season, with values reaching 1.83 °C for the maximum temperature and 1.84 °C for the average temperature. At the end of the century (2100s), projections under the RCP2.6 scenario show a temperature stabilization. The SON season is the one that presents the major changes, with values reaching 1.72, 1.67, and 1.71 °C, for the maximum, minimum, and average temperature, respectively.

For projections under the RCP4.5 scenario (Figures A3–A5, middle), during the DJF season, the coastal region remains the place where the smallest variations are observed. Unlike RCP2.6, for RCP4.5, the interior of the Gaza Province presents the pattern observed on the annual scale, being one of the places where the greatest temperature variations are registered, together with the northern part of the Tete Province and the interior of the Niassa and Zambézia Provinces. The change in average temperature can reach 1.4 °C in the 2040s, 2.12 °C in the 2070s, and 2.51 °C in the 2100s (Table 5). For the MAM station (Figures A6–A8, middle), the change in average temperature may reach 1.27 °C in the 2040s, 2.01 °C in the 2070s, and 2.69 °C at the end of the century. During the JJA and SON seasons (Figures A9–A14, middle), the major changes are also expected in the interior of the Gaza Province, the north of the Tete Province, and in some parts of the Niassa Province. During the 2040s, the change in average temperature only exceeded 1.5 °C in the SON season (Table 5), where it reaches 1.52 °C; in JJA, the average temperature reaches 1.47 °C. In the 2070s, the temperature rise exceeds 2 °C, but it does not reach 3 °C, and the change

in temperature reaches 2.23 °C in JJA and 2.6 °C in SON. For the 2100s period, the RCP4.5 scenario shows that the temperature rise will exceed the 3 °C barrier. Once again, the SON season is the one with the major increase in temperature, reaching 3.05, 3.03, and 3.06 °C, for the maximum, minimum, and average temperature, respectively.

In the RCP8.5 scenario, the same locations mentioned previously (inland Gaza Province, north of the Tete Province, and in some parts of the Niassa Province) are the ones that show the major changes. For the DJF station (Figure A3, Figure A4, Figure A5, right), the average temperature may reach 1.37 °C in the 2040s, 2.69 °C in the 2070s, and 4.39 °C at the end of the century (Table 6). During the MAM season (Figures A6–A8, right), the change in average temperature may reach 1.41 °C in the 2040s, 2.65 °C in the 2070s, and 4.59 °C in 2100s. The temperature increase could rise from 5 °C at the end of the 21st century, mainly during the JJA and SON seasons (Figures A9–A14, right). During the 2040s, RCP8.5 projections show that the average temperature rise will reach 1.63 °C in JJA and 1.64 °C in SON. In the 2070s, the change in average temperature will reach 2.92 °C in JJA and 3.28 °C in SON. At the end of the century, the average temperature change will reach 4.7 °C in JJA and 5.2 °C in SON (Table 6).

3.4. Changes in Annual and Seasonal Precipitation Projections (RCP2.6, RCP4.5, and RCP8.5)

3.4.1. Projected Changes in Annual Precipitation

In general, the behavior of annual precipitation shows a pattern with considerably variability influenced by the type of scenario and period chosen, including the geographic location. All RCPs are consistent in showing that at the annual time scale, there will be a decrease in precipitation in all periods in the coastal zone of the northern region (Figure 6). The projections under the RCP2.6 scenario (Figure 6, left) indicate that there will be an increase in precipitation in much of Mozambique, mainly in the 2040s, where the 5th and 95th percentiles will have values of −7.3% and 30.7%, respectively (Table 7). For almost the entire southern region, with the exception of the coastal part, precipitation may increase by up to 40% compared to the precipitation in the reference period. The same is true in some parts of the central and northern regions, in the northern part of the Tete Province, and some parts of the interior of the Niassa Province, where the increase in precipitation may exceed 50%. During the 2070s, there was a slight decrease in precipitation, with the 5th percentile equal to −16.4% and the 95th percentile equal to 22.1%. At the end of the century, precipitation showed a slight increase in relation to the 2070s, with the entire southern region with precipitation above the average of the reference period.

Table 7. Percentile values of precipitation for the 2040s (2011–2040), 2070s (2041–2070), and 2100s (2071–2100) with respect to the reference period (1961–1990) for the RCP2.6 scenario. The cells filled with different colors differentiate positive and negative anomalies.

Period	Reference Period		Change in 2040s			Change in 2070s			Change in 2100s		
	Average	Std. Dev.	P5	P50	P95	P5	P50	P95	P5	P50	P95
	(mm)		(%)	(%)	(%)	(%)	(%)	(%)	(%)	(%)	(%)
Annual	1020	246.3	−7.3	10.7	30.7	−16.4	2.1	22.1	−23.3	−8.3	7.2
DJF	186.2	47.6	−7.5	11.6	38.1	−13.8	6.7	31.4	−10.9	4.3	23.0
MAM	86.3	35.6	−1.9	21.5	49.4	−16.6	5.6	24.5	−6.6	17.0	40.4
JJA	23.5	12.6	−56.5	−31.8	1.0	−61.6	−33.4	−15.4	−55.3	−30.9	−6.8
SON	44.5	11.5	−18.2	−1.2	25.1	−26.9	−9.6	9.7	−15.2	2.4	26.2

The RCP4.5 and RCP8.5 scenarios (Figure 6, middle and right) present similar pattern for precipitation in almost all three analysis periods. For these projections, a large part of the southern region will show precipitation within or below the average of the reference period (up to about −30%), except for some parts of the interior of the Inhambane Province and parts of the provinces of the central and northern regions. In these places, the change in precipitation may reach 20%. From Tables 8 and 9, it is clear that projections show a decrease

in precipitation, with RCP4.5 showing the 50th percentile with a negative sign during the 2040s and 2070s periods, while RCP8.5 shows similar behavior for all periods. This shows that for these scenarios, most of the country will experience a decrease in precipitation.

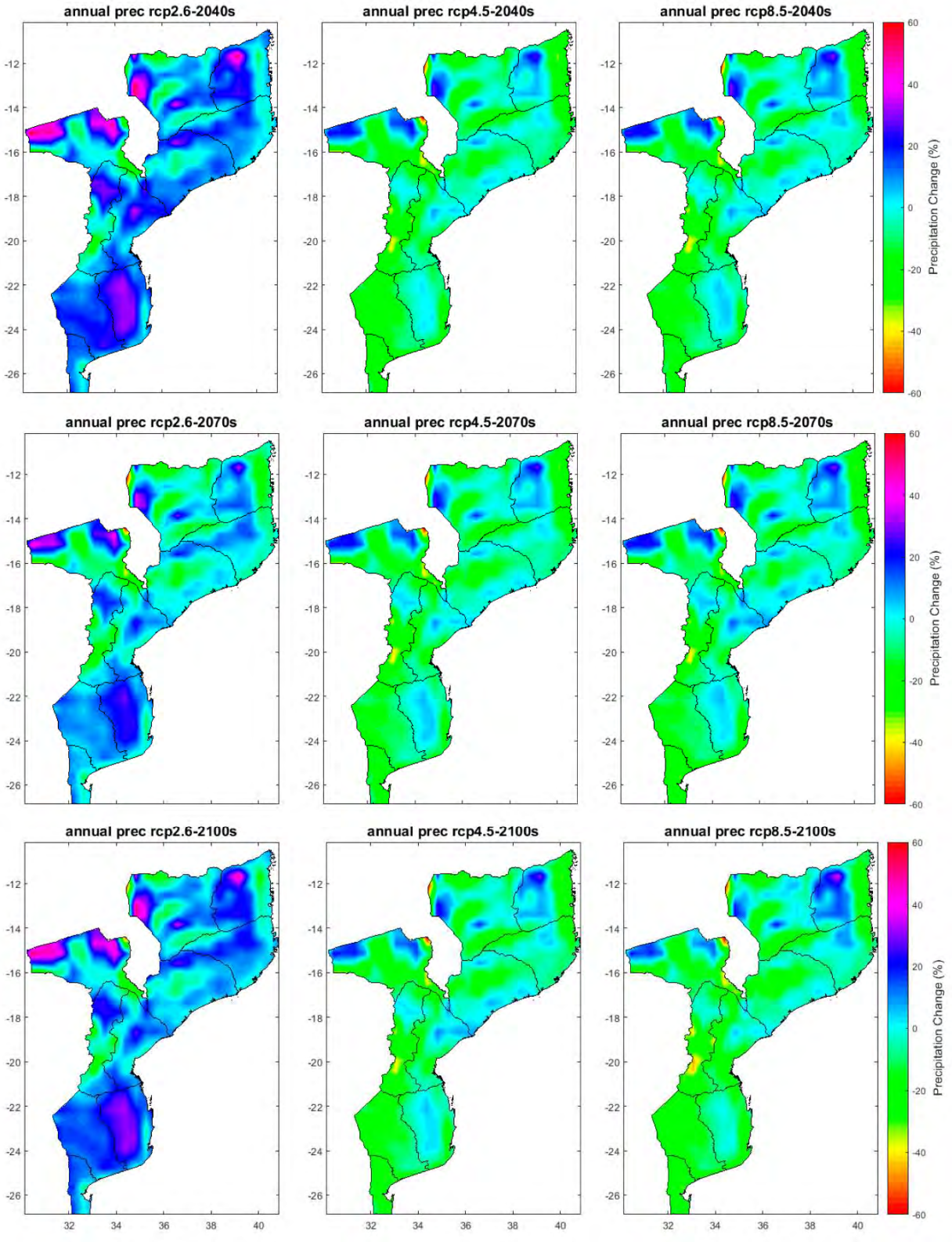

Figure 6. Projected changes in annual precipitation (%) for the 2040s (2011–2040), 2070s (2041–2070), and 2100s (2071–2100) with respect to the reference period (1961–1990) for the three RCPs scenarios (RCP2.6, RCP4.5, and RCP8.5).

Table 8. Percentile values of precipitation for the 2040s (2011–2040), 2070s (2041–2070), and 2100s (2071–2100) with respect to the reference period (1961–1990) for the RCP4.5 scenario. The cells filled with different colors differentiate positive and negative anomalies.

Period	Reference Period		Change in 2040s			Change in 2070s			Change in 2100s		
	Average	Std. Dev.	P5	P50	P95	P5	P50	P95	P5	P50	P95
	(mm)		(%)	(%)	(%)	(%)	(%)	(%)	(%)	(%)	(%)
Annual	1020	246.3	−23.8	−8.9	7.4	−22.6	−7.9	7.6	−14.5	4.5	23.7
DJF	186.2	47.6	−12.9	3.0	20.3	−10.4	6.0	25.4	−12.2	6.1	26.3
MAM	86.3	35.6	−18.2	3.9	25.1	−16.2	6.7	26.4	−12.8	10.9	31.6
JJA	23.5	12.6	−60.2	−33.4	−14.1	−61.1	−37.3	−19.9	−63.8	−39.5	−23.3
SON	44.5	11.5	−7.6	10.6	37.4	−15.9	2.1	33.5	−21.5	2.3	30.6

Table 9. Percentile values of precipitation for the 2040s (2011–2040), 2070s (2041–2070), and 2100s (2071–2100) with respect to the reference period (1961–1990) for the RCP8.5 scenario. The cells filled with different colors differentiate positive and negative anomalies.

Period	Reference Period		Change in 2040s			Change in 2070s			Change in 2100s		
	Average	Std. Dev.	P5	P50	P95	P5	P50	P95	P5	P50	P95
	(mm)		(%)	(%)	(%)	(%)	(%)	(%)	(%)	(%)	(%)
Annual	1020	246.3	−22.6	−7.0	9.8	−22.3	−6.6	9.8	−25.0	−10.0	9.5
DJF	186.2	47.6	−10.5	5.6	23.7	−8.2	8.3	26.3	−10.5	7.5	25.3
MAM	86.3	35.6	−15.8	5.6	25.3	−12.8	12.1	30.4	−16.1	5.9	27.9
JJA	23.5	12.6	−60.9	−33.6	−13.1	−63.9	−40.3	−24.9	−67.8	−47.0	−31.1
SON	44.5	11.5	−11.1	11.0	39.2	−16.1	6.1	30.9	−32.6	−6.0	28.6

3.4.2. Projected Changes in Seasonal Precipitation

In general, the behavior of seasonal precipitation shows a variable pattern similar to the pattern of annual precipitation, which is probably influenced by the same factors. All RCP scenarios point to above average precipitation in much of Mozambique during the DJF season (Figure A15), regardless of the period. The projections under the RCP2.6 scenario (Figure A15, left) show that during the DJF season, the entire southern region will show an increase in precipitation, which may exceed the historical average by more than 40%. The 5th and 95th percentile values are −7.5% and 38.1%, in the 2040s, −13.8% and 31.4%, in the 2070s, and −10.9% and 23% at the end of the century (Table 7).

For the RCP 4.5 and 8.5 scenarios (Figure A15, middle and right), there is a decrease in precipitation in the interior of the central and southern regions. For RCP4.5, the 5th and 95th percentiles are −12.9% and 20.3% in the 2040s, −10.4% and 25.4% in the 2070s, and −12.2% and 26.3% in the 2100s (Table 8). The RCP8.5 scenario presents changes in precipitation with values within the same magnitude. At the MAM season (Figure A16), similarly to the DJF season, projections under RCP2.6 point to an increase in precipitation in much of Mozambique, mainly in the 2040s (Figure A16, left) and 2100s. During these periods, the increase in precipitation may reach 60%, mainly in the north of the Tete Province and some parts of the Manica and Niassa Provinces. For the RCP4.5 and RCP8.5 scenarios (Figure A16, middle and right), the pattern is similar to that seen in the DJF season.

During the JJA season (Figure A17), all scenarios show that in almost all of Mozambique, there will be a decrease in precipitation, mainly for scenarios RCP4.5 and 8.5 (Figure A17, middle and right). The north of the Tete Province, the interior of the Niassa Province, and parts of the Cabo Delgado Province are the places where an increase in precipitation is expected, with values not exceeding 30%. The interior part of Mozambique will have a robust decrease in precipitation, reaching a variation of −60% in most of the provinces of Gaza, Tete, and Niassa. In this season, the 5th and 95th percentiles show negative values regardless of the period or scenario, except for the 95th percentile of RCP2.6, which is 1% during the 2040s (Table 7).

For the SON season (Figure A18), the projections under the RCP4.5 and RCP8.5 scenarios (Figure A18, middle and right) show a pattern of increased precipitation in the central and northern regions and of decreased precipitation in the south at the end of the century, where the change in precipitation could reach −40%. On the other hand, the RCP2.6 scenarios (Figure A18, left) show that there will be a decrease in precipitation in central Mozambique in the 2040s and 2100s and a decrease in almost the whole country in the 2070s.

3.5. Robustness of Projected CORDEX Model Simulations

Tables 10–12 show the change in temperature and precipitation projections, including the robustness test for the 20 districts divided by the four sub-regions used in this study. The results in bold are for the places where the change is robust. The results of the change in temperature are in accordance with the analysis in the previous section, with coastal districts having the least variation and districts in the south and center having the greatest variation. For temperature, all districts show robust changes, regardless of RCP and period.

For the precipitation simulations of RCP2.6 (Table 10), it is noticed that most districts present a robustness in the signal agreement, mainly in the districts of the coastal, central, and northern regions. In the districts of the southern region, the fact that none of them passed both tests in the 2070s stands out. In terms of combination, the districts of Beira, in the coastal region, Muidumbe and Chimbonila in the north, and Zumbo in the central region showed a robust change in precipitation in the 2040s. In the 2070s, only the districts of Beira, Muidumbe, and Chimbonila experienced a robust change. In the 2100s, the districts of Mangaja da Costa, Nampula, Chimbonila, Zumbo, and Mocuba show robustness in precipitation change. According to the table, no district in the southern region has a robust change in precipitation for the simulations of RCP2.6.

Table 10. Changes in future projections for RCP2.6 temperature and precipitation simulations. Results in bold show where the changes are robust.

Region	District	Temperature (°C)			Precipitation (%)		
		2040s	2070s	2100s	2040s	2070s	2100s
Coastal	Govuro	0.89	1.23	1.13	24.6	22.0	22.3
	Massinga	0.88	1.21	1.09	30.0	23.9	27.7
	Moc. Praia	0.97	1.29	1.24	26.8	17.0	17.7
	Nacala	0.95	1.23	1.19	14.6	12.7	14.5
	Mang. Costa	0.90	1.29	1.17	26.0	15.9	17.1
	Beira	0.89	1.24	1.13	28.8	20.3	22.9
	Xai-Xai	0.92	1.30	1.16	12.1	8.2	8.8
	Manhiça	0.95	1.31	1.18	7.6	8.4	7.3
Northern	Muidumbe	0.99	1.35	1.29	22.4	14.1	17.3
	Balama	0.96	1.36	1.31	15.1	11.4	12.9
	Nampula	0.96	1.33	1.27	13.6	10.4	12.3
	Chimbonila	1.01	1.41	1.31	7.8	4.3	7.4
Central	Zumbo	1.15	1.62	1.43	20.7	15.0	24.6
	Chemba	1.05	1.52	1.35	14.1	6.5	9.8
	Mocuba	0.93	1.28	1.23	19.6	11.9	15.6
	Sussundenga	1.03	1.45	1.30	11.8	4.4	9.3
Southern	Massangena	1.14	1.52	1.37	9.4	9.8	12.1
	Chigubo	1.09	1.48	1.33	14.8	97	11.7
	Massingir	1.08	1.49	1.33	7.6	2.1	4.9
	Namaacha	1.02	1.38	1.25	0.4	1.2	1.4

Table 11. Changes in future projections for RCP4.5 temperature and precipitation simulations. Results in bold show where the changes are robust.

Region	District	Temperature (°C)			Precipitation (%)		
		2040s	**2070s**	**2100s**	**2040s**	**2070s**	**2100s**
Coastal	Govuro	1.06	1.72	2.12	−2.4	−1.2	1.3
	Massinga	1.06	1.72	2.10	−12.9	−11.5	−12.3
	Moc. Praia	1.07	1.72	2.12	−25.6	−24.1	−24.6
	Nacala	1.05	1.70	2.10	−7.7	−8.9	−7.8
	Mang. Costa	1.12	1.81	2.22	17.1	14.6	17.1
	Beira	1.07	1.74	2.12	−5.2	−6.3	−4.7
	Xai−Xai	1.13	1.84	2.23	−11.5	−9.7	−12.9
	Manhiça	1.13	1.86	2.24	−21.2	−20.0	−22.1
Northern	Muidumbe	1.10	1.84	2.37	1.2	2.4	1.7
	Balama	1.17	1.99	2.68	**20.9**	**22.3**	**21.3**
	Nampula	1.16	1.95	2.53	6.7	**5.4**	5.9
	Chimbonila	1.21	2.22	3.18	**30.2**	**28.0**	**27.1**
Central	Zumbo	1.29	2.16	2.55	−31.2	−28.3	−28.7
	Chemba	1.21	1.96	2.41	−7.3	−6.4	−5.4
	Mocuba	1.16	1.90	2.33	7.2	6.9	7.1
	Sussundenga	1.20	1.97	2.42	−12.4	**−12.3**	−12.8
Southern	Massangena	1.28	2.03	2.52	−9.2	−6.9	−11.5
	Chigubo	1.27	2.02	2.49	−2.1	2.3	−1.3
	Massingir	1.32	2.13	2.56	−0.8	−0.3	−0.5
	Namaacha	1.17	1.96	2.34	2.5	0.6	−0.1

Table 12. Changes in future projections for RCP4.5 temperature and precipitation simulations. Results in bold show where the changes are robust.

Region	District	Temperature (°C)			Precipitation (%)		
		2040s	**2070s**	**2100s**	**2040s**	**2070s**	**2100s**
Coastal	Govuro	1.14	2.25	3.49	−2.6	−0.4	−8.4
	Massinga	1.12	2.24	3.65	−12.4	−13.6	−17.4
	Moc. Praia	1.15	2.27	3.72	−23.6	−23.8	−21.5
	Nacala	1.13	2.24	3.64	−4.9	−7.3	−5.4
	Mang. Costa	0.16	1.42	3.72	16.5	17.4	12.7
	Beira	1.16	2.26	3.67	−8.0	−5.1	−11.8
	Xai−Xai	1.20	2.39	3.90	−10.8	−12.6	−16.4
	Manhiça	1.21	2.41	3.93	−20.4	−22.7	**−25.7**
Northern	Muidumbe	1.20	2.37	3.87	3.9	4.9	8.0
	Balama	1.25	2.48	4.03	24.6	**24.5**	**26.0**
	Nampula	1.26	2.49	3.98	8.7	7.6	9.9
	Chimbonila	1.31	2.61	4.24	29.9	**30.4**	**27.2**
Central	Zumbo	1.38	2.93	4.60	−28.2	−26.7	−26.7
	Chemba	1.31	2.56	4.21	−6.6	−1.7	−8.1
	Mocuba	1.23	2.51	4.05	7.9	11.0	5.0
	Sussundenga	1.32	2.58	4.06	−13.6	**−12.7**	**−18.9**
Southern	Massangena	1.37	2.65	4.37	−10.3	−6.2	−13.8
	Chigubo	1.35	2.67	4.15	−1.9	1.9	−4.2
	Massingir	1.41	2.75	4.51	0.2	0.3	−5.0
	Namaacha	1.28	2.55	3.98	1.5	−0.7	−4.5

For the precipitation simulations of RCP4.5 (Table 11), there is a slight increase in districts that pass the test of significance and a decrease in districts that pass the test of agreement of the sign of change. The fact of having only four simulations of RCP2.6, in relation to nine simulations of RCP4.5, may have contributed to this difference, mainly

with regard to the test of agreement. For the RCP4.5 simulations, no district in the coastal and southern regions passed the combination of the two tests. The districts of Balama and Chimbonila, in the northern region, passed the tests regardless of the period. Still, in the northern region, the districts of Nampula and Muidumbe passed both tests in the 2070s and 2100s, respectively. The district of Sussundenga is the only one that passed both tests, in the central region, in the 2070s.

For the assessment of robustness for the precipitation simulations of RCP8.5 (Table 12), similar to the simulations of RCP2.6 and RCP4.5, no district in the southern region passed the combination of the two tests. The districts of Balama and Chimbonila, in the northern region, passed the tests regardless of the period, while still in this region, the districts of Muidumbe and Nampula passed both tests in the 2040s and 2070s, respectively. In the coastal region, the districts of Beira and Manhiça passed both tests in the 2040s and 2100s. Finally, in the central region, only the district passes the two tests, in the 2070s and 2100s.

4. Discussion and Conclusions

To determine climate change adaptation responses under different future climate projections with reduced uncertainty and particularly at regional, countrywide, or local levels at which important and actionable policy decisions are made requires reliable climate projections. This requires evaluation of climate projection in terms of comparison with other sources of data, also in terms of their robustness and significance [94]. The scarcity of dedicated studies on climate change projections at local levels is an undeniable fact. While efforts are taken to improve the accuracy of climate change projections, publications or studies focusing on regional, countrywide, and local levels should be increased. Publications available to date on climate projections at the aforementioned levels are very limited for Mozambique [3,95].

In this study, we analyzed the results of a multi-model ensemble based on nine models derived from the COordinated Regional Downscaling EXperiment (CORDEX) initiative and examined climate change projections of temperature and precipitation over Mozambique. These changes were calculated and analyzed for Mozambique taking into account its four sub-regions, namely, coastal, northern, central, and southern, considering three 30-year time periods, the 2040s (present 2011–2040), the 2070s (mid 2041–2070), and the 2100s (end 2071–2100) under the Representative Concentration Pathways RCP2.6, RCP4.5, and RCP8.5, relative to the baseline period (1961–1990).

The results show that future warming is not uniform over Mozambique and varies from region to region. Projected temperatures (maximum, minimum, and average) show an upward trend in most of the country in particular for the RCP4.5 and RCP8.5 scenarios.

Under the RCP2.6, for the present (end) period, the maximum temperature increases by 0.8 °C (1.1 °C), the minimum temperature increases by ≈1.0 °C (≈1.2 °C), and the average temperature increases by ≈0.9 °C (≈1.2 °C).

Under the RCP4.5, the maximum temperature increases by ≈1.2 °C (2.4 °C), the minimum temperature increases by ≈1.3 °C (≈2.5 °C), and the average temperature increases by ≈1.3 °C (≈2.4 °C).

Under the RCP8.5, the maximum temperature increases by ≈1.2 °C (2.4 °C), the minimum temperature increases by ≈1.3 °C (4.1 °C), and the average temperature increases by ≈1.3 °C (4.3 °C).

The projected changes in average temperature in this study are consistent with regional estimates (≈1.2 °C (≈1.3 °C), ≈1.4 °C (≈2.3 °C), and ≈1.7 °C (4.1 °C) under RCP2.6, RCP4.5 and RCP8.5, respectively) obtained from CMIP6 [88] for the sub-region of South East AFrica (SEAF) which includes Mozambique.

These increases, especially under the RCPs 4.5 and 8.5 already surpassed the Paris Agreement policy responses to climate change targets [19], which states the need for maintaining temperatures at present levels while assessing the implications that could arise if warming overcomes 1.5–2 °C. These increases in temperature, particularly the maximum

temperature, are expected to impact socio-economic sectors, in particular the agricultural sector.

The largest warming (hotspots) in the country are projected to occur under RCP4.5 and RCP8.5 mainly over parts of Gaza, parts of the central region, and parts of Niassa in the north. These regions are projected to have their maximum temperature increasing by ≈0.9 °C (≈1.2 °C), minimum temperature increasing by ≈1.1 °C (1.4 °C), and average temperature increasing by ≈1.0 °C (≈1.3 °C) under RCP2.6. Under RCP4.5, the maximum temperature increases by ≈1.4 °C (2.7 °C), the minimum temperature increases by ≈1.5 °C (≈2.8 °C), and the average temperature increases by ≈1.4 °C (≈2.7 °C). Under RCP8.5, the maximum temperature increases by ≈1.5 °C (4.7 °C), the minimum temperature increases by ≈1.6 °C (4.9 °C), and the average temperature increases by ≈1.5 °C (4.7 °C). The regions of Gaza and central region are predominately semi-arid and experience frequent droughts, and hence, they are the most likely to experience increased risk of inland crop failure, which can be expected to affect a huge number of communities [96] as a result of serious water shortages. The high vulnerability of the population in the arid and semi-arid regions encouraged the Government of Mozambique to initiate several important investments locally. One of these investments was the United Nations Joint Programme (UNJP) on Environmental Mainstreaming and Adaptation to Climate Change for the period between 2008 and 2012 (total of US$7 million), which identified at the farm and community level adaptive interventions that have been tested and applied as well as showed a positive impact on productivity, broadening of the livelihood basis, and improving resilience to climate change [97]. On the other hand, Niassa is among the most irregular rainfall regimes in the northern region of the country [98]. Increased temperatures due to climate change may result in a decrease soil moisture, which in turn promotes increased evapotranspiration loss from open water bodies, soils, and vegetation [3].

With these projected temperature increases, particularly the hotspots, it is likely that some of the aforementioned areas, particularly in the north, will experience normal to extreme floods more frequently. In contrast, the southern region where the largest warming is expected is likely to deal with more frequent droughts and other induced hazards.

These results are supported to some extent by previous studies [3,31,56,95]. Notably, the magnitude of change in the aforementioned scenarios shows an increase in temperature up to ≈5 °C on the interior and less toward the coast of the Mozambique. This result is consistent with the study by [3] in which temperature increased up to 6 °C by 2100 based on an A2 emission scenario (equivalent to the RCP8.5 scenario). The difference in relation to our results can be explained by the outputs of the models used, since there was no downscaling based on local observations for this study. Another result consistent with the study by [3] is related to the fact that at a seasonal time scale, the SON period presents the greatest change in temperature.

One important finding of this study is that projected increases in temperature over most of the country indicate higher values for the worst level case scenario (RCP8.5) than for the medium level case scenario (RCP4.5) and for the low level case scenario (RCP2.6). The latter options have less impact and are more convenient for the world's governments and other institutions for decision making, since they lead to medium/small temperature increases. If the world follows the two pathways, medium/less adaptation will be needed and medium/low costs implications will likely occur.

Projected precipitation changes over Mozambique show substantial spatial and temporal variations. Analysis for the present (end) period presented different patterns under the RCP pathways.

Under the RCP2.6, annual precipitation change is projected to vary from −10 to 30 (−20 to 30)%, with substantial decreases occurring in the northern coastal zone, the interior of the central and northern regions, by −30 (−40)% and the increases occurring optimistically in the southern region and substantial increases in some parts of the central and northern regions by 50 (50)%. The 5th percentile and 95th percentile show values of

−7.3 (−23.3)% and 30.7 (7.2)%, respectively. These results show a tendency of precipitation decrease over time in most of the country.

Under RCP4.5, annual precipitation is projected to decrease over most of Mozambique by −20 (−20)%, with some hotspots showing substantial decreases such as those occurring in the interior of central and Niassa Province by −50 (−60)%, and substantial increases occurring north of Tete Province and parts of the northern region by 25 (30)%. The 5th percentile and 95th percentile show values of −23.8 (−14.5)% and 7.4 (23.7)%, respectively.

Under RCP8.5, annual precipitation is projected to decrease over most of Mozambique by −30 (−30)%, with hotspots indicating substantial decreases for example occurring in the interior of central and Niassa Province by −50 (−60)%, and the highest increases occurring north of the Tete Province and parts of the northern region by 30 (30)%. The 5th percentile and 95th percentile show values of −22.6 (−25)% and 9.8 (9.5)%, respectively.

The results of precipitation analyses point out that under the RCP2.6 scenario, the southern region will experience an increase of precipitation over time. On the other hand, projected precipitation under the RCP4.5 and RCP8.5 scenarios shows that over the southern region, there will be a decrease of precipitation over time, mainly in interior areas. This suggests that long drought periods are likely to be the dominant factor for the southern region climate. The central and northern region results show a complex pattern of projected precipitation change, with a decrease over most of the northern region under the RCP2.6 scenario and an increase under the RCP4.5 and RCP8.5 scenarios. From the point of view of agriculture, the central and northern regions are likely to be more suitable for the cultivation of crops under a precipitation-increasing tendency, while under a precipitation-decreasing tendency, these areas will demand more water for the crops or increase water stress and drought conditions.

Similar findings on projected precipitation changes were also verified by [56], although their analysis was not so localized. Other researchers [31] also found a robust decrease in precipitation accompanied by increases in the number of consecutive dry days and decreases in consecutive wet days over most of the central African subcontinent, including parts of northern Mozambique under RCP8.5.

Studies assessing impacts of hydropower generation in Mozambique found temperature and precipitation to have a critical role since the projected increasing in temperature will increase evaporation, while the projected reduction in precipitation will affect the potential for hydropower generation [33]. Kariba and Cahora Bassa are among the major dams in the Zambezi river system, presenting two vivid examples that will be substantially affected by increased evapotranspiration and decreased precipitation due to climate change.

The assessment of the performance of model outputs in relation to historical data showed that all models have good correlations with the observations (above 0.7) in almost all stations, except in Pemba, where the correlations are above 0.5. The associated errors vary between 0.25 and 2 °C, with the standard deviation not exceeding 3 °C. The average of the models presents the best results in the evaluation, where their correlation reaches more than 0.9. For precipitation, correlations are below 0.5 in most stations; only Nampula and Lichinga present correlations that reach 0.75 and 0.77, respectively. The errors vary between 100 and 200 mm. Similar to what was observed in the temperature, the average of the models presents the best results also for precipitation, reaching 0.79 in Nampula and 0.82 in Lichinga.

Regarding future simulations, the robustness of the change through the combination of the signal agreement and Student t-test was performed. The analysis of the robustness of the change in future simulations is important to assess the level of uncertainty in relation to the projections, mainly of precipitation, which is the variable that presents the great variability, both temporal and spatial. The results show that in all regions and for all periods, the change in temperature is robust. Regarding the change in precipitation, the northern region is the one that presents most of the districts that pass the two robustness tests for the three projection periods (2040s, 2070s, and 2100s). On the other hand, the coastal and southern regions are the ones that have more districts that do not pass the tests,

whereas in the southern region, no district passed the tests in the three periods of analysis. The high spatial and temporal variability of precipitation, and the fact that the simulation was downscaled over the African region, not at the country level, may have influenced the poor robustness of the precipitation projections.

A special highlight derived from the analysis goes to the central region, which is extremely vulnerable to all types of natural disasters and weather-related events, which are likely induced by ongoing climate change. The complexity of the climate patterns in this region calls for profound climate risk monitoring, risk preparedness, and resilience actions as well as more dedicated climate studies.

This study is perhaps among the first of its kind using CORDEX Climate model ensemble outputs to assess climate projections over Mozambique (countrywide), based on the Representative Concentration Pathways (RCPs) to update previous studies conducted with Special Emission Scenarios (SRES), among others. This piece of work represents a contribution aiming to respond to the impacts of climate change already happening in Mozambique and elsewhere. The significance of this work lies in the fact that this information is particularly needed to support decision making at different levels: policy, government sectors, scientific community, associations, civil society, and other types of organizations. In particular, the expanded uncertainties associated with the increasing climate variability and climate change (global warming) make such decisions and public participation even more daunting. This fact points to the need for more reliable, tailored climate information to adequately attend different and specific user needs.

In this paper, we show that improved climate information of high resolution freely available from web portals can be used to study the behavior of our climate system with an eye to the past, present, and future changes over time in a specific domain, particularly under but not limited to the human influence. This is crucial, because accessing this information, which contains key indicators that characterize the state of the climate represents an open window for the scientific community to conduct timely and systematic assessments on the patterns of change, thus improving our understanding of how climate change becomes a major concern to the survival of human beings as it poses significant risks and impacts on the natural resources, environment, and surrounding assets. Finally, we are able to discuss and present results that can be used as reference material for decisions processes, climate change projects, interventions, and also for education purposes.

Author Contributions: Conceptualization, A.F.M., B.E.B. and A.J.Q.; methodology, A.F.M., B.E.B. and O.A.M.; software, A.F.M. and B.E.B.; validation, A.F.M., A.J.Q. and B.E.B.; formal analysis, A.F.M., B.E.B., O.A.M. and. A.J.Q.; investigation, A.F.M., B.E.B., O.A.M. and. A.J.Q.; resources, A.F.M.; data curation, A.F.M. and B.E.B.; writing—original draft preparation, A.F.M. and B.E.B.; writing—review and editing, A.F.M., B.E.B., O.A.M. and. A.J.Q.; visualization, B.E.B.; supervision, A.F.M., B.E.B., O.A.M. and. A.J.Q.; project administration, A.F.M.; funding acquisition, A.F.M. All authors have read and agreed to the published version of the manuscript.

Funding: This research work was funded by the European Union, La Réunion Regional Council and the French state under the framework of the INTERREG-5 Indian Ocean 2014–2020 project "ReNovRisk-Cyclone and Precipitation".

Institutional Review Board Statement: Not applicable.

Informed Consent Statement: Not applicable.

Data Availability Statement: The numerical models outputs (CanESM2, CNRM-CM5, CSIRO-MK3, GFDL-ESM2M, HadGEM2-ES, IPSL-CM5A-MR, MIROC5, MPI-ESM-LR, Nor-ESM1-M) used in this study can be downloaded following specific guiding instructions and steps available at http://www.csag.uct.ac.za/cordex-africa/how-to-download-cordex-data-from-the-esgf. Other data presented in this study are not publicly available. These data are available on request from INAM (Instituto Nacional de Meteorologia, Maputo, Moçambique).

Software: The data analysis and output for this paper was generated using (i) [ArcGIS] software, Version [10.5.1], from the Department of Geology, Faculty of Sciences, Eduardo Mondlane University (UEM), Maputo, Mozambique; (ii) ENVI 5.1 and IDL software, Version [8.5,], License number 406564

(student version), from Stockholm University, Sweden, and (iv) Matlab software, Version [10a], License number 506085, from the Department of Physics, Faculty of Sciences, UEM, Maputo, Mozambique.

Acknowledgments: The authors thank Eduardo Mondlane University, Faculty of Sciences (UEM-FC) in Maputo, Mozambique, where all computer work was conducted. including the software facilities provided by the Departments of Geology and Physics. They also give thanks to the National Institute of Meteorology for providing station data for validation analysis. The authors also thanks the climate modeling groups and their respective institutions (aforementioned in Table 1) and the COordinated Regional Downscaling EXperiment (CORDEX) for producing and making their model output archived via Earth System Grid Federation (ESGF) Swedish datanode (https://esg-dn1.nsc.liu.se/projects/esgf-liu/) and freely available (access on February 2020).

Conflicts of Interest: The authors declare no conflict of interest with regard to this work and publication in this journal.

Appendix A

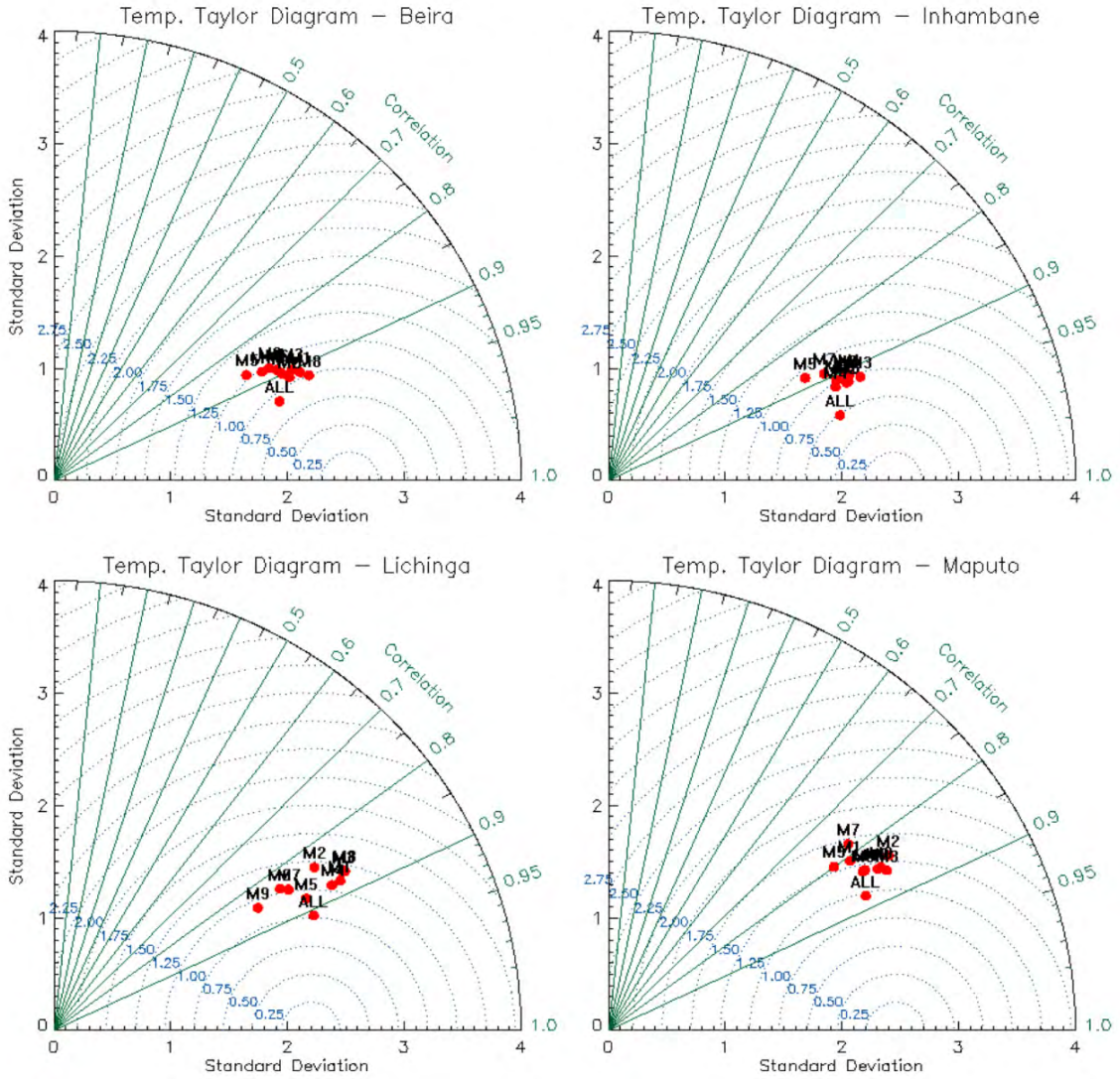

Figure A1. *Cont.*

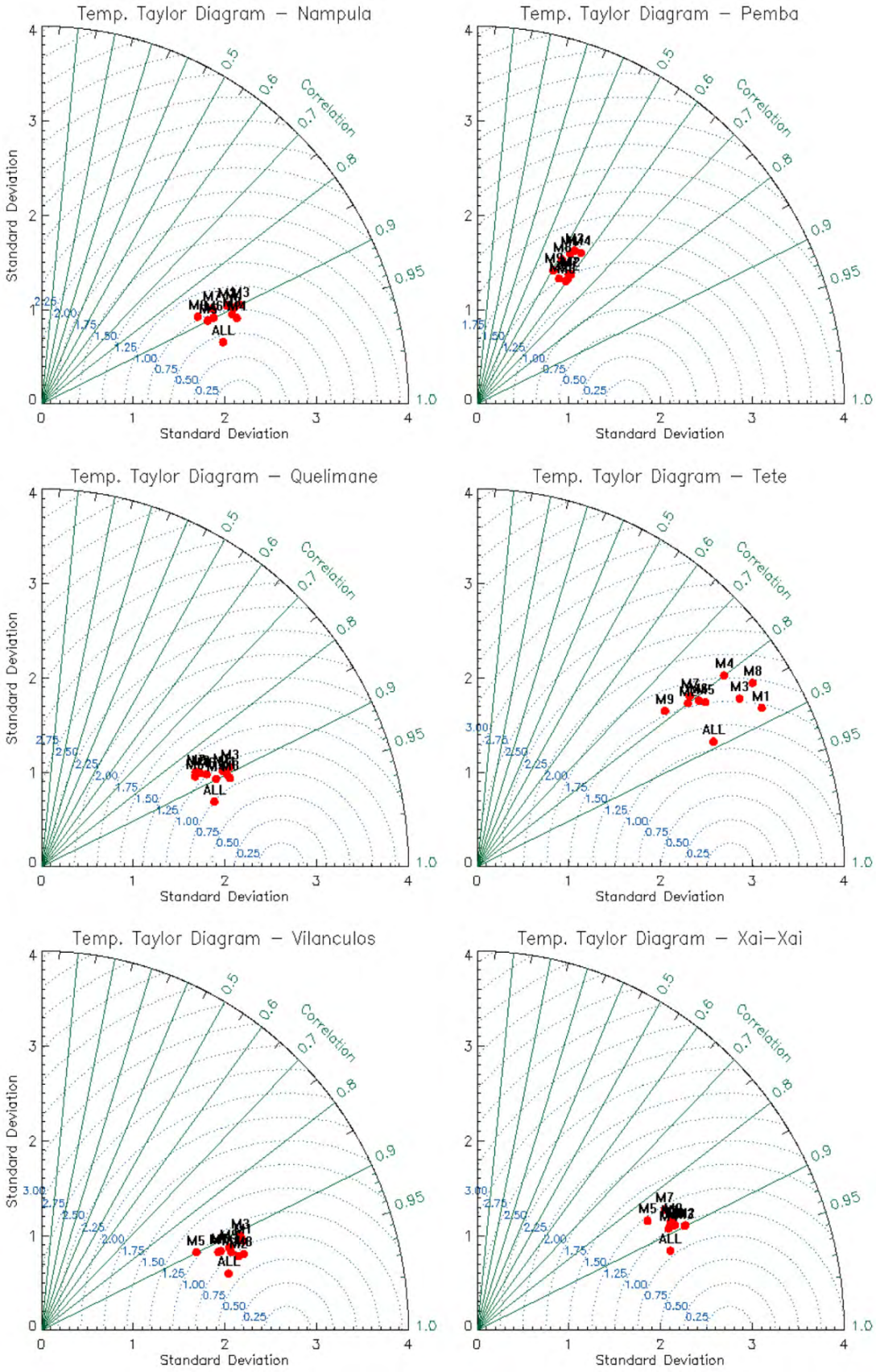

Figure A1. Taylor diagrams for temperature evaluation in Beira, Inhambane, Lichinga, and Maputo stations; Nampula, Pemba, Quelimane, Tete, Vilanculos, and Xai-Xai stations.

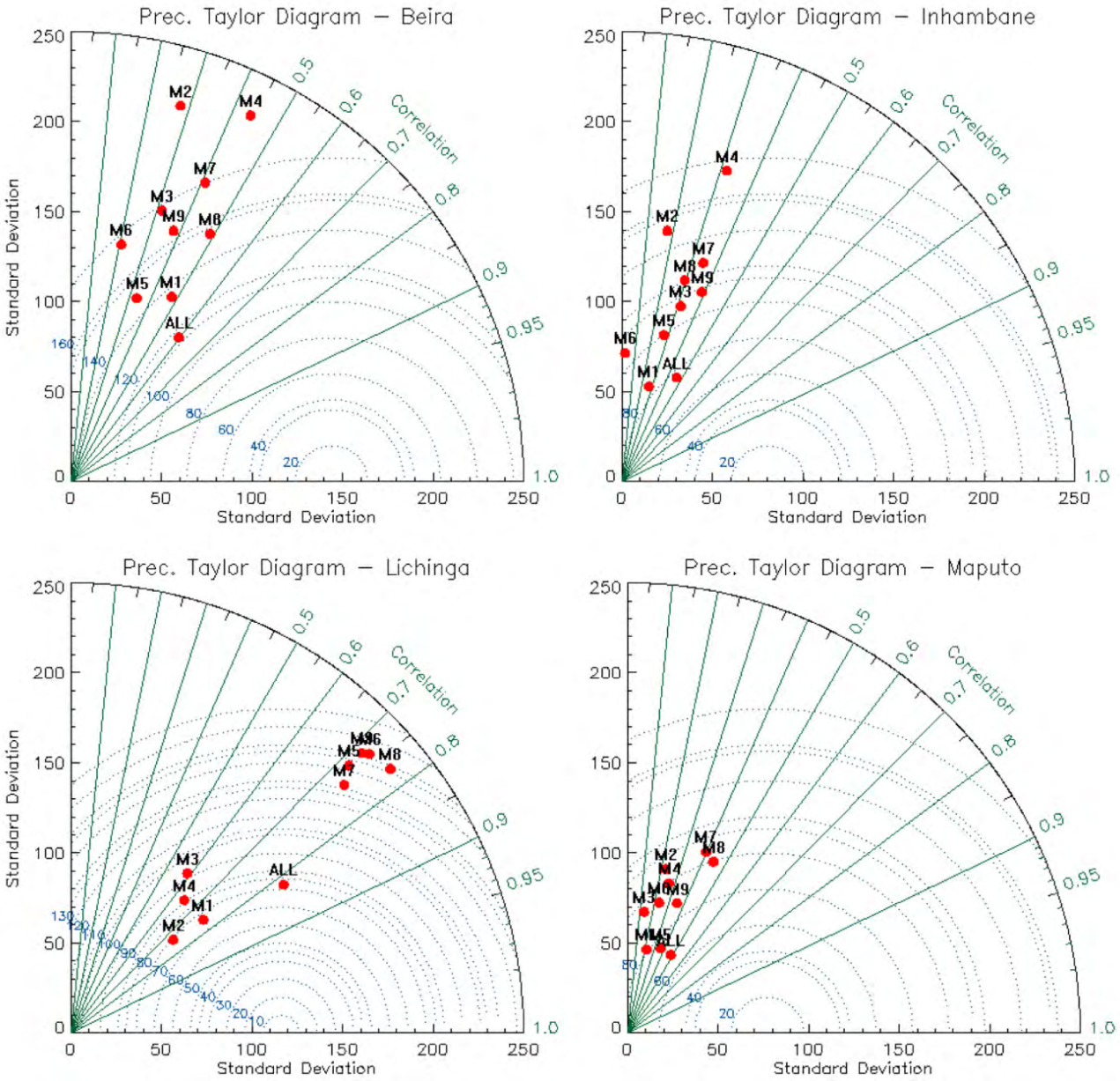

Figure A2. *Cont.*

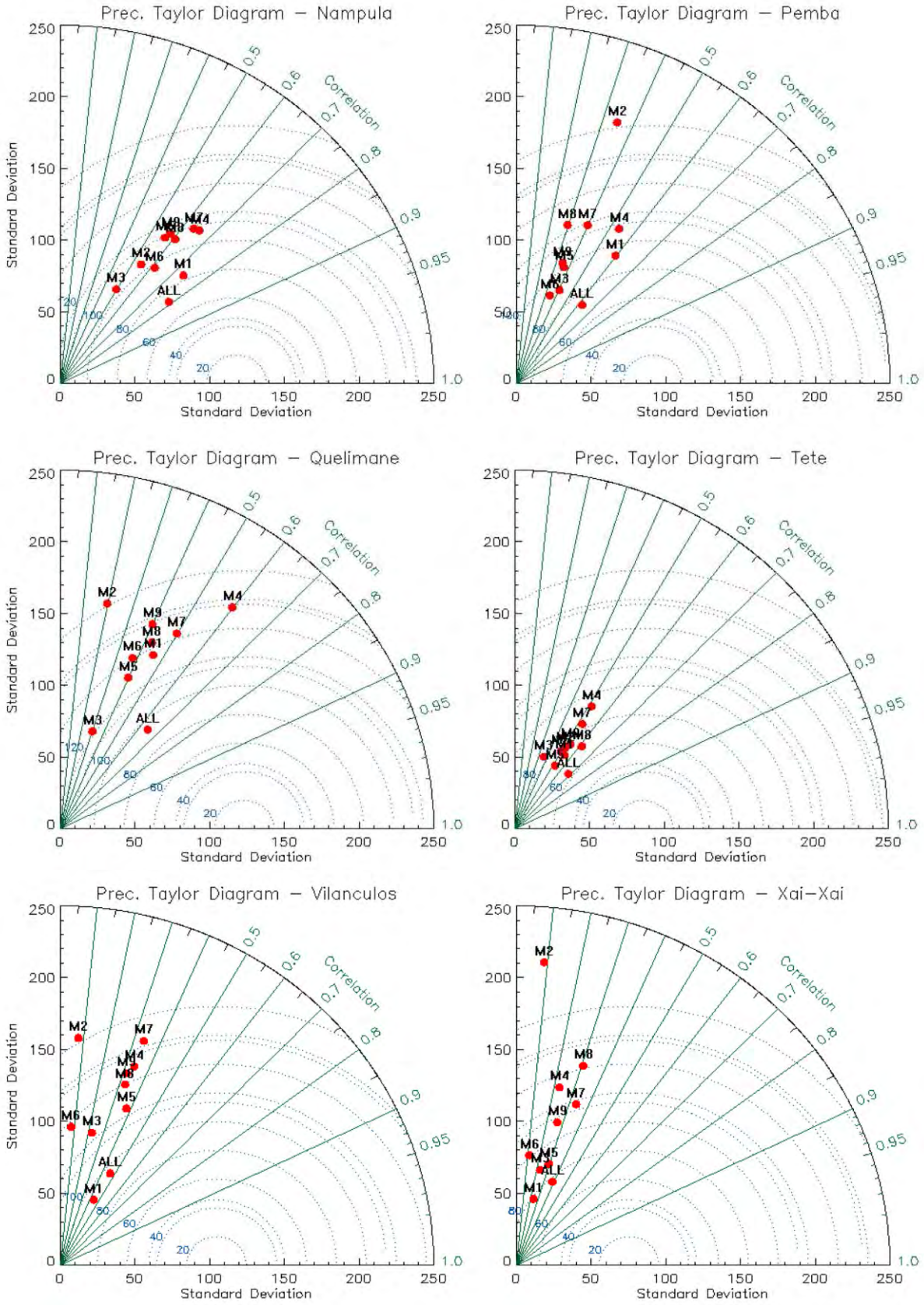

Figure A2. Taylor diagrams for precipitation evaluation in Beira, Inhambane, Lichinga, and Maputo stations; Nampula, Pemba, Quelimane, Tete, Vilanculos, and Xai-Xai stations.

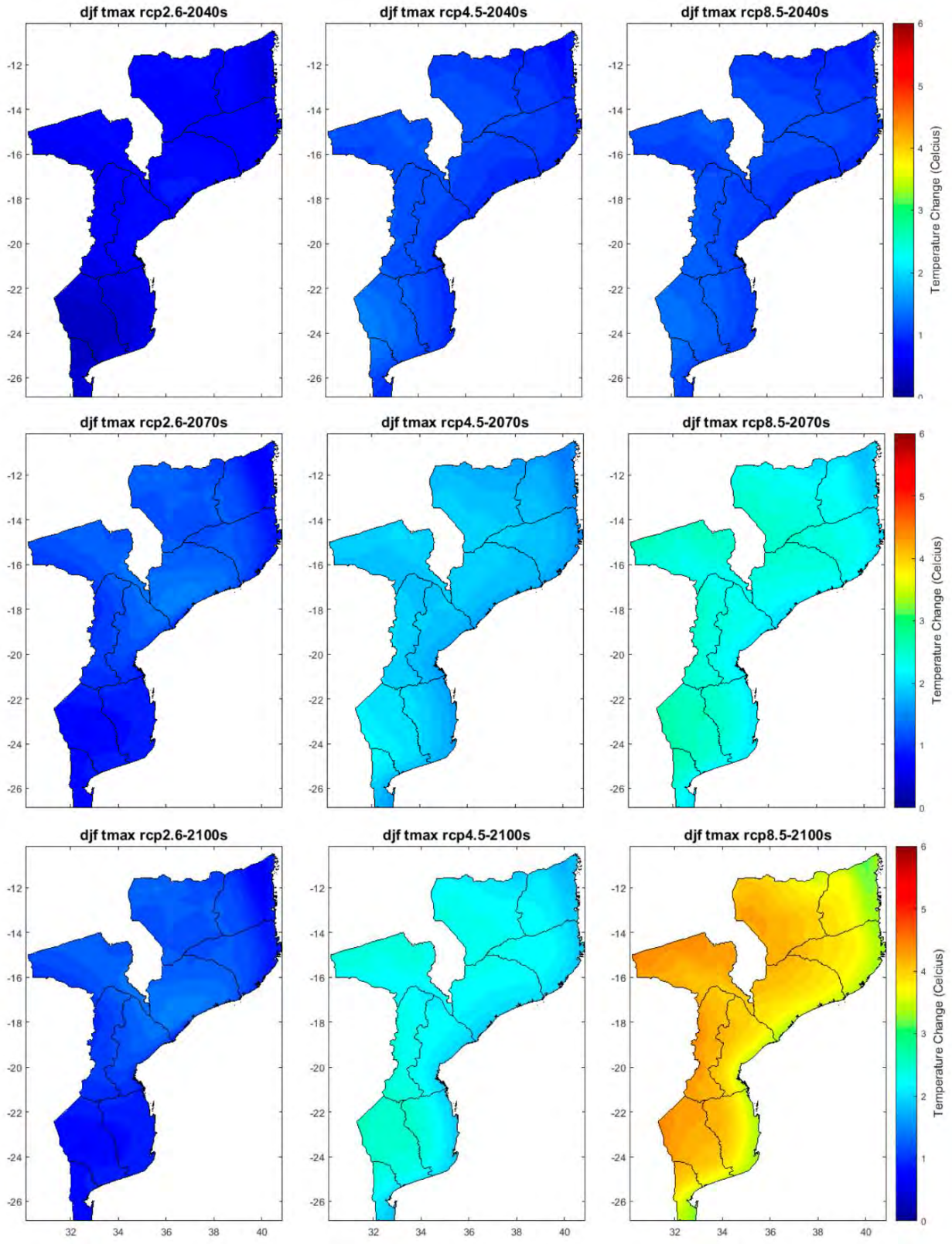

Figure A3. Projected changes of DJF maximum temperature for the 2040s (2011–2040), 2070s (2041–2070), and 2100s (2071–2100) with respect to the reference period (1961–1990) for the three RCP emission scenarios (RCP2.6, RCP4.5, and RCP8.5).

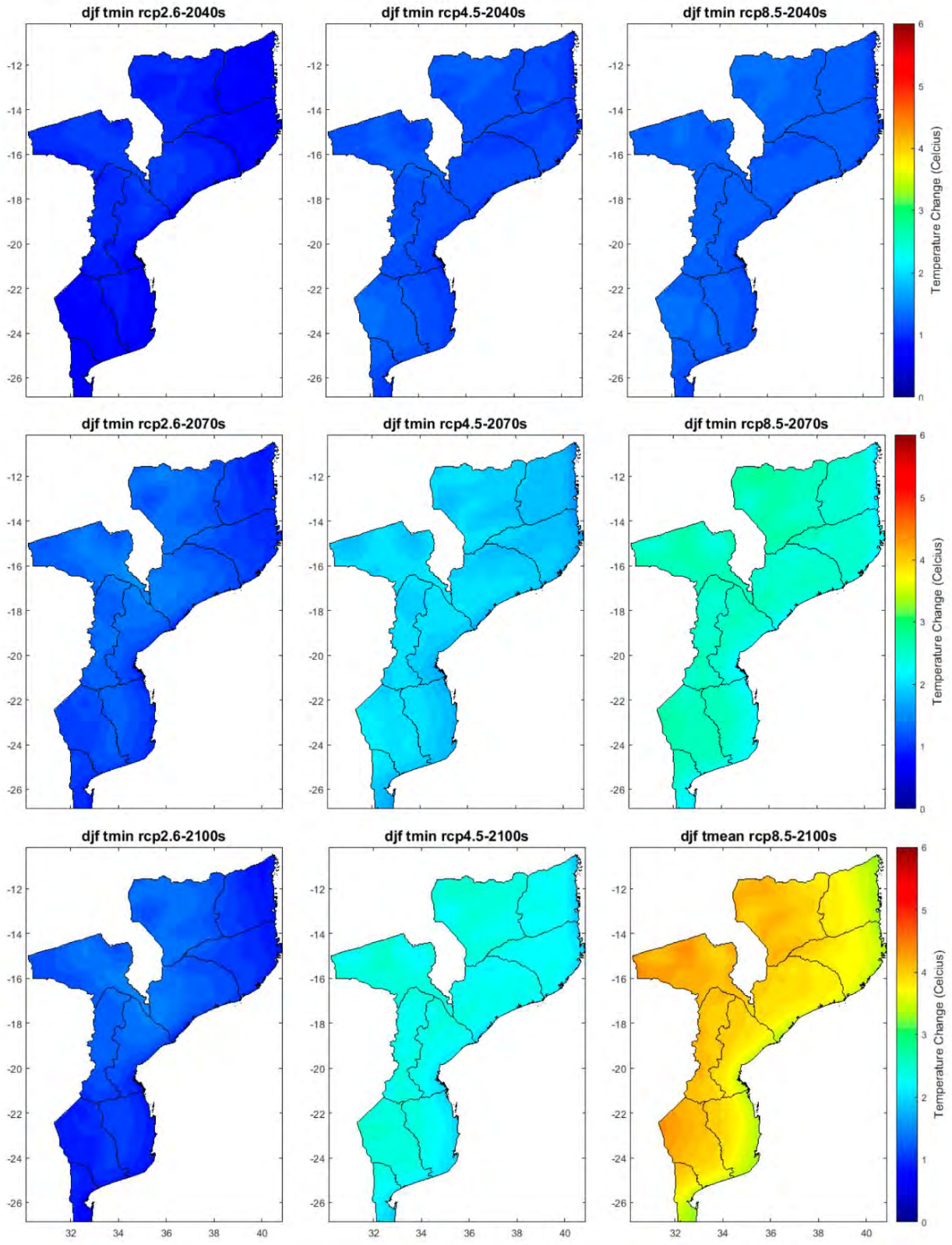

Figure A4. Projected changes of DJF minimum temperature for the 2040s (2011–2040), 2070s (2041–2070), and 2100s (2071–2100) with respect to the reference period (1961–1990) for the three RCP emission scenarios (RCP2.6, RCP4.5, and RCP8.5).

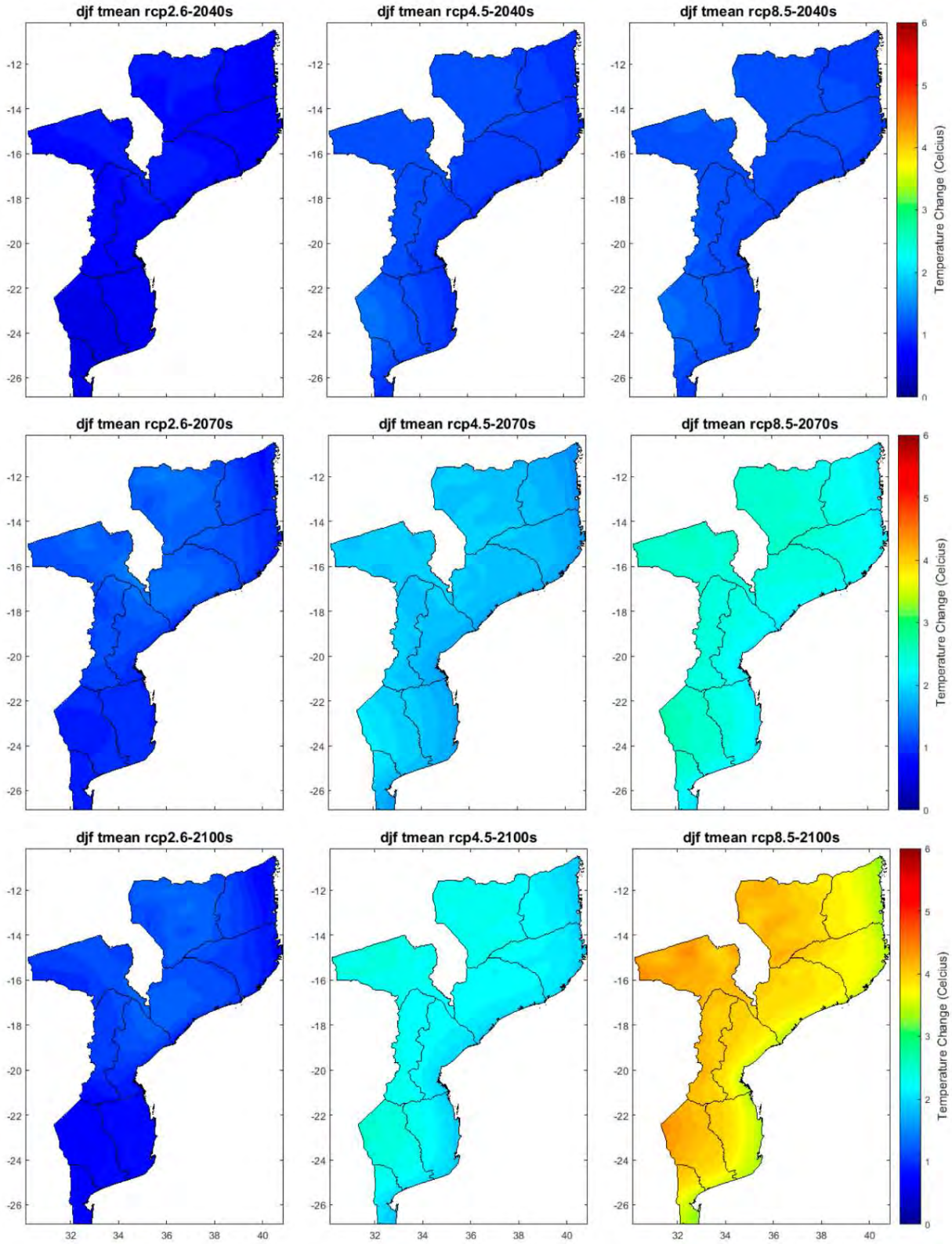

Figure A5. Projected changes of DJF mean temperature for the 2040s (2011–2040), 2070s (2041–2070), and 2100s (2071–2100) with respect to the reference period (1961–1990) for the three RCP emission scenarios (RCP2.6, RCP4.5, and RCP8.5).

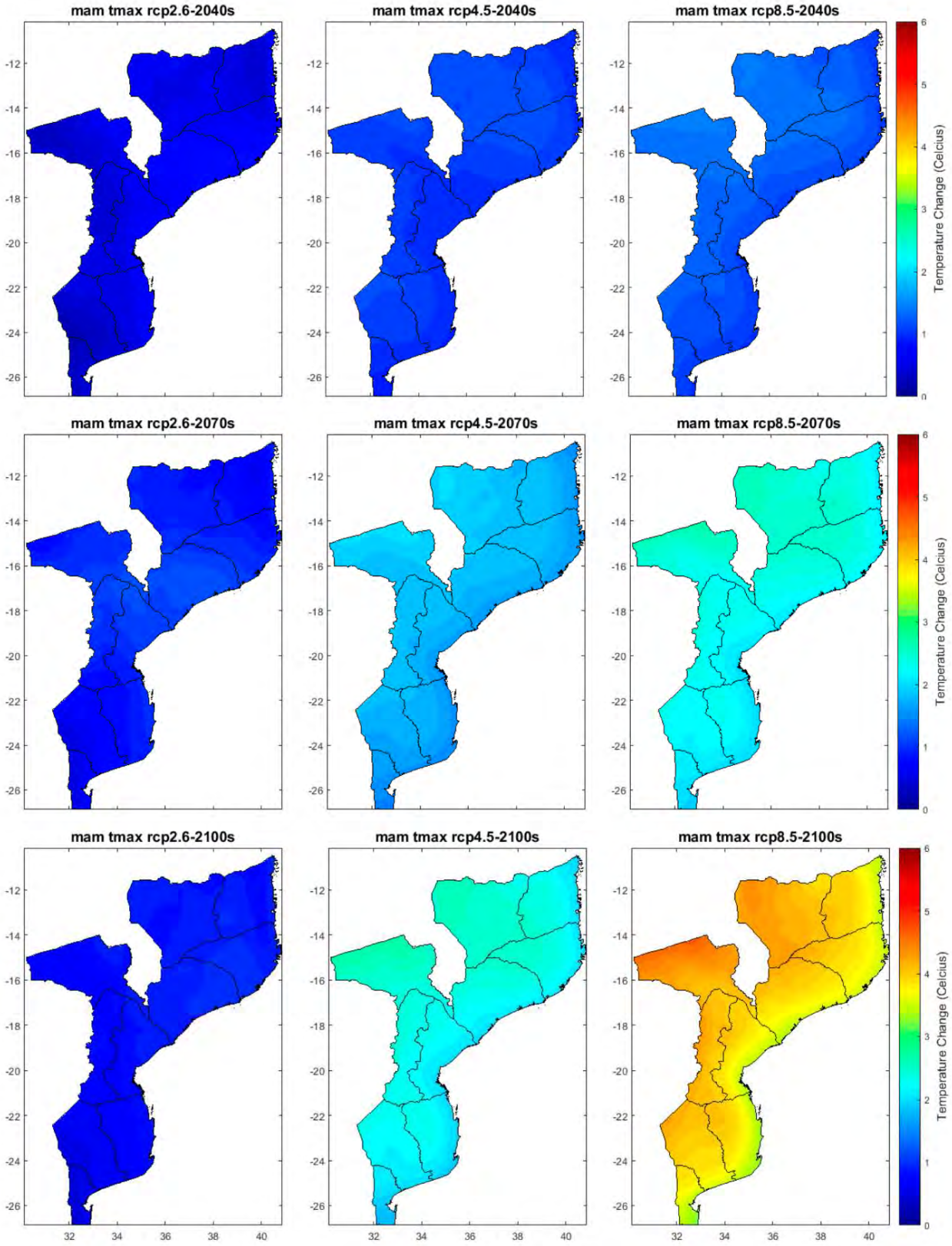

Figure A6. Projected changes of the MAM maximum temperature for the 2040s (2011–2040), 2070s (2041–2070), and 2100s (2071–2100) with respect to the reference period (1961–1990) for the three RCP emission scenarios (RCP2.6, RCP4.5, and RCP8.5).

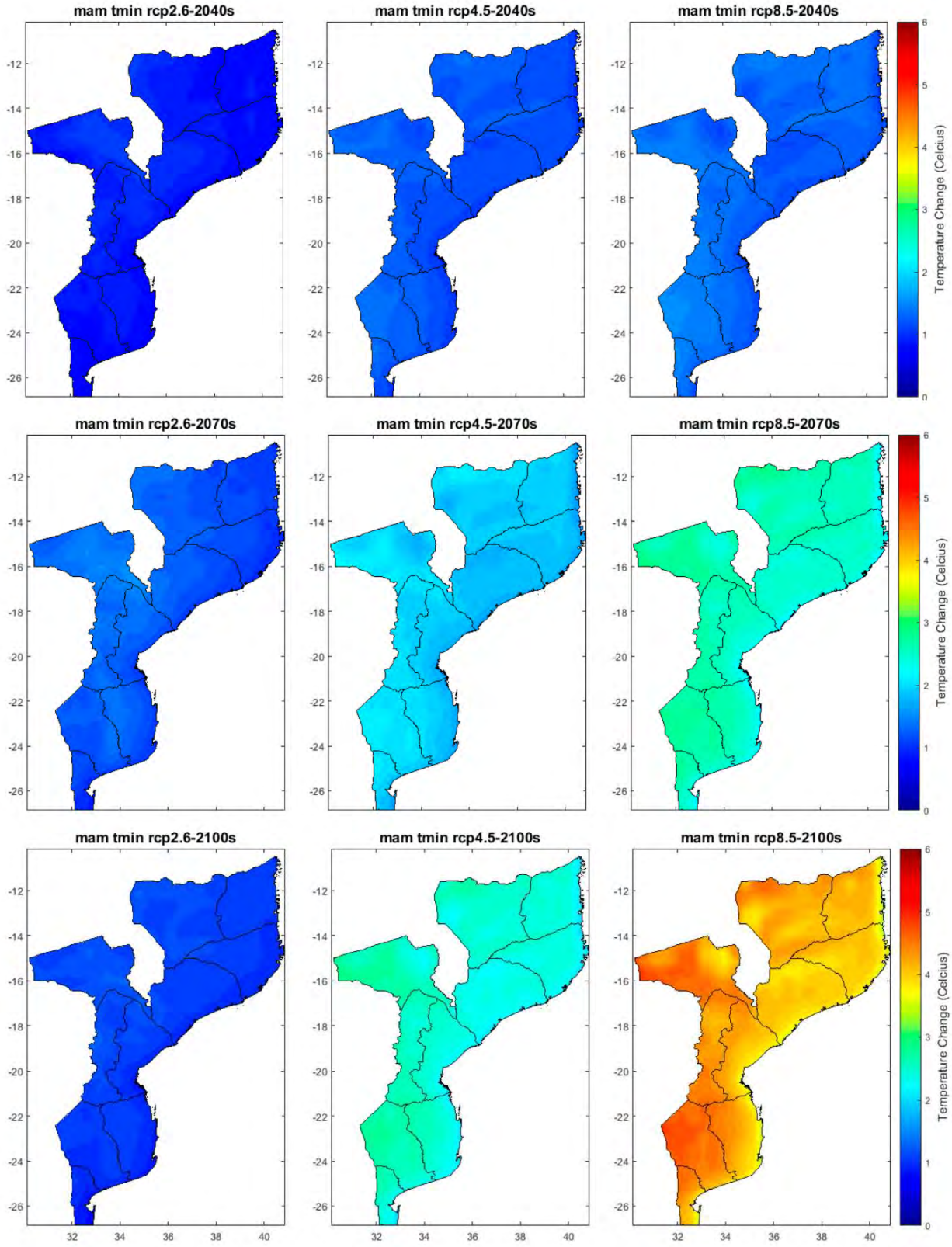

Figure A7. Projected changes of MAM minimum temperature for the 2040s (2011–2040), 2070s (2041–2070), and 2100s (2071–2100) with respect to the reference period (1961–1990) for the three RCP emission scenarios (RCP2.6, RCP4.5, and RCP8.5).

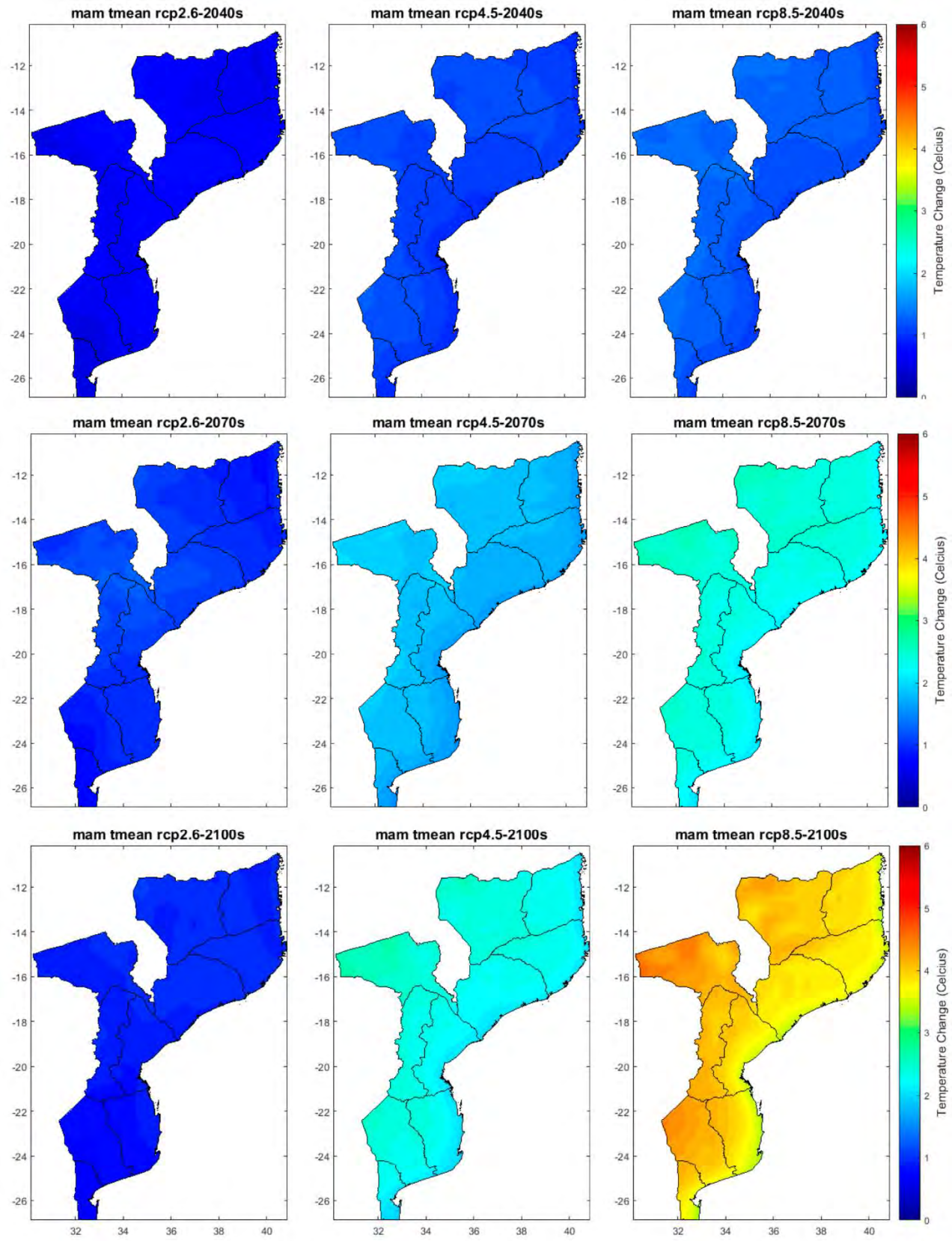

Figure A8. Projected changes of MAM mean temperature for the 2040s (2011–2040), 2070s (2041–2070), and 2100s (2071–2100) with respect to the reference period (1961–1990) for the three RCP emission scenarios (RCP2.6, RCP4.5, and RCP8.5).

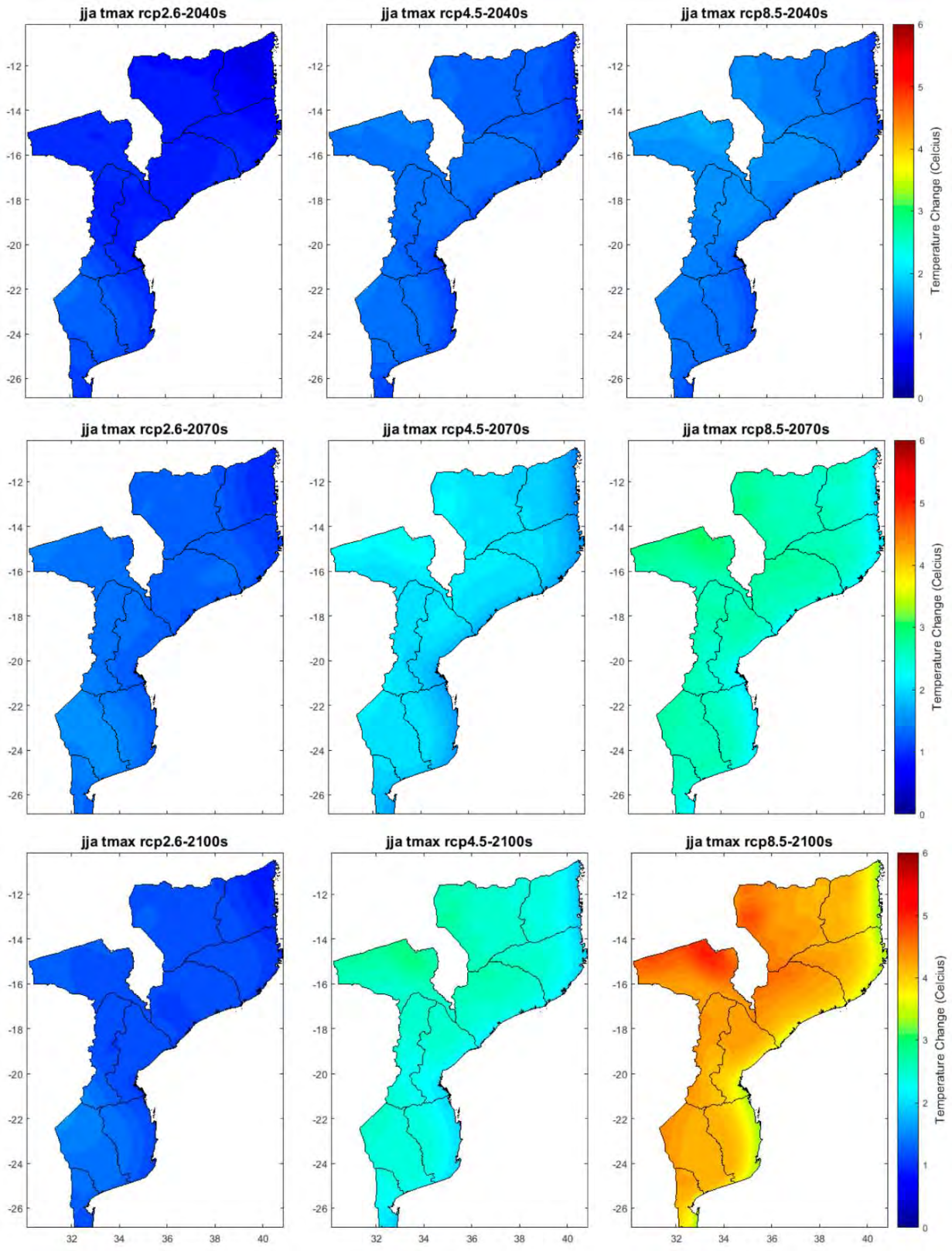

Figure A9. Projected changes of JJA maximum temperature for the 2040s (2011–2040), 2070s (2041–2070), and 2100s (2071–2100) with respect to the reference period (1961–1990) for the three RCP emission scenarios (RCP2.6, RCP4.5, and RCP8.5).

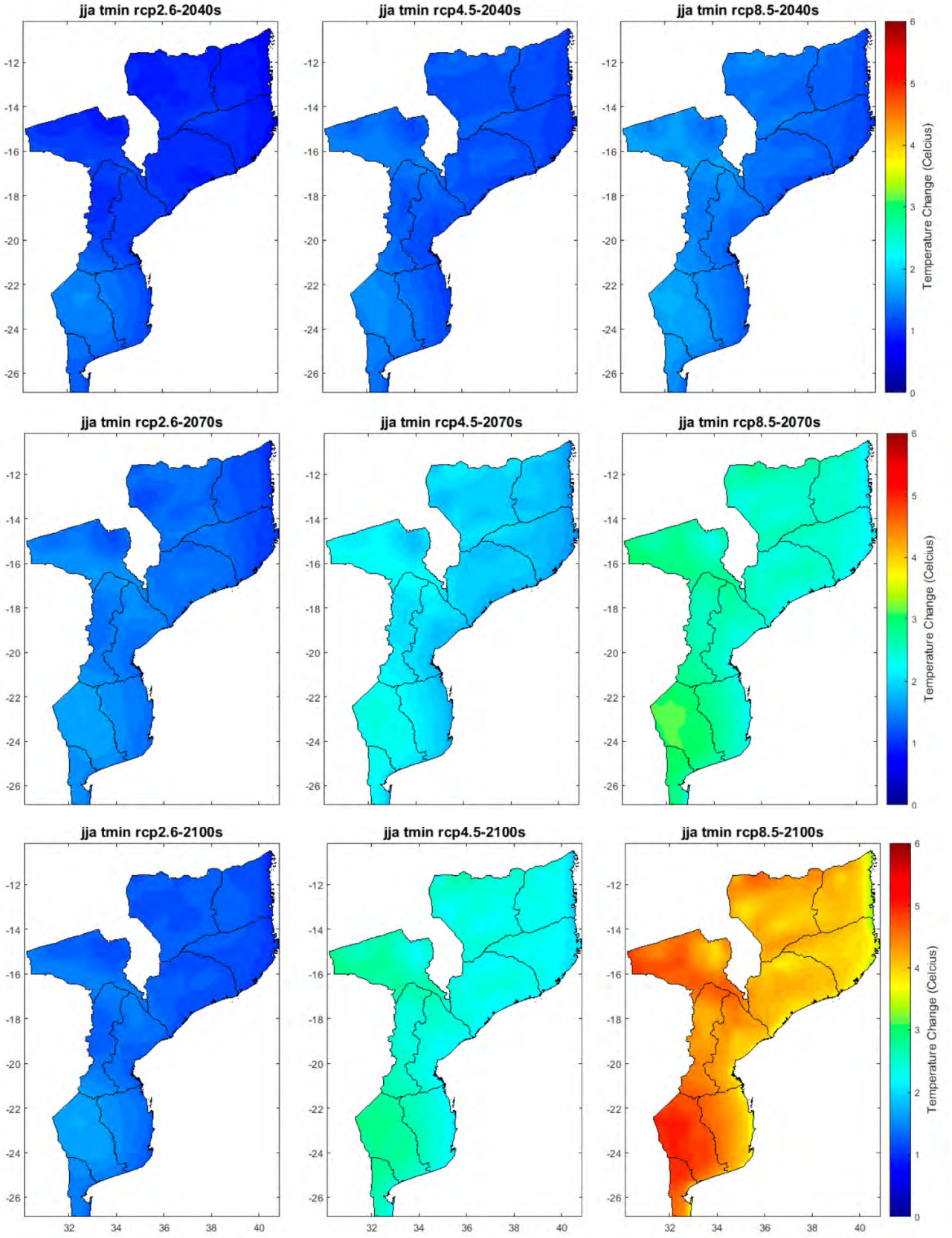

Figure A10. Projected changes of JJA minimum temperature for the 2040s (2011–2040), 2070s (2041–2070), and 2100s (2071–2100) with respect to the reference period (1961–1990) for the three RCP emission scenarios (RCP2.6, RCP4.5, and RCP8.5).

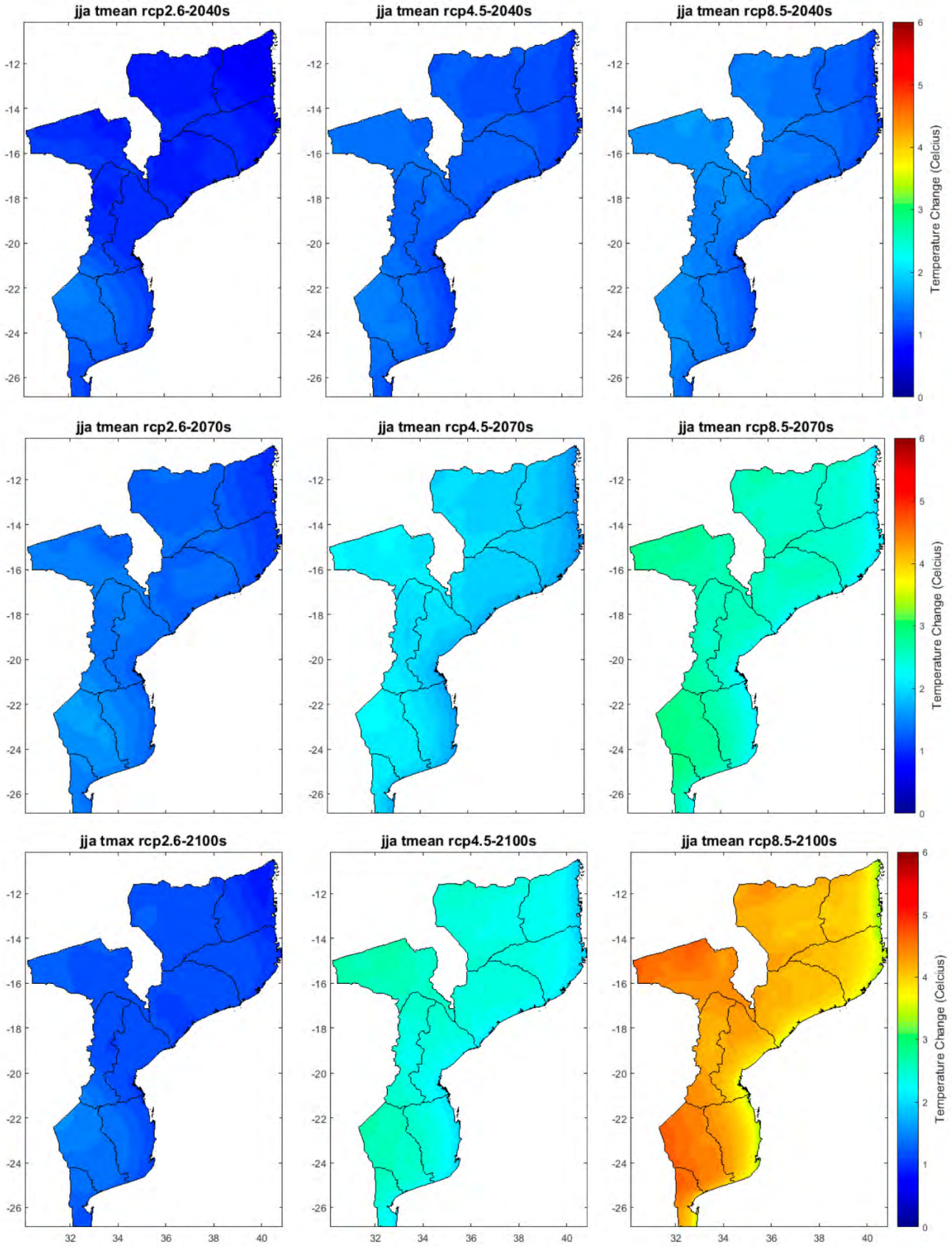

Figure A11. Projected changes of JJA mean temperature for the 2040s (2011–2040), 2070s (2041–2070), and 2100s (2071–2100) with respect to the reference period (1961–1990) for the three RCP emission scenarios (RCP2.6, RCP4.5, and RCP8.5).

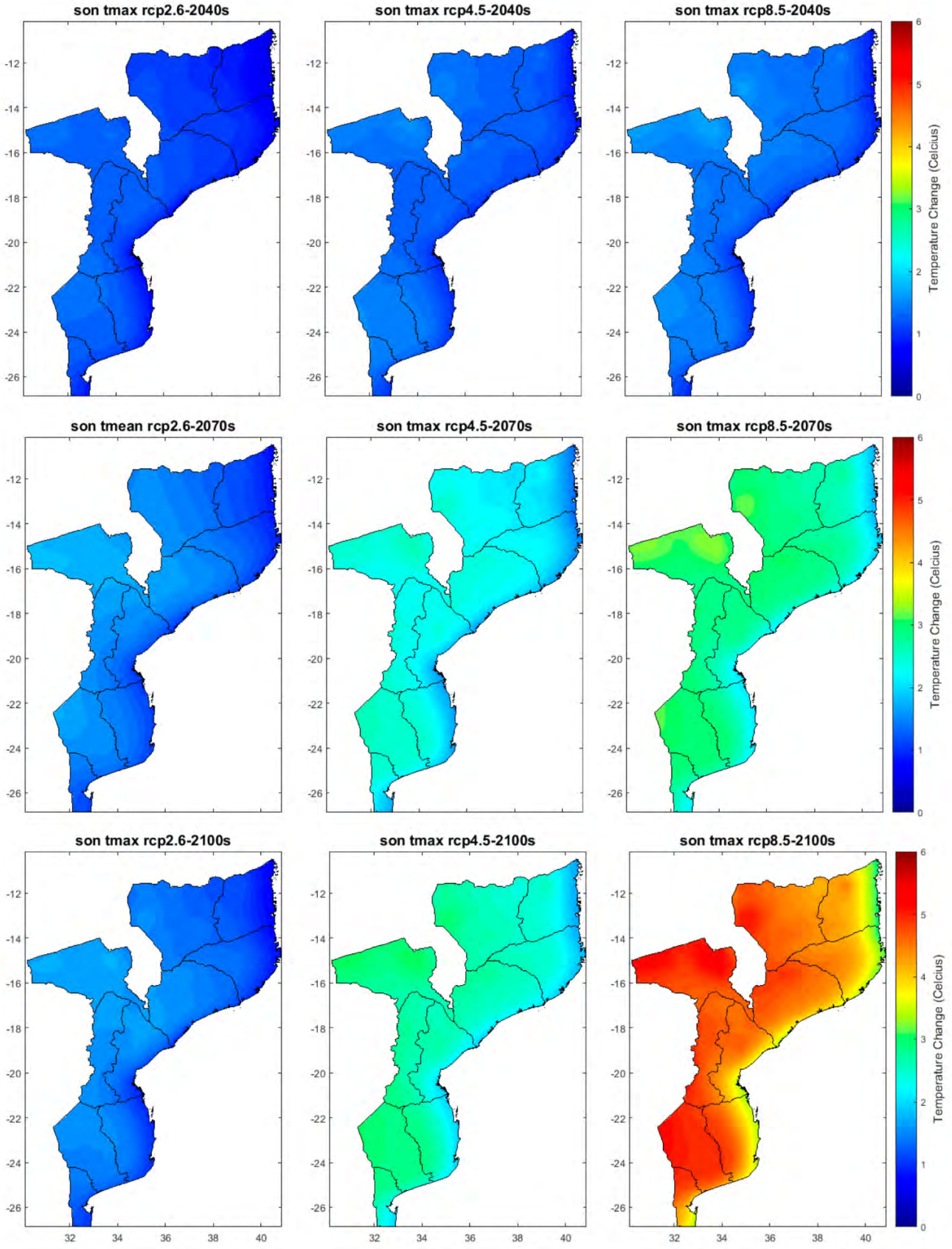

Figure A12. Projected changes of SON maximum temperature for the 2040s (2011–2040), 2070s (2041–2070), and 2100s (2071–2100) with respect to the reference period (1961–1990) for the three RCP emission scenarios (RCP2.6, RCP4.5, and RCP8.5).

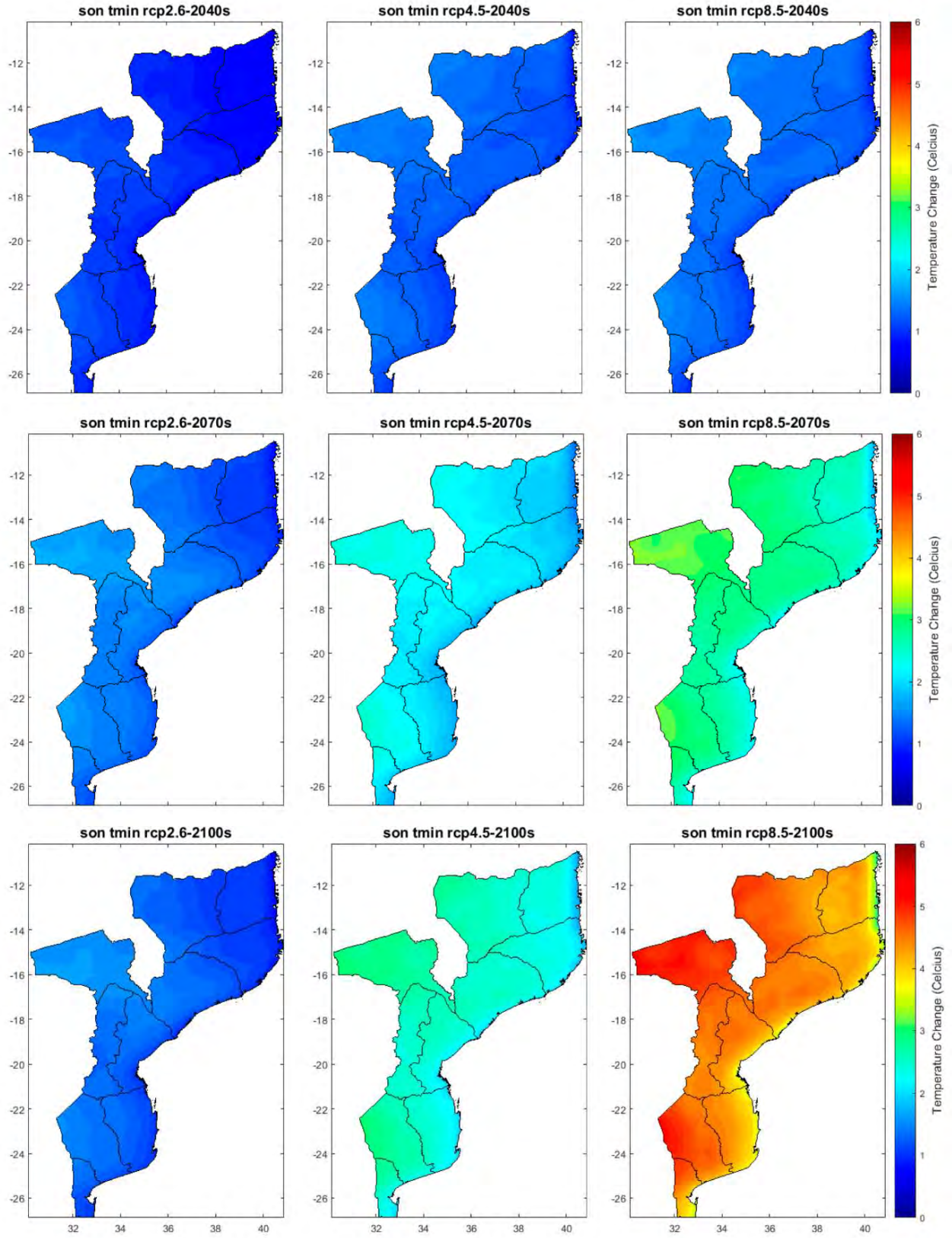

Figure A13. Projected changes of SON minimum temperature for the 2040s (2011–2040), 2070s (2041–2070), and 2100s (2071–2100) with respect to the reference period (1961–1990) for the three RCP emission scenarios (RCP2.6, RCP4.5, and RCP8.5).

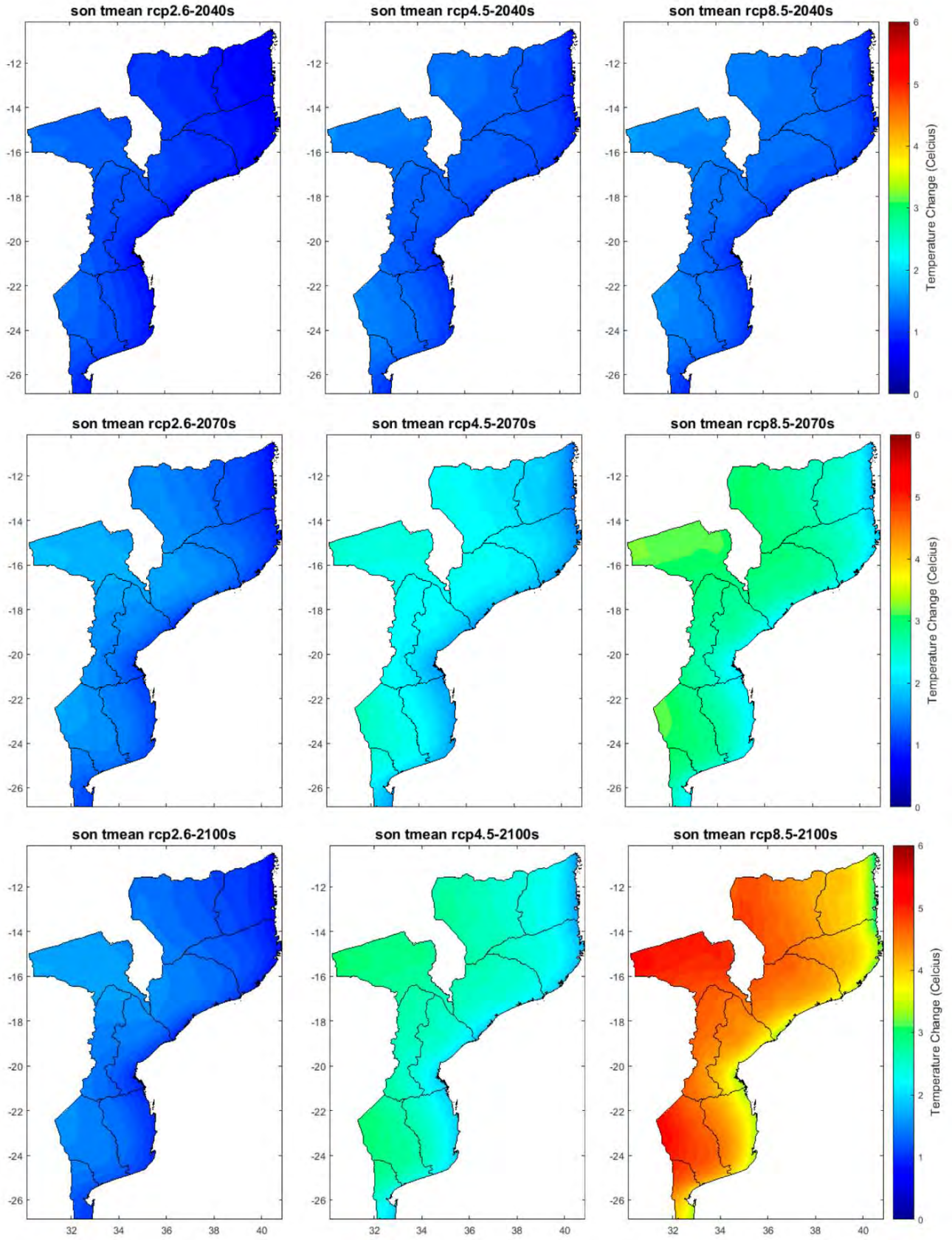

Figure A14. Projected changes of SON mean temperature for the 2040s (2011–2040), 2070s (2041–2070), and 2100s (2071–2100) with respect to the reference period (1961–1990) for the three RCP emission scenarios (RCP2.6, RCP4.5, and RCP8.5).

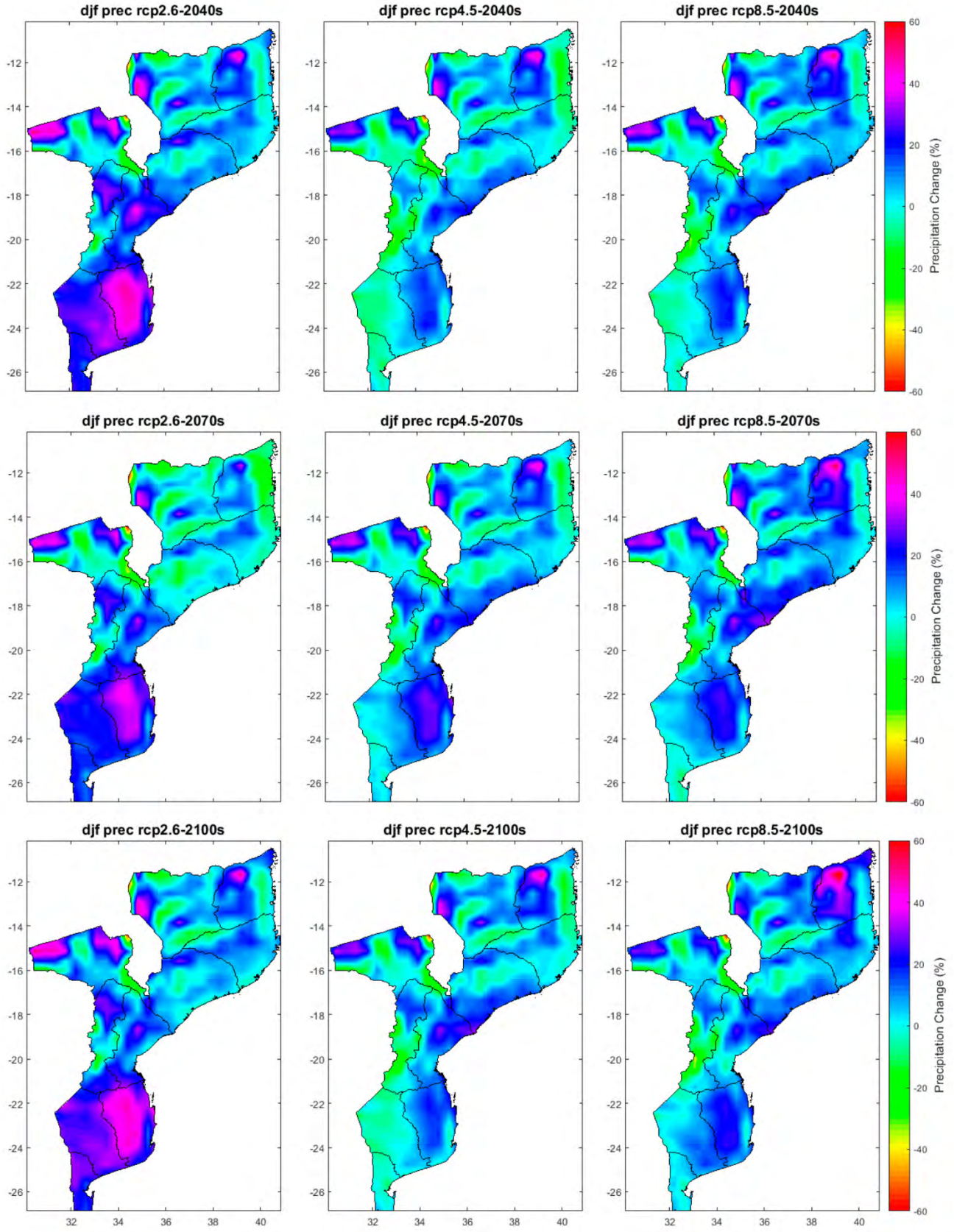

Figure A15. Projected changes of DJF precipitation (%) for the 2040s (2011–2040), 2070s (2041–2070), and 2100s (2071–2100) with respect to the reference period (1961–1990) for the three RCP emission scenarios (RCP2.6, RCP4.5, and RCP8.5).

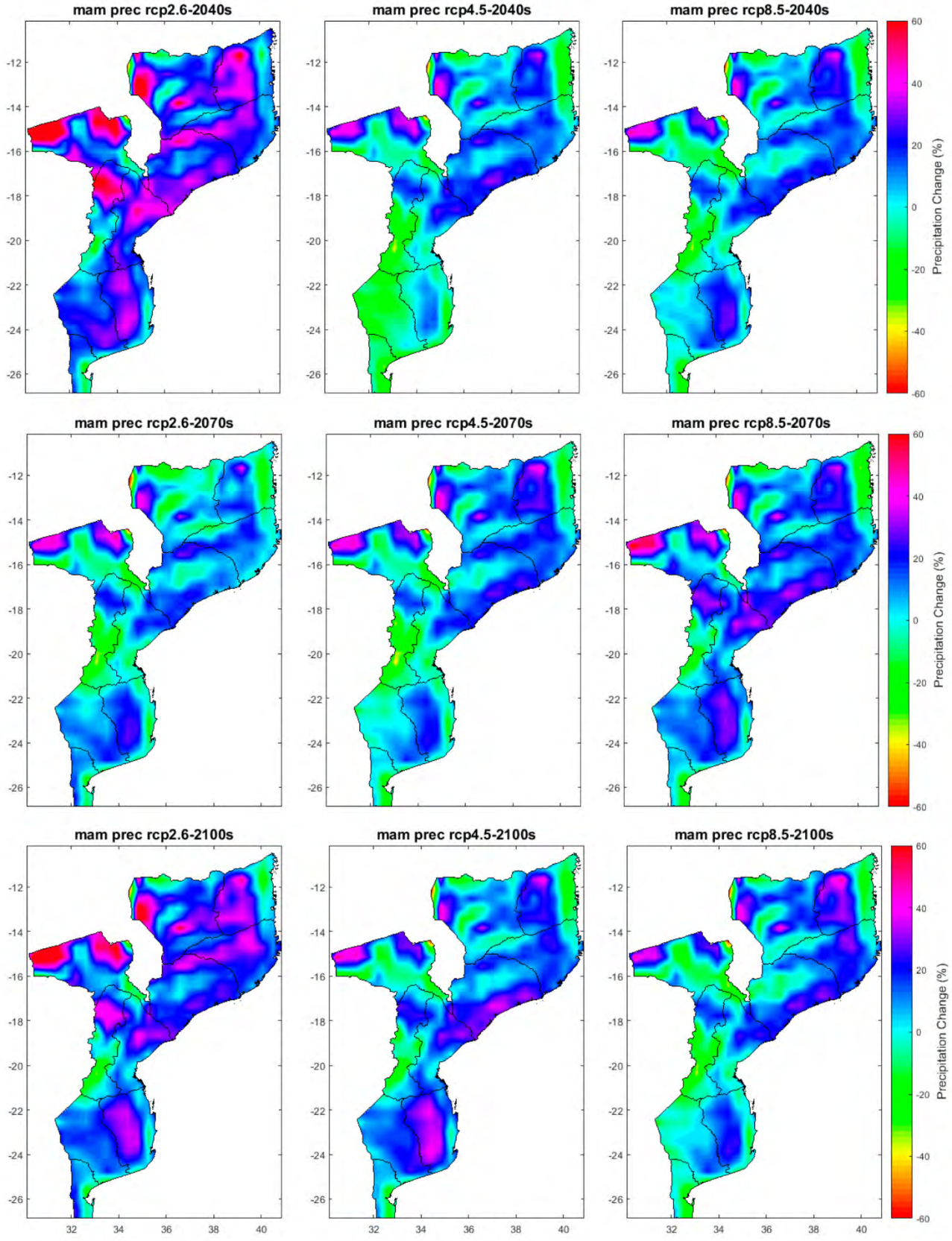

Figure A16. Projected changes of MAM precipitation (%) for the 2040s (2011–2040), 2070s (2041–2070), and 2100s (2071–2100) with respect to the reference period (1961–1990) for the three RCP emission scenarios (RCP2.6, RCP4.5, and RCP8.5).

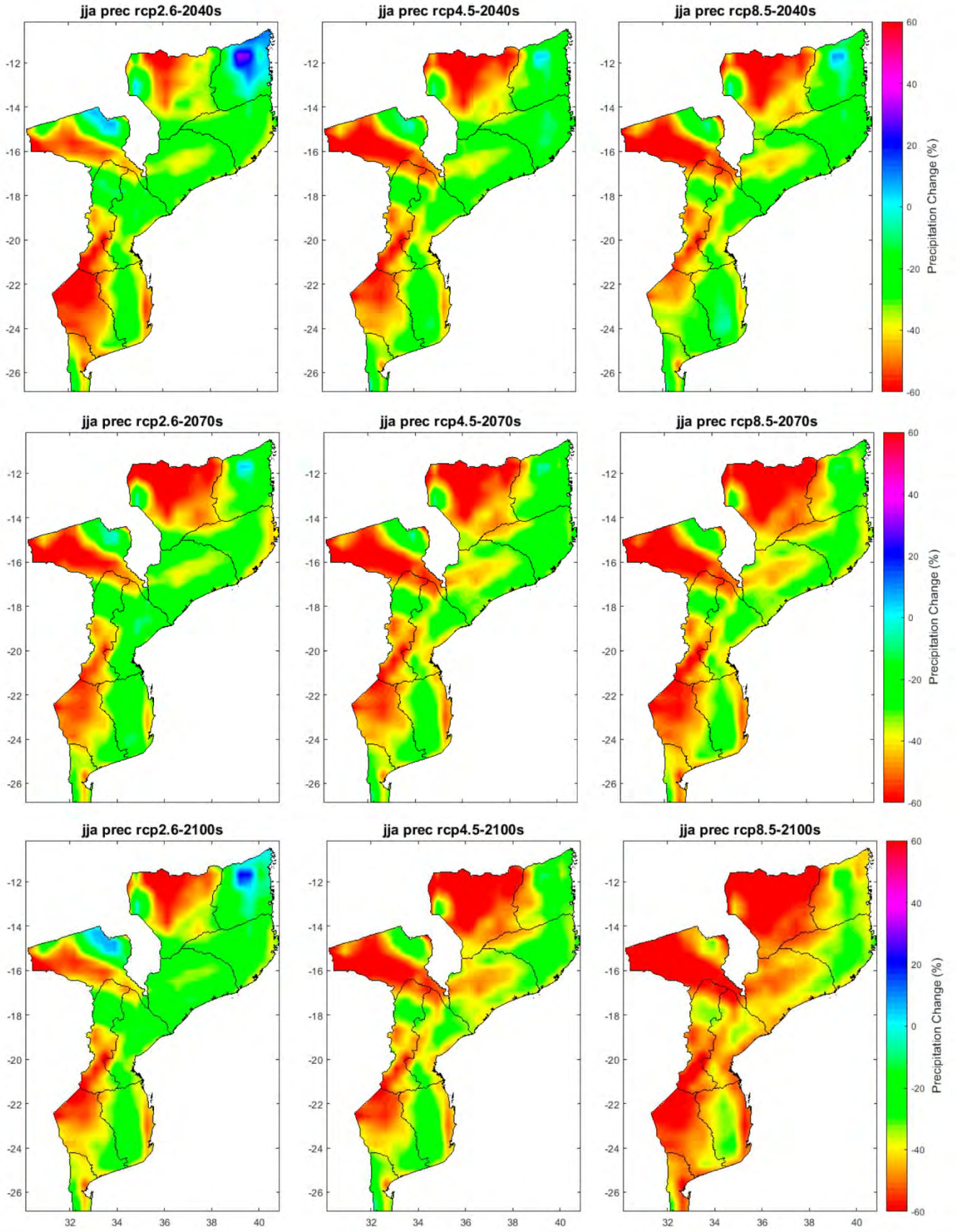

Figure A17. Projected changes of JJA precipitation (%) for the 2040s (2011–2040), 2070s (2041–2070), and 2100s (2071–2100) with respect to the reference period (1961–1990) for the three RCP emission scenarios (RCP2.6, RCP4.5, and RCP8.5).

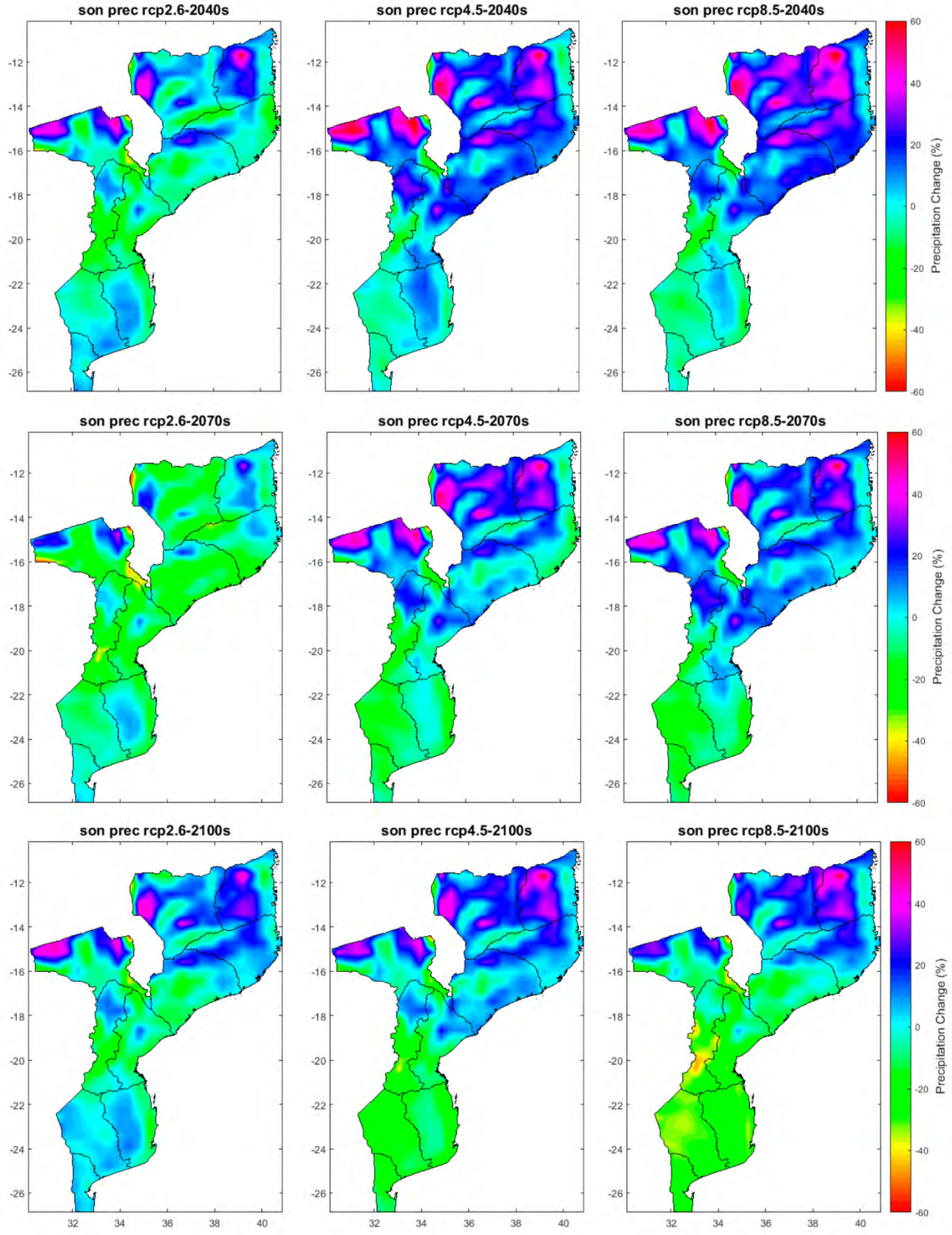

Figure A18. Projected changes of SON precipitation (%) for the 2040s (2011–2040), 2070s (2041–2070), and 2100s (2071–2100) with respect to the reference period (1961–1990) for the three RCP emission scenarios (RCP2.6, RCP4.5, and RCP8.5).

References

1. IPCC. Climate Change 2014: Synthesis Report. In *Contribution of Working Groups I, II and III to the Fifth Assessment Report of the Intergovernmental Panel on Climate Change*; Pachauri, R.K., Meyer, L.A., Eds.; IPCC: Geneva, Switzerland, 2014; p. 151.
2. Boko, M.; Niang, I.; Nyong, A.; Vogel, C.; Githeko, A.; Medany, M.; Osman-Elasha, B.; Tabo, R.; Yanda, P. *Contribution of Working Group II to the Fourth Assessment Report of the Intergovernmental Panel on Climate Change. Climate Change 2007: Impacts, Adaptation and Vulnerability*; Parry, O.F., Canziani, J.P., Palutikof, P.J., van der Linden, Eds.; Cambridge University Press: Cambridge, UK, 2007; pp. 433–467.
3. INGC. *Main Report: INGC Climate Change Report: Study on the Impact of Climate Change on Disaster Risk in Mozambique*; Asante, K., Brundrit, G., Epstein, P., Fernandes, A., Marques, M.R., Mavume, A., Metzger, M., Patt, A., Queface, A., Sanchez del Valle, R., et al., Eds.; INGC: Maputo, Mozambique, 2009.
4. INE. *Statistical Yearbook 2018—Mozambique*; National Statistics Institute: Newport, UK, 2018.
5. World Bank. *Population Grow Rate (Annual %)—Mozambique*; World Bank: Washington, DC, USA, 2019.
6. UN-HABITAT. *The State of African Cities 2014: Re-Imagining Sustainable Urban Transitions*; UN-Habitat: Nairobi, Kenya, 2014.
7. INE. *Statistical Yearbook 2019—Mozambique*; National Statistics Institute: Newport, UK, 2019.
8. Mawren, D.; Hermes, J.; Reason, C.J.C. Exceptional Tropical Cyclone Kenneth in the Far Northern Mozambique Channel and Ocean Eddy Influences. *Geophys. Res. Lett.* **2020**, *47*, e2020GL088715. [CrossRef]
9. PDNA. *Mozambique Cyclone Idai Post Disaster Needs Assessment: Full Report (2019)*; PDNA: Maputo, Mozambique, 2019.
10. WMO. *State of the Climate in Africa 2019*; WHO: Geneva, Switzerland, 2020.
11. Reason, C.J.C. Tropical cyclone Dera, the unusual 2000/01 tropical cyclone season in the South West Indian Ocean and associated rainfall anomalies over Southern Africa. *Theor. Appl. Clim.* **2007**, *97*, 181–188. [CrossRef]
12. Manhique, A.J.; Reason, C.J.C.; Silinto, B.; Zucula, J.; Raiva, I.; Congolo, F.; Mavume, A.F. Extreme rainfall and floods in southern Africa in January 2013 and associated circulation patterns. *Nat. Hazards* **2015**, *77*, 679–691. [CrossRef]
13. Rouault, M.; Richard, Y. Intensity and spatial extent of droughts in southern Africa. *Geophys. Res. Lett.* **2005**, *32*. [CrossRef]
14. New, M.; Hewitson, B.; Stephenson, D.B.; Tsiga, A.; Kruger, A.; Manhique, A.; Gomez, B.; Coelho, C.A.S.; Masisi, D.N.; Kululanga, E.; et al. Evidence of trends in daily climate extremes over southern and west Africa. *J. Geophys. Res. Space Phys.* **2006**, *111*, 111. [CrossRef]
15. Ceccherini, G.; Russo, S.; Ameztoy, I.; Marchese, A.F.; Carmona-Moreno, C. Heat waves in Africa 1981–2015, observations and reanalysis. *Nat. Hazards Earth Syst. Sci.* **2017**, *17*, 115–125. [CrossRef]
16. Nkemelang, T.; New, M.; Zaroug, M.A.H. Temperature and precipitation extremes under current, 1.5 °C and 2.0 °C global warming above pre-industrial levels over Botswana, and implications for climate change vulnerability. *Environ. Res. Lett.* **2018**, *13*, 065016. [CrossRef]
17. Davis-Reddy, C.L.; Vincent, K. *Climate Risk and Vulnerability: A Handbook for Southern Africa*, 2nd ed.; Council for Scientific and Industrial Research: Pretoria, South Africa, 2017.
18. Muthige, M.S.; Malherbe, J.; A Englebrecht, F.; Grab, S.; Beraki, A.; Maisha, T.R.; Van Der Merwe, J.; A Engelbrecht, F. Projected changes in tropical cyclones over the South West Indian Ocean under different extents of global warming. *Environ. Res. Lett.* **2018**, *13*, 065019. [CrossRef]
19. UNFCC. *Paris Agreement*; UNFCC: Bonn, Germany, 2015.
20. IPCC. 2018: Summary for Policymakers. In *Global warming of 1.5 °C. An IPCC Special Report on the Impacts of Global Warming of 1.5°C above Pre-Industrial Levels and Related Global Greenhouse Gas Emission Pathways, in the Context of Strengthening the Global Response to the Threat of Climate Change, Sustainable Development, and Efforts to Eradicate Poverty*; Masson-Delmotte, V., Zhai, P., Pörtner, H.O., Roberts, D., Skea, J., Shukla, P.R., Pirani, A., Moufouma-Okia, W., Péan, C., Pidcock, R., et al., Eds.; World Meteorological Organization: Geneva, Switzerland, 2018.
21. Kompas, T.; Pham, V.H.; Che, T.N. The Effects of Climate Change on GDP by Country and the Global Economic Gains From Complying With the Paris Climate Accord. *Earth's Futur.* **2018**, *6*, 1153–1173. [CrossRef]
22. Rogelj, J.; Elzen, M.D.; Höhne, N.; Fransen, T.; Fekete, H.; Winkler, H.; Schaeffer, R.; Sha, F.; Riahi, K.; Meinshausen, M. Paris Agreement climate proposals need a boost to keep warming well below 2 °C. *Nat. Cell Biol.* **2016**, *534*, 631–639. [CrossRef]
23. UNEP. *UN Environment, Emissions Gap Report 2019 (Nairobi: UN Environment, 2019)*; UNEP: Nairobi, Kenya, 2019.
24. INDC. *Intended Nationally Determined Contribution (INDC) of Mozambique to the United Nations Framework Convention on Climate Change (UNFCCC)*; UNFCCC: Rio de Janeiro, Brazil, 2015.
25. Nikulin, G.; Lennard, C.; Dosio, A.; Kjellström, E.; Chen, Y.; Hänsler, A.; Kupiainen, M.; Laprise, R.; Mariotti, L.; Maule, C.F.; et al. The effects of 1.5 and 2 degrees of global warming on Africa in the CORDEX ensemble. *Environ. Res. Lett.* **2018**, *13*, 065003. [CrossRef]
26. Fischer, E.M.; Knutti, R. Anthropogenic contribution to global occurrence of heavy-precipitation and high-temperature extremes. *Nat. Clim. Chang.* **2015**, *5*, 560–564. [CrossRef]
27. Marques, M.R. Impacts of Climate Change and socio economic developments on Land Use and Land Cover-Potential effects on crop yields. In *INGC. (2009). Main Report: INGC Climate Change Report: Study on the Impact of Climate Change on Disaster Risk in Mozambique*; Asante, K., Brundrit, G., Epstein, P., Fernandes, A., Marques, M.R., Mavume, A., Metzger, M., Patt, A., Queface, A., Sanchez del Valle, R., et al., Eds.; INGC: Maputo, Mozambique, 2009.

28. Assante, K.; Vilankulos, A. Future impacts of climate change on river flow, floods, saline intrusion. In *INGC. (2009). Main Report: INGC Climate Change Report: Study on the Impact of Climate Change on Disaster Risk in Mozambique*; Asante, K., Brundrit, G., Epstein, P., Fernandes, A., Marques, M.R., Mavume, A., Metzger, M., Patt, A., Queface, A., Sanchez del Valle, R., et al., Eds.; INGC: Maputo, Mozambique, 2009.
29. Engelbrecht, F.; Adegoke, J.; Bopape, M.-J.; Naidoo, M.; Garland, R.; Thatcher, M.; McGregor, J.; Katzfey, J.; Werner, M.; Ichoku, C.; et al. Projections of rapidly rising surface temperatures over Africa under low mitigation. *Environ. Res. Lett.* **2015**, *10*, 085004. [CrossRef]
30. Dosio, A. Projection of temperature and heat waves for Africa with an ensemble of CORDEX Regional Climate Models. *Clim. Dyn.* **2017**, *49*, 493–519. [CrossRef]
31. Maure, G.A.; Pinto, I.; Ndebele-Murisa, M.R.; Muthige, M.; Lennard, C.; Nikulin, G.; Dosio, A.; Meque, A.O. The southern African climate under 1.5 °C and 2 °C of global warming as simulated by CORDEX regional climate models. *Environ. Res. Lett.* **2018**, *13*, 065002. [CrossRef]
32. Kling, H.; Stanzel, P.; Preishuber, M. Impact modelling of water resources development and climate scenarios on Zambezi River discharge. *J. Hydrol. Reg. Stud.* **2014**, *1*, 17–43. [CrossRef]
33. Uamusse, M.M.; Tussupova, K.; Persson, K.M. Climate Change Effects on Hydropower in Mozambique. *Appl. Sci.* **2020**, *10*, 4842. [CrossRef]
34. Epstein, P. Preliminary health analysis. In *Main Report: INGC Climate Change Report: Study on the Impact of Climate Change on Disaster Risk in Mozambique*; Asante, K., Brundrit, G., Epstein, P., Fernandes, A., Marques, M.R., Mavume, A., Metzger, M., Patt, A., Queface, A., Sanchez del Valle, R., et al., Eds.; INGC: Maputo, Mozambique, 2009.
35. Salau, O.R.; Adeleye, O.A.; Adeleye, F.A.; Américo, F. The Links between Climate and Malaria Disease in Ekiti State, Nigeria. *Intern. J. Prev. Med. Res.* **2018**, *4*, 60–67.
36. WHO. Cholera in 1997. *Week. Epidem. Rec.* **1998**, *73*, 201–208.
37. Bateman, C. Mozambique cholera will affect region. *S. Afr. Med. J.* **2002**, *92*, 104–106.
38. Gudo, E.S.; Pinto, G.; Weyer, J.; Le Roux, C.; Mandlaze, A.; José, A.F.; Muianga, A.; Paweska, J.T. Serological evidence of rift valley fever virus among acute febrile patients in Southern Mozambique during and after the 2013 heavy rainfall and flooding: Implication for the management of febrile illness. *Virol. J.* **2016**, *13*, 96. [CrossRef] [PubMed]
39. WHO. *Fact Sheet: World Malaria Report 2016*; World Health Organization: Geneva, Switzerland, 2016.
40. Colborn, K.L.; Giorgi, E.; Monaghan, A.J.; Gudo, E.; Candrinho, B.; Marrufo, T.J.; Colborn, J.M. Spatio-temporal modelling of weekly malaria incidence in children under 5 for early epidemic detection in Mozambique. *Sci. Rep.* **2018**, *8*, 9238. [CrossRef]
41. Tadross, M. Climate Change modelling and future analysis. In *INGC. (2009). Main report: INGC Climate Change Report: Study on the Impact of Climate Change on Disaster Risk in Mozambique*; Asante, K., Brundrit, G., Epstein, P., Fernandes, A., Marques, M.R., Mavume, A., Metzger, M., Patt, A., Queface, A., Sanchez del Valle, R., et al., Eds.; INGC: Maputo, Mozambique, 2009.
42. Hunter, R.; Afonso, F.; Mavume, A.; New, M. *Problems and Solutions for Climate Change Resilience and Adaptation in Mozambique: State of Adaptation Knowledge, Policies and Practices to support Conservation Agriculture*; Universidade Eduardo Mondlane: Maputo, Mozambique, 2011.
43. Hayhoe, K.; Edmonds, J.; Kopp, R.E.; Le Grande, A.N.; Sanderson, B.M.; Wehner, M.F.; Wuebbles, D.J. Climate models, scenarios, and projections. In *Climate Science Special Report: Fourth National Climate Assessment*; U.S. Global Change Research Program: Washington, DC, USA, 2017; Volume I, pp. 1–470.
44. Luhunga, P.M.; Kijazi, A.L.; Chang'A, L.; Kondowe, A.; Ng'Ongolo, H.; Mtongori, H. Climate Change Projections for Tanzania Based on High-Resolution Regional Climate Models From the Coordinated Regional Climate Downscaling Experiment (CORDEX)-Africa. *Front. Environ. Sci.* **2018**, *6*, 6. [CrossRef]
45. Pinto, I.; Jack, C.; Hewitson, B. Process-based model evaluation and projections over southern Africa from Coordinated Regional Climate Downscaling Experiment and Coupled Model Intercomparison Project Phase 5 models. *Int. J. Clim.* **2018**, *38*, 4251–4261. [CrossRef]
46. Zittis, G.; Hadjinicolaou, P.; Klangidou, M.; Proestos, Y.; Lelieveld, J. A multi-model, multi-scenario, and multi-domain analysis of regional climate projections for the Mediterranean. *Reg. Environ. Chang.* **2019**, *19*, 2621–2635. [CrossRef]
47. Gebrechorkos, S.H.; Hülsmann, S.; Bernhofer, C. Statistically downscaled climate dataset for East Africa. *Sci. Data* **2019**, *6*, 1–8. [CrossRef] [PubMed]
48. Hewitson, B.; Crane, R. Climate downscaling: Techniques and application. *Clim. Res.* **1996**, *7*, 85–95. [CrossRef]
49. Giorgi, F.; Gutowski, W.J. Regional Dynamical Downscaling and the CORDEX Initiative. *Annu. Rev. Environ. Resour.* **2015**, *40*, 467–490. [CrossRef]
50. Liang, X.-Z.; Kunkel, K.E.; Meehl, G.A.; Jones, R.G.; Wang, J.X.L. Regional climate models downscaling analysis of general circulation models present climate biases propagation into future change projections. *Geophys. Res. Lett.* **2008**, *35*, 1–5. [CrossRef]
51. Giorgi, F.; Jones, C.; Asrar, G. Addressing Climate Information Needs at the Regional Level: The CORDEX Framework. *World Meteor. Organiz. Bull.* **2009**, *58*, 175–183. Available online: http://wcrp.ipsl.jussieu.fr/RCD_Projects/CORDEX/CORDEX_giorgi_WMO.pdf (accessed on 12 March 2020).
52. Buontempo, C.; Mathison, C.; Jones, R.; Williams, K.; Wang, C.; McSweeney, C. An ensemble climate projection for Africa. *Clim. Dyn.* **2014**, *44*, 2097–2118. [CrossRef]

53. Gebrechorkos, S.H.; Hülsmann, S.; Bernhofer, C. Regional climate projections for impact assessment studies in East Africa. *Environ. Res. Lett.* **2019**, *14*, 044031. [CrossRef]
54. Klutse, N.A.B.; Ajayi, V.O.; Gbobaniyi, E.; Egbebiyi, T.S.; Kouadio, K.; Nkrumah, F.; Quagraine, K.A.; Olusegun, C.; Diasso, U.; Abiodun, B.J.; et al. Potential impact of 1.5 °C and 2 °C global warming on consecutive dry and wet days over West Africa. *Environ. Res. Lett.* **2018**, *13*, 055013. [CrossRef]
55. Dosio, A.; Turner, A.G.; Tamoffo, A.T.; Sylla, M.B.; Lennard, C.; Jones, R.G.; Terray, L.; Nikulin, G.; Hewitson, B. A tale of two futures: Contrasting scenarios of future precipitation for West Africa from an ensemble of regional climate models. *Environ. Res. Lett.* **2020**, *15*, 064007. [CrossRef]
56. Pinto, I.; Lennard, C.; Tadross, M.; Hewitson, B.; Dosio, A.; Nikulin, G.; Panitz, H.-J.; Shongwe, M.E. Evaluation and projections of extreme precipitation over southern Africa from two CORDEX models. *Clim. Chang.* **2015**, *135*, 655–668. [CrossRef]
57. Lennard, C.; Nikulin, G.; Dosio, A.; Moufouma-Okia, W. On the need for regional climate information over Africa under varying levels of global warming. *Environ. Res. Lett.* **2018**. [CrossRef]
58. Osima, S.; Indasi, V.S.; Zaroug, M.; Endris, H.S.; Gudoshava, M.; Misiani, H.O.; Nimusiima, A.; Anyah, R.O.; Otieno, G.; Ogwang, B.A.; et al. Projected climate over the Greater Horn of Africa under 1.5 °C and 2 °C global warming. *Environ. Res. Lett.* **2018**, *13*, 065004. [CrossRef]
59. Tamoffo, A.T.; Dosio, A.; Vondou, D.A.; Sonkoué, D. Process-Based Analysis of the Added Value of Dynamical Downscaling Over Central Africa. *Geophys. Res. Lett.* **2020**, *47*. [CrossRef]
60. Luhunga, P.; Botai, J.; Kahimba, F. Evaluation of the performance of CORDEX regional climate models in simulating present climate conditions of Tanzania. *J. South. Hemisph. Earth Syst. Sci.* **2016**, *66*, 32–54. [CrossRef]
61. Sibanda, S.; Grab, S.W.; Ahmed, F. An evaluation of the CORDEX regional climate models in simulating future rainfall and extreme events over Mzingwane catchment, Zimbabwe. *Theor. Appl. Clim.* **2019**, *140*, 91–100. [CrossRef]
62. Van Logchem, B.; Queface, A.J. *Responding to Climate Change in Mozambique: Synthesis Report*; INGC: Maputo, Mozambique, 2012.
63. Bousquet, O.; Barruol, G.; Cordier, E.; Barthe, C.; Bielli, S.; Calmer, R.; Rindraharisaona, E.; Roberts, G.; Tulet, P.; Amelie, V.; et al. Impact of Tropical Cyclones on Inhabited Areas of the SWIO Basin at Present and Future Horizons. Part 1: Overview and Observing Component of the Research Project RENOVRISKCYCLONE. *Atmosphere* **2021**, *12*, 544. [CrossRef]
64. Van Vuuren, D.P.; Stehfest, E.; Elzen, M.G.J.D.; Kram, T.; Van Vliet, J.; Deetman, S.; Isaac, M.; Goldewijk, K.K.; Hof, A.; Beltran, A.M.; et al. RCP2.6: Exploring the possibility to keep global mean temperature increase below 2 °C. *Clim. Chang.* **2011**, *109*, 95–116. [CrossRef]
65. van Vuuren, D.P.; Carter, T.R. Climate and socio-economic scenarios for climate change research and assessment: Reconciling the new with the old. *Clim. Chang.* **2014**, *122*, 415–429. [CrossRef]
66. Nakicenovic, N.; Swart, R. *Special Report on Emissions Scenarios: A Special Report of Working Group III of the Intergovernmental Panel on Climate Change*; Cambridge University Press: Cambridge, UK, 2000; p. 599.
67. Manhique, A. The South Indian Convergence Zone and Relationship with Rainfall Variability in Mozambique. Ph.D. Thesis, University of Cape Town, Western Cape, South Africa, 2008.
68. Usman, M.; Reason, C. Dry spell frequencies and their variability over southern Africa. *Clim. Res.* **2004**, *26*, 199–211. [CrossRef]
69. Lindesay, J.A.; Vogel, C.H. Historical evidence for Southern Oscillation-southern African rainfall relationships. *Int. J. Clim.* **1990**, *10*, 679–689. [CrossRef]
70. Rocha, A.; Simmonds, I.A.N. Interannual variability of south-eastern African summer rainfall. Part 1: Relationships with air-sea interactions processes. *Int. J. Climatol.* **1997**, *17*, 235–265. [CrossRef]
71. Tyson, P.D.; Preston-Whyte, R.A. *The Weather and Climate of Southern Africa*; Oxford University Press: Oxford, UK, 2000; p. 396.
72. Reason, C.J.C.; Landman, W.; Tennant, W. Seasonal to Decadal Prediction of Southern African Climate and Its Links with Variability of the Atlantic Ocean. *Bull. Am. Meteorol. Soc.* **2006**, *87*, 941–956. [CrossRef]
73. Edossa, D.C.; Woyessa, Y.E.; Welderufael, W.A. Analysis of Droughts in the Central Region of South Africa and Their Association with SST Anomalies. *Int. J. Atmos. Sci.* **2014**, *2014*, 1–8. [CrossRef]
74. Reason, C.J.C.; Keibel, A. Tropical Cyclone Eline and its unusual penetration and impacts over the southern Africa mainland. *Weather Forecast.* **2004**, *19*, 789–805. [CrossRef]
75. Mavume, A.F.; Rydberg, L.; Rouault, M.; Lutjeharms, J.R.E. Climatology of Tropical Cyclones in the South-West Indian Ocean; landfall in Mozambique and Madagascar. *West. Indian Ocean J. Mar. Sci.* **2009**, *8*, 15–36.
76. Leroux, M.-D.; Meister, J.; Mekies, D.; Dorla, A.-L.; Caroff, P. A Climatology of Southwest Indian Ocean Tropical Systems: Their Number, Tracks, Impacts, Sizes, Empirical Maximum Potential Intensity, and Intensity Changes. *J. Appl. Meteorol. Clim.* **2018**, *57*, 1021–1041. [CrossRef]
77. Freitas, E.D.; Rozoff, C.M.; Cotton, W.R.; Dias, P.L.S. Interactions of an urban heat island and sea-breeze circulations during winter over the metropolitan area of São Paulo, Brazil. *Bound.-Layer Meteorol.* **2006**, *122*, 43–65. [CrossRef]
78. Jones, C.G.; Wyser, K.; Ullerstig, A.; Willén, U. The Rossby Centre Regional Atmospheric Climate Model Part II: Application to the Arctic Climate. *AMBIO A J. Hum. Environ.* **2004**, *33*, 211–220. [CrossRef]
79. Samuelsson, P.; Jones, C.G.; Will´ En, U.; Ullerstig, A.; Gollvik, S.; Hansson, U.; Jansson, C.; Kjellström, C.; Nikulin, G.; Wyser, K. The Rossby Centre Regional Climate model RCA3: Model description and performance. *Tellus A Dyn. Meteorol. Oceanogr.* **2011**, *63*, 4–23. [CrossRef]

80. Collazo, S.; Lhotka, O.; Rusticucci, M.; Kyselý, J. Capability of the SMHI-RCA4 RCM driven by the ERA-Interim reanalysis to simulate heat waves in Argentina. *Int. J. Clim.* **2017**, *38*, 483–496. [CrossRef]
81. Wu, M.; Nikulin, G.; Kjellström, E.; Belušić, D.; Jones, C.; Lindstedt, D. The impact of regional climate model formulation and resolution on simulated precipitation in Africa. *Earth Syst. Dyn.* **2020**, *11*, 377–394. [CrossRef]
82. Kalognomou, E.-A.; Lennard, C.; Shongwe, M.; Pinto, I.; Favre, A.; Kent, M.; Hewitson, B.; Dosio, A.; Nikulin, G.; Panitz, H.-J.; et al. A Diagnostic Evaluation of Precipitation in CORDEX Models over Southern Africa. *J. Clim.* **2013**, *26*, 9477–9506. [CrossRef]
83. Switanek, M.B.; Troch, P.A.; Castro, C.L.; Leuprecht, A.; Chang, H.-I.; Mukherjee, R.; DeMaria, E.M.C. Scaled distribution mapping: A bias correction method that preserves raw climate model projected changes. *Hydrol. Earth Syst. Sci.* **2017**, *21*, 2649–2666. [CrossRef]
84. Wilcke, R.A.I.; Mendlik, T.; Gobiet, A. Multi-variable error correction of regional climate models. *Clim. Chang.* **2013**, *120*, 871–887. [CrossRef]
85. Mendez, M.; Maathuis, B.; Hein-Griggs, D.; Alvarado-Gamboa, L.-F. Performance Evaluation of Bias Correction Methods for Climate Change Monthly Precipitation Projections over Costa Rica. *Water* **2020**, *12*, 482. [CrossRef]
86. Mehan, S.; Gitau, M.W.; Flanagan, D.C. Reliable Future Climatic Projections for Sustainable Hydro-Meteorological Assessments in the Western Lake Erie Basin. *Water* **2019**, *11*, 581. [CrossRef]
87. Teutschbein, C.; Seibert, J. Is bias correction of Regional Climate Model (RCM) simulations possible for non-stationary conditions? *Hydrol. Earth Syst. Sci.* **2013**, *17*, 5061–5077. [CrossRef]
88. Moss, R.H.; Edmonds, J.A.; Hibbard, K.A.; Manning, M.R.; Rose, S.K.; Van Vuuren, D.P.; Carter, T.R.; Emori, S.; Kainuma, M.; Kram, T.; et al. The next generation of scenarios for climate change research and assessment. *Nature* **2010**, *463*, 747–756. [CrossRef]
89. Almazroui, M.; Saeed, F.; Saeed, S.; Islam, M.N.; Ismail, M.; Klutse, N.A.B.; Siddiqui, M.H. Projected Change in Temperature and Precipitation Over Africa from CMIP6. *Earth Syst. Environ.* **2020**, *4*, 455–475. [CrossRef]
90. Hobbs, J.E.; Lindesay, J.A.; Bridgman, H.A. *Climate of the Southern Continents: Present, Past and Future*; Wiley: Hoboken, NJ, USA, 1998; p. 318.
91. Lindesay, J.A. South African rainfall, the Southern Oscillation and a Southern Hemisphere semi-annual cycle. *J. Clim.* **1988**, *8*, 17–30. [CrossRef]
92. Taylor, K.E. Summarizing multiple aspects of model performance in a single diagram. *J. Geophys. Res. Atmos.* **2001**, *106*, 7183–7192. [CrossRef]
93. Ashaley, J.; Anornu, G.K.; Awotwi, A.; Gyamfi, C.; Anim-Gyampo, M. Performance evaluation of Africa CORDEX regional climate models: Case of Kpong irrigation scheme, Ghana. *Spat. Inf. Res.* **2020**, *28*, 735–753. [CrossRef]
94. Pfeifer, S.; Bülow, K.; Gobiet, A.; Hänsler, A.; Mudelsee, M.; Otto, J.; Rechid, D.; Teichmann, C.; Jacob, D. Robustness of Ensemble Climate Projections Analyzed with Climate Signal Maps: Seasonal and Extreme Precipitation for Germany. *Atmosphere* **2015**, *6*, 677–698. [CrossRef]
95. McSweeney, C.; New, M.; Lizcano, G.; Lu, X. The UNDP Climate Change Country Profiles. *Bull. Am. Meteorol. Soc.* **2010**, *91*, 157–166. [CrossRef]
96. Salite, D.; Poskitt, S. Managing the impacts of drought: The role of cultural beliefs in small-scale farmers' responses to drought in Gaza Province, southern Mozambique. *Int. J. Disaster Risk Reduct.* **2019**, *41*, 101298. [CrossRef]
97. Midgley, S.; Dejene, A.; Mattick, A. *Mozambique Adaptation to Climate Change in Semi-Arid Environments: Experience and Lessons from Mozambique*; FAO: Rome, Italy, 2012; ISBN 978-92-5-107135-9.
98. INAM. *Atlas de Precipitação de Moçambique*; INAM: Maputo, Mozambique, 2012.